DEVELOPMENT OF DATA ASSIMILATION FOR ANALYSIS OF ION DRIFTS DURING GEOMAGNETIC STORMS

BY

JIAHUI HU

Submitted in partial fulfillment of the
requirements for the degree of
Doctor of Philosophy in Mechanical and Aerospace Engineering
in the Graduate College of the
Illinois Institute of Technology

Approved ______________________
Adviser

Chicago, Illinois
May 2024

ACKNOWLEDGMENT

I am extremely grateful to my supervisor, Dr. Seebany Datta-Barua, for her unwavering support and expertise. She not only guided me in my research endeavors but also generously provided professional advice for both my academic pursuits and personal growth. Thank you!

Additionally, I appreciate my Illinois Institute of Technology Ph.D. committee members: Dr. Alex Chartier, Dr. Boris Pervan, Dr. Hassan Nagib, and Dr. Qing-Chang Zhong, for dedicating their valuable time and offering insightful suggestions in the development of my thesis. Thanks to IIT, Armour College of Engineering, Mechanical Materials Aerospace Engineering Department.

I want to thank my past and present lab mates at the IIT Space Weather Lab, with special acknowledgment to Aurora López Rubio, Gytis Blinstrubas, Roohollah Parvizi, Ningchao Wang, Yang Su, and Daniel Miladinovich. I sincerely appreciate the Graduate Visitor Program (GVP) advisor at National Center for Atmospheric Research (NCAR): Dr. Nicholas Pedatella. Also a lot of thanks to collaborators Dr. Sarah McDonald and Dr. Shun-Rong Zhang, for their help and support.

I want to express my gratitude to my family members: mother Yaqin Li, aunt Xueqin Li, and uncle-in-law Charles Smith, especially in remembrance of my grandparents, Hongshui Li and Jingqiu Shi, for their endless supports. Last but not the least, to Chenhao Gao, for all his love and encouragement during my journey.

This work was funded by NASA 80NSSC19K0086, AFOSR FA9550-23-1-0169, and IIT Graduate Research Assistantship. GVP was supported by NCAR sponsored by the National Science Foundation (NSF) under Cooperative Agreement No. 1755088. Thanks to the NSF Coupling, Energetics and Dynamics of Atmospheric Regions Program for workshop travel support in 2022 and 2023.

The authors thank the Data Analysis Center for Geomagnetism and Space Magnetism of Kyoto University for maintaining the World Data Center for Geomagnetism in Kyoto. The Ap index and provisional Dst index data shown in this work can be downloaded at their website [1]. The proton density, solar wind speed and magnetic field are archived from Advanced Composition Explorer (ACE) and Deep Space Climate Observatory (DSCOVR) satellite missions [2, 3]. EMPIRE source code is proprietary but may be licensed for use by contacting S. Datta-Barua. The SAMI3 model can be run on request at the Community Coordinated Modeling Center website `https://ccmc.gsfc.nasa.gov/models/SAMI3~3.22`. The Sami3 is Also a Model of the Ionosphere (SAMI3) and SAMI3/IDA4D (Ionospheric Data Assimilation Four-Dimension) codes used in this work were run by A. Chartier and S. McDonald. The Millstone Hill Incoherence Scatter Radar measurements for validation purpose are provided from S. Zhang, and the derived data products are available on the Madrigal website `http://millstonehill.haystack.mit.edu`. The SuperDARN data products are provided by A. Chartier. SuperDARN is a collection of radars funded by national scientific funding agencies of Australia, Canada, China, France, Italy, Japan, Norway, South Africa, United Kingdom and the United States of America.

AUTHORSHIP STATEMENT

I, Jiahui Hu, attest that the work in this thesis is substantially my own. In accordance with the disciplinary norm of authorship in Mechanical and Aerospace Engineering, the following collaborations occurred in the thesis. (Please consult Appendix S of the IIT Faculty Handbook for further information.)

My adviser, Prof. Seebany Datta-Barua, contributed to the design of all experiments and assisted and guided in the interpretation of data as is the norm for a doctoral supervisor.

Alex Chartier and Sarah McDonald provided datasets and advice on use for developing the contributions. Aurora López Rubio initiated the idea and built the workflow for contribution of Chapter 3. Shun-Rong Zhang provided the datasets for Chapter 4. Nicholas Pedatella supported the development of Chapter 5.

The content in Chapter 3 was accepted by the journal of American Geophysical Union Space Weather division. The open-access publication title is “Quantification of Representation Error in the Neutral Winds and Ion Drifts Using Data Assimilation”, with assigned doi: `https://doi.org/10.1029/2023SW003609` [4]. For the journal, Aurora López Rubio contributed to conceptualization, investigation, methodology, and software. Seebany Datta-Barua contributed to the conceptualization, formal analysis, funding acquisition, project administration and supervision. Alex Chartier and Sarah McDonald provided resources for this study.

TABLE OF CONTENTS

LIST OF FIGURES

LIST OF SYMBOLS

Scalar

Symbol	Description
a_{prod}	Ion production rate
a_{loss}	Ion loss rate
a_{grav}	Ion transport due to gravitation
a_{dfsn}	Ion transport due to diffusion
a_u	Ion transport due to neutral wind
a_{exb}	Ion transport due to ExB effect
a_0	Climate modeled ion transport
δa_u	EMPIRE correction of ion transport due to neutral wind
δa_{exb}	EMPIRE correction of ion transport due to ExB effect
k	time epoch
l	Polynomial degree
L	L-shell number
L_{min}	Minimum L-shell number
L_{max}	Maximum L-shell number
m	Polynomial order
N	Electron density
r	Radius
R_e	Earth radius
$\delta v_{\perp r}$	Ion velocity correction in magnetic radial direction

$\delta v_{\perp\theta}$	Ion velocity correction in magnetic co-latitudinal direction
$\delta v_{\perp\phi}$	Ion velocity correction in magnetic longitudinal direction
$\delta v_{\perp z}$	Field-perpendicular zonal ion velocity correction
$\delta v_{\perp m}$	Field-perpendicular meridional ion velocity correction
θ	Latitude
ρ_+	Gyro frequency
τ	Time constant
ϕ	Longitude

Vector

$\hat{b}$	Magnetic field-align direction vector
$\vec{B}$	Magnetic field
$\mathbf{e}^-$	Prior-measurement state error
$\mathbf{e}^+$	Post-measurement state error
$\vec{E}$	Electric field
$\hat{g}_E$	Geographic east direction vector
$\hat{g}_N$	Geographic north direction vector
$\hat{g}_U$	Geographic up direction vector
$\hat{m}_E$	Geomagnetic east direction vector
$\hat{m}_N$	Geographic north direction vector
$\hat{m}_U$	Geographic up direction vector
$\vec{u}$	Neutral wind velocity
$\vec{v}$	Ion velocity

$\vec{v}_\perp$	Field-perpendicular ion velocity
$\vec{v}_\parallel$	Field-perpendicular ion velocity
$\vec{v}_u$	Neutral wind dynamo
$\vec{v}_{grav}$	Ion velocity due to gravity
$\vec{v}_{dfsn}$	Ion velocity due to diffusion
$\delta\mathbf{x}$	True state
$\delta\hat{\mathbf{x}}^-$	Prior-measurement estimated state
$\delta\hat{\mathbf{x}}^+$	Post-measurement estimated state
$\mathbf{x}_\mathbf{c}^\mathbf{lm}$	Cosine coefficient
$\mathbf{x}_\mathbf{s}^\mathbf{lm}$	Sine coefficient
$\mathbf{z}$	Measurement
$\mathbf{z}_{\partial\mathbf{N}/\partial\mathbf{t}}$	Measurement gap between observations and model values of electron density rate
ϵ	Observation noise
$\epsilon_\mathbf{rep}$	Representation error
$\epsilon_\mathbf{msmt}$	Measurement error
$\epsilon_\mathbf{vi}$	Analysis error between true and modeled velocities
$\bar{\epsilon}_\mathbf{vi}(\theta; t)$	Mean error of zonally averaged $\epsilon_\mathbf{vi}$
$\mu_{\epsilon_\mathbf{vi}}(\theta)$	Mean error of time averaged $\bar{\epsilon}_\mathbf{vi}(\theta; t)$
$\sigma_{\epsilon_\mathbf{vi}}(\theta)$	Standard deviation of time averaged $\bar{\epsilon}_\mathbf{vi}(\theta; t)$
η	Dynamic process error
$\hat{\perp}_z$	Magnetic field-perpendicular zonal unit vector

$\hat{\perp}_m$	Magnetic field-perpendicular meridional unit vector

Matrix

$\mathbf{H}$	State mapping matrix
$\mathbf{H_V}$	State mapping matrix of $E \times B$ transport correction
$\mathbf{H_u}$	State mapping matrix of neutral wind transport correction
$\mathbf{H_{\perp r}}$	State transition matrix onto radial ion velocity space
$\mathbf{H}_{\perp\theta}$	State transition matrix onto latitudinal ion velocity space
$\mathbf{H}_{\perp\phi}$	State transition matrix onto longitudinal ion velocity space
$\mathcal{H}(x)$	Real physical state
$\mathbf{H}\hat{x}$	Linear approximations of physical states
$\mathbf{K}$	Kalman/linear gain of measurement
$\mathbf{K}'$	Linear gain of prior-measurement state
$\mathbf{P}^-$	Prior-measurement state covariance
$\mathbf{P}^+$	Post-measurement state covariance
$\mathbf{P_0}$	Climate model state covariance
$\mathbf{Q}$	Dynamic process noise covariance
$\mathbf{R}$	Observation noise covariance
$\mathbf{R_{rep}}$	Representation error covariance
$\mathbf{R_{msmt}}$	Measurement error covariance
$\mathbf{R_{a0}}$	Background model error covariance
$\mathbf{R_N}$	Electron density error covariance
$\mathbf{\Phi}$	State transition matrix

Abbreviated term

ACE	Advanced Composition Explorer
A-CHAIM	Assimilative Canadian High Arctic Ionospheric Model
AMIE	Assimilative Mapping Ionospheric Electrodynamics
AMGeo	Assimilative Mapping of Geospace Observations
CME	Coronal Mass Ejection
DA	Data Assimilation
DART	Data Assimilation Research Testbed
Dst	Disturbance storm time
DWM	Disturbance Wind Model
DMSP	Defense Meteorological Satellite Program
DSCOVR	Deep Space Climate ObserVatoRy
EMPIRE	Estimating Model Parameters Ionospheric Reverse Engineering
EUV	Extreme UltraViolet
EIA	Equatorial ionization anomaly
FAA	Federal Aviation Administration
GNSS	Global Navigation Satellite System
GPS	Global Positioning System
GIRO	Global Ionospheric Radio Observatory
GSM	Geocentric Solar Magnetospheric
HWM	Horizontal Wind Model
IDA4D	Ionospheric Data Assimilation Four-Dimension

IT	Ionosphere-Thermosphere
IMF	Interplanetary Magnetic Field
IRI	International Reference Ionosphere
IRTAM	IRI Real-Time Assimilative Mapping
IGRF	International Geomagnetic Reference Field
LT	Local time
LETKF	Local Ensemble Transform Kalman Filter
MHISR	Millstone Hill Incoherent Scatter Radar
NILE	Nighttime Ionospheric Localized Enhancement
Nmf2	Max electron density at F2 layer
PRE	Pre-Reversal Enhancement
PT	Polarization terminator
SAMI3	Sami3 is Also a Model of the Ionosphere
SuperDARN	Super Dual Auroral Radar Network
SAC-C	Satélite de Aplicaciones Científicas-C
SED	Storm Enhanced Density
TEC	Total Electron Content
TIEGCM	Thermosphere-Ionosphere-Electrodynamics General Circulation Model
TWAM	Thermospheric Wind Assimilation Model
UT	Universal time
UV	UltraViolet
vTEC	vertical Total Electron Content

WACCM-X	Whole Atmosphere Community Climate Model with thermosphere and ionosphere eXtension
WDCG	World Data Center for Geomagnetism
WAAS	Wide Area Augmentation System

ABSTRACT

The primary objective of this dissertation is to gain insight into geomagnetic storm effects at mid-latitudes induced by solar activity. Geomagnetic storms affect our everyday lives because they give rise to transient signal loss, data transmission errors, negatively impacting users of satellite navigation systems. The Nighttime Localized Ionospheric Enhancement (NILE) is a localized plasma enhancement that because it is not well understood, drives the design of satellite-based augmentation systems.

To better secure operation of technological infrastructure, it is essential to build a comprehensive understanding of the atmospheric drivers, especially during solar active periods. Instrument measurements and climate models serve as valuable tools in obtaining information regarding the occurrence of space weather events; nonetheless, both sources exhibit quantitative and qualitative limitations. Data assimilation, an evolving technique, integrates measurements and model information to optimize the state estimations.

This dissertation presents developments in a data assimilation algorithm known as Estimating Model Parameters from Ionospheric Reverse Engineering (EMPIRE), and its applications in investigating the atmospheric behaviors under varying solar conditions. EMPIRE is a data assimilation algorithm specifically designed for upper atmospheric driver estimation of neutral wind and ion drifts at user-defined spatial and temporal scales. The EMPIRE application in this work aims to contribute to a more comprehensive understanding of the effects of the NILE.

EMPIRE utilizes the Kalman filter to optimize state calculations primarily based on electron density rates, provided by other data assimilation algorithms. Earlier runs of the algorithm used pre-defined values for the background state covariance cross time. To address model limitations under changing geomagnetic conditions, the algorithm is enhanced by concurrently updating the background state covariance during assimilation processes. Additionally, representation error is incorporated as a component of the observation error, and error analysis is performed through a synthetic-data study. Previously, EMPIRE fused Fabry-Perot Interferometer (FPI) neutral wind measurements, demonstrating increased agreement with validation neutral wind data. In this work, this approach is extended to augment Coherent Scatter Radar (CSR) ion drift measurements from Super Dual Auroral Radar Network (SuperDARN), providing additional insights into EMPIRE's estimated field-perpendicular ion motion. For an in-depth exploration of storm-related NILE, both EMPIRE and another data assimilation method, the Whole Atmosphere Community Climate Model with thermosphere and ionosphere eXtension coupled with Data Assimilation Research Testbed (WACCM-X + DART), is implemented for a storm event to test the proposed NILE driving mechanism. Furthermore, this dissertation introduces a Kalman smoother technique into the EMPIRE to enhance its ability to assess past storm events, and to explore the potential for algorithm improvements.

CHAPTER 1

INTRODUCTION

Space weather is a research field that focuses on the activity of the Sun and its influence on our planet. Earth's internal magnetic field, extending from its interior into space, interacts with the solar wind and streams of energetic particles. The ionosphere-thermosphere (IT) coupled region, spanning from 100 $[km]$ to 1000 $[km]$ in altitude, consists mainly of ionizied and neutral particles, respectively, that are heatded and ionized by the sun's radiation. Also, energetic particles from the Sun and the Earth's magnetosphere can enter atmosphere particularly through the high latitude region [5].

During periods of severe solar activity (i.e. solar storms), trans-ionospheric radio systems experience longer delays than usual due to refraction by ionospheric plasma. Understanding the protective shield of the IT region is essential to minimize risks to technological system used in daily life, such as on the Global Navigation Satellite System (GNSS), whose signal propagation is influenced by deflection, attenuation, or production within the IT region [6].

Researchers have contributed tremendous efforts to understand storm-related phenomenon. The Nighttime Ionospheric Localized Enhancement (NILE) is one of the intriguing ionospheric phenomena observed most notably during extreme storms, involving enhanced electron density concentrated over a few hundred kilometers of the mid-latitude region in the US during local nighttime. The driving mechanism behind the NILE is currently unknown and under investigation.

When describing a phenomenon, mathematical models serve as valuable tools for providing scientific explanations of spatial and temporal behaviors, while instrumental observations offer realistic insights into the states of the system. Nevertheless, both approaches face limitations characterized by an insufficient grasp of the true states. Physics-based equations or empirical derivations in models inadequately capture the complete description of true states due to the imperfect capture of dynamic processes, parameter uncertainties and computing limitations [7]. Specifically, physics-based equations may subjected to assumptions and linearization of the complex dynamic process, and empirical model errors can be caused by extrapolation, over-fitting or under-fitting issues. Limitations in measurements predominantly arise from issues of quantity (i.e., data sparsity) and quality (i.e., errors) [8]. Addressing these limitations, data assimilation algorithms analyze information gaps between models and measurements, aiming to optimize state calculations that approximate the true states. Data assimilation is pivotal for enhancing comprehension of behaviors across diverse earth science disciplines, encompassing meteorology, oceanography, and hydrology [9].

This chapter predominantly focuses on the basic knowledge foundation needed to understand the research scope and contributions. Section 1.1 introduces the IT coupled region as the focal point of research. The research history of periodic solar activities, the drivers of geomagnetic storms, and the categorization of storm severity are outlined in Section 1.2. Section 1.3 describes the primary NILE phenomenon initially observed during the October 2003 storm. Section 1.4 traces the traditional branches of Data Assimilation (DA) algorithms, providing a comparative analysis between existing DA algorithms and the unique DA algorithm, Estimating Model Parameters from Ionospheric Reverse Engineering (EMPIRE), which uses a Kalman filter to estimate the information gap between model and measurements. Lastly, Section 1.5 provides the specific contributions of this dissertation to the EMPIRE algorithm and its application in investigating the NILE phenomenon.

1.1 Ionosphere-Thermosphere Coupled Region

The Earth's atmosphere consists of the neutral atmosphere and charged particle ionosphere embedded within it. The neutral atmosphere consists of neutral gas particles, while the ionosphere is the region where ionized gas forms [10]. The thermosphere and ionosphere coexist within a shared altitude range, approximately spanning from 100 $[km]$ to 1000 $[km]$. The F layer at about 200-500 $[km]$ contains most plasma.

To simplify the dynamic modeling processes that characterize the relationship between electron density, ions, and neutrals, O^+ is assumed in this work to be the predominant ion species in the IT coupled region and our investigation focuses on the F region.

1.2 Geomagnetic Storm

Throughout the centuries, researchers have invested significant efforts in examining the interactions between the Sun and Earth, particularly the repercussions of periodic solar activity. Alexander Von Humboldt observed magnetic deflection and noted the occurrence of northern lights at high latitudes during the storm event on December 20, 1806. Measurements of the geomagnetic field by J. Von Lamont and Edward Sabine revealed sun-earth interactions linked to a periodic variability of the Sun with a cycle of approximately 10.33 years. Concurrently, Heinrich Schwabe published observations of sunspots, indicating a similar cycle of about 10 years. Swiss astronomers Rudolf Wolf and Hermann Firtz further investigated the correlations between the frequencies of auroras and sunspots. They determined the average sunspot period to be 11.111 ±0.038 years based on a proposed sunspot number equation derived from empirical data dating back to the eighteenth century [11].

The initial exploration into periodic solar activity prompted a fundamental inquiry into the driving mechanisms behind geomagnetic storms. The first well-documented observation of a solar flare in September 1859, famously known as the "Carrington flare," was published by Richard Carrington [12]. Subsequent statistical analyses confirmed that geomagnetic storms, triggered by large solar flares, emit intense X-rays, extreme ultraviolet (EUV), and UV radiation, leading to the ionization of neutral particles in Earth's atmosphere.

In the 1970s, Coronal Mass Ejection (CME) events were identified through coronagraph observations on the OSO-7 and Skylab spacecraft. These events serve as sources of energy release and cause interplanetary disturbances affecting Earth [13]. The contemporary definition of CME events involves the outward flow of energetic particles from the Sun, with these particles carrying a sustained southward Interplanetary Magnetic Field (IMF). This southward IMF is responsible for driving geomagnetic storms on Earth [14].

To assess the energy dissipation within the magnetosphere resulting from induced geomagnetic storms, various commonly used indices such as Kp, Ap, AE, and Dst are employed. The differences in these indices are comprehensively elucidated in [15]. In our research, we use the Disturbance Storm Time (Dst) index as a key indicator of storm severity. The Dst index monitors the magnetic ring current and measures magnetic activity at hourly intervals, obtainable from the World Data Center for Geomagnetism (WDCG), Kyoto [16, 17]. When the charged particles (i.e. electrons and protons) interact with the Earth, they generate electric currents in the space environment that oppose to the Earth's internal magnetic field. As a result, the net magnetic field measured weakens due to the disturbances during geomagnetic active periods, and can be reflected by the Dst index, which measures the deviation of the Earth's magnetic field from nominal state. A drop in the Dst index indicates the decreased Earth's magnetic field because of the increased solar activities. According to the classification outlined in [18], storm intensity levels can be distinguished based on the Dst minimum values criterion, as summarized in Table 1.1.

Based on Dst values, the storm phases can be categorized as initial, main and recovery, as indicated by the Dst value plot for storm event March 2015 in Figure 1.1. Note that the storm sudden commencement (SSC) indicates enhanced IMF in northward direction same as Earth's internal magnetic field [19], and SSC does not necessarily appear for every storm event.

Table 1.1. Storm Classification [18]

Storm class	Dst_{min} range [nT]	Dst_{min} mean [nT]
weak	-30 to -50	-36
moderate	-50 to -100	-68
strong	-100 to -200	-131
severe	-200 to -350	-254
extreme	$<$ -350	-427

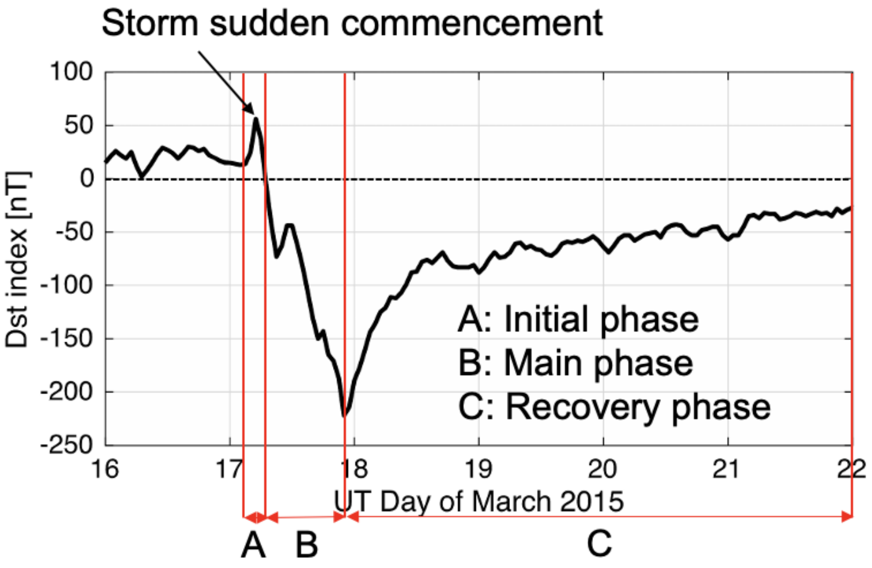

Figure 1.1. Storm phases (A: Inital, B: Main, C: Recovery) indicated by Dst example plot for the storm event on March 2015.

1.3 Nighttime Ionospheric Localized Enhancement (NILE)

The NILE, a storm-related phenomenon, manifests as a persistent enhancement in Total Electron Content (TEC) that co-rotates over the United States Florida region during local nighttime in the storm recovery phase. Because refractive delay is proportional to plasma along the signal path, the geomagnetic storm of October 29-30, 2003, a noticeable 10-meter higher ranging error at Global Positioning System (GPS) L1 frequency compared to the nighttime background ionosphere TEC was observed in the mid-latitude region. Simultaneously, the tracks of Jason Dual-frequency and Satellite de Aplicaciones Cientificas-C (SAC-C) provided measurements of vertical ionospheric delay over Florida, indicating the presence of enhanced TEC in that region [20]. Figure 1.2 depicts the regional vertical ionospheric delay map measured in meters of L1 during the storm recovery phase at 05 Universal Time (UT), or 00 Local Time (LT) in Florida. The NILE also manifested during storm events in November 2003 and August 2018. This involved a moderate enhancement of the F2 layer peak electron density (Nmf2) extended longitudinally at mid-latitudes of 30° - 40° N [21].

1.4 Data Assimilation

To gain a comprehensive understanding of the Earth and its surrounding environment, a collaborative approach involving climate models and direct measurements is employed to investigate physical characteristics relevant to various research disciplines. In this section, I introduce model and data sources that will be used in this work, as examples. Climate models are constructed to analyze states based on scientific principles and empirical data. An example is the Thermosphere-Ionosphere-Electrodynamics General Circulation Model (TIEGCM), which assumes hydrostatic equilibrium, constant gravity, steady-state ion and electron energy equations, and incompressibility on a constant pressure surface [22]. The model offers a global perspective on IT region temperatures, plasma density, and electric potential in a 4D grid

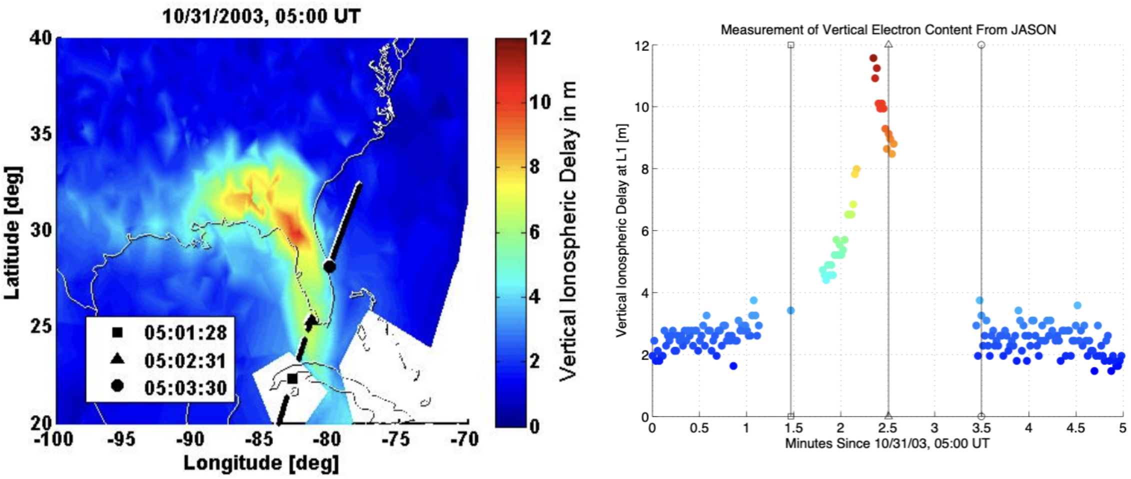

Figure 1.2. The left figure is a regional map of Vertical Ionospheric Delay at 05 UT. The color bar ranges from 0 (blue) to 12 meters (red) of ranging delay at L1 frequency. The shadowed black line is the Jason satellite track. The square, triangle and circle marks are the positions of Jason at 1-min intervals. The right figure shows the Jason vertical delay measurements below its orbit altitude as a function of time, with respect to the satellite positions. Image credit: [20]

map (Pressure Level x longitude x latitude x time). The Whole Atmosphere Community Climate Model (WACCM) has been extended to include the thermospheric and ionospheric dynamics, resulting in the development of WACCM-X (eXtension).

Measurements of IT parameters encompass remote sensing and in-situ techniques. Remote sensing techniques involve measuring properties of emitted and reflected radiation at a distance from the target. For instance, the Millstone Hill Incoherent Scatter Radar (MHISR) transmits high-power radio waves in the high-to-ultrahigh-frequency range, providing altitudinal plasma states of temperature, density, composition, and velocity [23]. Super Dual Auroral Radar Network (SuperDARN) is another radar network consisting of 35 high frequency radars, and provides high-latitude convection maps in the northern and southern hemisphere [24].

DA techniques, commonly employed for optimization through the assimilation of information from both models and measurements, consist of traditional branches within Bayesian-based algorithms. These branches encompass Variational, Ensemble, and Monte-Carlo methods [25]. In the case of the variational DA algorithm linearized observation and forecast operators are applied, along with pre-defined Gaussian uncertainty statistics for both models and observations. This process results in the optimized state obtained by minimizing the cost function, analogous to the Kalman filter, at each analysis time epoch. Ionospheric Data Assimilation 4-D (IDA4D) is a example of 3D variation algorithm that yields a spatial map of electron densities at each time analysis epoch [26, 27, 28, 29]. The ensemble DA algorithm is adaptable to nonlinear systems, utilizing uncertainty statistics derived from an ensemble of data sources. The Monte-Carlo method becomes particularly useful when dealing with non-Gaussian error distributions. The Data Assimilation Research Testbed (DART) is built based on the ensemble method that estimates statistical means and co-variances from a group of assimilated states [30].

EMPIRE, employs a linearized electron continuity equation to explicitly compute ionospheric drivers such as neutral wind and electric potential from time-varying densities. This algorithm predominantly uses modeled information on ion density rates and ion transport terms, applying the Kalman filter technique to generate driver estimations at each time epoch. Recent studies on EMPIRE focused on developments of mapping matrices and scientific investigations of the NILE as affected by neutral winds, and also enabled to ingest neutral wind measurements [31, 6].

Table 1.2 summarizes the data assimilation algorithms related to the dissertation, indicating the technique and horizontal resolution for each algorithm.

1.5 Contributions

This work asks the following research questions: **1) What methodologies can be employed to enhance the understanding of ionospheric behavior**

Table 1.2. Data assimilation algorithms

Name	Classification	Horizontal resolution [dlat x dlon]
EMPIRE	Sequential	6° x 6°
IDA4D	Variational	1° x 4°
DART	Sequential	1.9° x 2.5°

during geomagnetic storm periods through data assimilation? 2) What inferences can be drawn from the research methodologies employed? 3) How may the findings be applied to investigate the NILE phenomenon? This dissertation is structured around these research questions, outlining four primary contributions. The analysis period and data sources used for EMPIRE runs in this dissertation are summarized in Table 1.3. Each contribution is introduced in the following subsections.

Table 1.3. Contributions on EMPIRE development and application

Contribution	Analysis period	DA	Measurement source	Validation
#1 (1.5.1)	25 - 26 Aug 2018	EMPIRE	SAMI3	SAMI3
#2 (1.5.2)	16 - 18 Mar 2015	EMPIRE	SAMI3/IDA4D, SuperDARN	SuperDARN, MHISR
#3 (1.5.3)	16 - 18 Mar 2015	EMPIRE, DART	SAMI3/IDA4D	
#4 (1.5.4)	25 - 26 Aug 2018	EMPIRE	SAMI3	SAMI3

1.5.1 Reconstruction of representation error covariance in Kalman filter.

In this work we quantify the representation error of EMPIRE using a simulated truth experiment, and evaluate EMPIRE performance by comparing to that simulated truth. Sami is Also a Model of the Ionosphere (SAMI3) [32] serves as the background climate model and pseudo-measurements for the EMPIRE observation system. This configuration allows the data assimilation inputs to be self-consistent between each other and with the validation data. For both the quiet period on 25 August 2018 and subsequent storm on 26 August 2018, the EMPIRE estimation of ion drifts is better at low-to-mid geomagnetic latitudes, with mean error up to 10 $[m/s]$ during quiet time and 40 $[m/s]$ during storm time. For the high latitude (±60° to 87°), the mean errors exceed 50 m/s and variances up to 200 $[m/s]$, and the relative errors are higher than the "truth." At latitudes of ± 87°, the large errors are attributed to a boundary effect. The field-parallel neutral wind estimation mean errors at high latitudes are up to 5 $[m/s]$ during quiet time and 10 $[m/s]$ during storms. However, the neutral wind mean errors peak near ± 20° latitudes, with larger uncertainties, then converge to 0 approaching higher latitudes. By conducting this study, we define a method for obtaining the representation error covariance for future use of EMPIRE with SAMI3 as background.

1.5.2 Augmentation of SuperDARN ion drift measurements to EMPIRE.

During geomagnetic storms, the capabilities of current climate models predicting ionospheric behavior are notably limited, primarily due to the disruptive influence of strong solar disturbances. In this study, a new augmentation method is evaluated in which ion drift measurements are assimilated into EMPIRE for March 2015 storm event. GNSS-based TEC measurements are assimilated using IDA4D, in conjunction with the SAMI3 first-principles background model. In the primary setup, plasma densities from IDA4D/SAMI3 are temporally differentiated and assimilated into EMPIRE. The ion drift measurements augmented to the new method are obtained from Super Dual Auroral Radar Netowrk (SuperDARN) sites in the mid-to-high latitude region of the northern hemisphere. To validate the implementation outcomes from comparing the cases of with or without ingesting ion drifts, independent data sources are used as the validation datasets.

1.5.3 NILE phenonmenon investigation via EMPIRE and WACCM-X + DART algorithms. NILE is a plasma enhancement sometimes observed in the local nighttime during significant geomagnetic storms, often over Florida. To investigate the physical mechanisms that might contribute to this phenomenon, we use EMPIRE, assimilating plasma density rates, to estimate the mid-latitude electric potential and the ion drifts associated with it. For this study, the 17 March 2015 storm is investigated because it has ion velocity measurements from various locations available for ingestion and for validation. Furthermore, we investigate the geographic east-north-up components of the ion velocity from the EMPIRE outputs in the F region above Miami, Florida, to examine whether the proposed theories of the pre-reversal enhancement and polarization terminator might be contributing factors to the NILE.

1.5.4 Kalman smoother implementation in EMPIRE. In this study, we are updating the Kalman filtering technique to a filtering/smoothing coupled technique to test whether it can improve the analysis of ionospheric driver estimations. The filtering/smoothing technique analyzes the ionospheric drivers recursively in a time forward and backward sequence. Since all measurement and model information is available to access for a past storm event, EMPIRE can update the state vectors (i.e. ion drifts and neutral winds in EMPIRE), using the past and "future" data to yield the optimized estimations with the loop closure process. To be consistent with the preliminary study of the EMPIRE performance, we select the analysis time to be 25-26 August 2018, and validate the coupled technique with the primary case of only using the Kalman filter. If it is proved that the coupled technique can improve the ion drift calculations, future studies of the NILE could investigate the ion motion in the Florida region using the filter/smoother.

CHAPTER 2

TECHNICAL BACKGROUND

2.1 Kalman filter

The EMPIRE algorithm utilizes the Kalman filter to iteratively estimate the optimal state vector in a linear dynamic system, incorporating noisy measurement inputs. Eq. (2.1) represents the measurement update in the Kalman filter at each time step k. In this text, $\delta\mathbf{x_k}$ represents the true state vector, $\mathbf{H_k}$ is the mapping matrix that maps the state vector to the same physical variable as the measurement vector $\mathbf{z_k}$, and $\epsilon_\mathbf{k}$ denotes the measurement noise from the instruments. This noise is assumed to follow a normal distribution with a mean value of $\mathbf{0}$ and a variance of $\mathbf{R_k}$.

$$\mathbf{z_k} = \mathbf{H_k}\delta\mathbf{x_k} + \epsilon_\mathbf{k}, \epsilon_\mathbf{k} \sim \mathcal{N}(\mathbf{0}, \mathbf{R_k}) \tag{2.1}$$

Referring to the derivation of the Kalman filter in [33], we begin by defining two state vectors at each time step k: the estimated state vector after the measurement update, denoted as $\delta\hat{\mathbf{x}}_\mathbf{k}^+$, and the estimated state vector prior to the measurement information, denoted as $\delta\hat{\mathbf{x}}_\mathbf{k}^-$. Assuming that $\delta\hat{\mathbf{x}}_\mathbf{k}^+$ can be expressed as a linear combination of $\delta\hat{\mathbf{x}}_\mathbf{k}^-$ and the measurement vector $\mathbf{z_k}$, the linear gains for the prior-measurement state estimation vector and the measurement vector are represented by $\mathbf{K}'_\mathbf{k}$ and $\mathbf{K_k}$, respectively, in Eq. (2.2)

$$\delta\hat{\mathbf{x}}_\mathbf{k}^+ = \mathbf{K}'_\mathbf{k}\delta\hat{\mathbf{x}}_\mathbf{k}^- + \mathbf{K_k}\mathbf{z_k} \tag{2.2}$$

The post-measurement state error vector, denoted as $\mathbf{e}_\mathbf{k}^+$ in Eq. (2.3), is defined as the difference between the estimated state vector $\delta\hat{\mathbf{x}}_{\mathbf{k}}^{+}$ and the actual state vector $\delta\mathbf{x}_{\mathbf{k}}$.

$$\mathbf{e}_{\mathbf{k}}^{+} = \delta\hat{\mathbf{x}}_{\mathbf{k}}^{+} - \delta\mathbf{x}_{\mathbf{k}} \tag{2.3}$$

The prior-measurement state error vector $\mathbf{e}_{\mathbf{k}}^{-}$ in Eq. (2.4) defines the gap between the actual state vector $\delta\mathbf{x}_{\mathbf{k}}$ and the estimated prior-measurement state vector $\delta\hat{\mathbf{x}}_{\mathbf{k}}^{-}$.

$$\mathbf{e}_{\mathbf{k}}^{-} = \delta\hat{\mathbf{x}}_{\mathbf{k}}^{-} - \delta\mathbf{x}_{\mathbf{k}} \tag{2.4}$$

By substituting Eq. (2.2) and (2.4) into Eq. (2.3) and rearranging the equation, the relationship between the post-measurement state error vector $\mathbf{e}_{\mathbf{k}}^{+}$ and the prior-measurement state error vector $\mathbf{e}_{\mathbf{k}}^{-}$ is represented as Eq. (2.5).

$$\mathbf{e}_{\mathbf{k}}^{+} = (\mathbf{K}_{\mathbf{k}}\mathbf{H}_{\mathbf{k}} + \mathbf{K}'_{\mathbf{k}} - \mathbf{I})\delta\mathbf{x}_{\mathbf{k}} + \mathbf{K}'_{\mathbf{k}}\mathbf{e}_{\mathbf{k}}^{-} + \mathbf{K}_{\mathbf{k}}\epsilon_{\mathbf{k}} \tag{2.5}$$

By computing the expectation value of the post-measurement error vector as given in Eq. (2.5), the desired optimal condition is the expectation value of the post-measurement error vector being $\mathbf{0}$. Similarly, the expectation value of the prior-measurement error vector is also $\mathbf{0}$. This is attributed to the fact that the measurement error vector follows a normal distribution with a mean value of zero, making the expectation value of the measurement error vector $\mathbf{0}$ as well.

$$\mathbb{E}[\mathbf{e}_{\mathbf{k}}^{+}] = \underbrace{(\mathbf{K}_{\mathbf{k}}\mathbf{H}_{\mathbf{k}} + \mathbf{K}'_{\mathbf{k}} - \mathbf{I})}_{\mathbf{0}}\mathbb{E}[\delta\mathbf{x}_{\mathbf{k}}] + \mathbf{K}'_{\mathbf{k}}\underbrace{\mathbb{E}[\mathbf{e}_{\mathbf{k}|\mathbf{k-1}}]}_{\mathbf{0}} + \mathbf{K}_{\mathbf{k}}\underbrace{\mathbb{E}[\epsilon_{\mathbf{k}}]}_{\mathbf{0}} = \mathbf{0} \tag{2.6}$$

For the condition of Eq. (2.6) to be satisfied, the formulation of $\mathbf{K}'_{\mathbf{k}}$ in terms of $\mathbf{K_k}$ can be expressed as follows:

$$\mathbf{K'_k} = \mathbf{I} - \mathbf{K_k H_k} \tag{2.7}$$

Plugging Eq. (2.2) into Eq. (2.3) and replacing $\mathbf{K'_k}$ with $\mathbf{I} - \mathbf{K_k H_k}$, the expression for $\mathbf{e_k^+}$ can be redefined as:

$$\begin{aligned}\mathbf{e_k^+} &= (\mathbf{I} - \mathbf{K_k H_k})\delta\hat{\mathbf{x}}_\mathbf{k}^- + \mathbf{K_k}(\mathbf{H}\delta\mathbf{x_k} + \epsilon_\mathbf{k}) - \delta\mathbf{x_k} \\ &= (\mathbf{I} - \mathbf{K_k H_k})\underbrace{(\delta\hat{\mathbf{x}}_\mathbf{k}^- - \delta\mathbf{x_k})}_{\mathbf{e_k^-}} + \mathbf{K_k}\epsilon_\mathbf{k}\end{aligned} \tag{2.8}$$

The definition of the post-measurement state error covariance matrix $\mathbf{P_k^+}$ according to Eq. (2.8) is as follows:

$$\begin{aligned}\mathbf{P_k^+} &= \mathbb{E}[\mathbf{e_k^+}\mathbf{e_k^{+T}}] = (\mathbf{I} - \mathbf{K_k H_k})\mathbf{P_k^-}(\mathbf{I} - \mathbf{K_k H_k})^\mathbf{T} + \mathbf{K_k R_k K_k^T} \\ \mathbf{P_k^-} &= \mathbb{E}[\mathbf{e_k^-}\mathbf{e_k^{-T}}]\end{aligned} \tag{2.9}$$

The objective is to minimize the trace of the post-measurement error covariance in order to obtain the optimized estimated state vector. This involves taking the gradient of the trace of $\mathbf{P_k^+}$ with respect to $\mathbf{K_k}$ [33]:

$$\frac{d(Trace\mathbf{P_k^+})}{d(\mathbf{K_k})} = -2(\mathbf{H_k P_k^-})^\mathbf{T} + 2\mathbf{K_k}(\mathbf{H_k P_k^- H_k^T} + \mathbf{R_k}) \tag{2.10}$$

Equating (2.10) to $\mathbf{0}$, the expression for the optimized gain, known as the Kalman gain, can be derived as presented in Eq. (2.11).

$$\mathbf{K_k} = \mathbf{P_k^- H_k^T}(\mathbf{H_k P_k^- H_k^T} + \mathbf{R_k})^{-1} \tag{2.11}$$

By rearranging Eq. (2.2) and Eq. (2.9) and incorporating the derived Kalman gain $\mathbf{K_k}$ from Eq. (2.11) and the measurement gain $\mathbf{K'_k}$ from Eq. (2.7), the posterior state estimate $\delta\mathbf{\hat{x}_k^+}$ and posterior covariance matrix $\mathbf{P_k^+}$ can be revised to incorporate the measurement information, as indicated in (2.12) and (2.13).

$$\delta\mathbf{\hat{x}_k^+} = \delta\mathbf{\hat{x}_k^-} + \mathbf{K_k}(\mathbf{z_k} - \mathbf{H_k}\delta\mathbf{\hat{x}_k^-})\mathbf{P_k^+} \tag{2.12}$$

$$\mathbf{P_k^+} = (\mathbf{I} - \mathbf{K_k}\mathbf{H_k})\mathbf{P_k^-} \tag{2.13}$$

In the subsequent time step k+1 of the process, the update for the true state vector $\delta\mathbf{x_{k+1}}$ follows a Gauss-Markov procedure as outlined in Eq. (2.14). Here, $\mathbf{\Phi_k}$ represents the state transition matrix, and $\eta_\mathbf{k}$ is the process noise vector, which follows a normal distribution with an error covariance of $\mathbf{Q_k}$.

$$\delta\mathbf{x_{k+1}} = \mathbf{\Phi_k}\delta\mathbf{x_k} + \eta_\mathbf{k}, \eta_\mathbf{k} \sim \mathcal{N}(\mathbf{0},\, \mathbf{Q_k}) \tag{2.14}$$

The predicted prior-measurement state vector $\delta\mathbf{\hat{x}_{k+1}^-}$ (Eq. (2.15)) and covariance matrix $\mathbf{P_{k+1}^-}$ (Eq. (2.16)) at $k+1$th time epoch are defined:

$$\delta\mathbf{\hat{x}_{k+1}^-} = \mathbf{\Phi_k}\mathbf{\hat{x}_k^+}, \tag{2.15}$$

$$\mathbf{P_{k+1}^-} = \mathbf{\Phi_k}\mathbf{P_k^+}\mathbf{\Phi_k^T} + \mathbf{Q_k} \tag{2.16}$$

Figure 2.1 is the Kalman Filter that is implemented in the EMPIRE algorithm and recursively calculates the optimized estimations. The initial state $\delta\mathbf{\hat{x}_1^-}$ and covariance matrix $\mathbf{P_1^-}$ are computed from the background modeled values as inputs to obtain the Kalman gain at first time epoch $\mathbf{K_k}$ and k=1. Then the posterior state $\delta\mathbf{\hat{x}_k^+}$ and covariance $\mathbf{P_k^+}$ are calculated and stored at that epoch. At next time step, the prior state $\delta\mathbf{\hat{x}_{k+1}^-}$ and covariance $\mathbf{P_{k+1}^-}$ are updated by the state transition matrix $\mathbf{\Phi_k}$

and feed in to the Kalman gain calculation, and finish the loop for the designated evaluation time period.

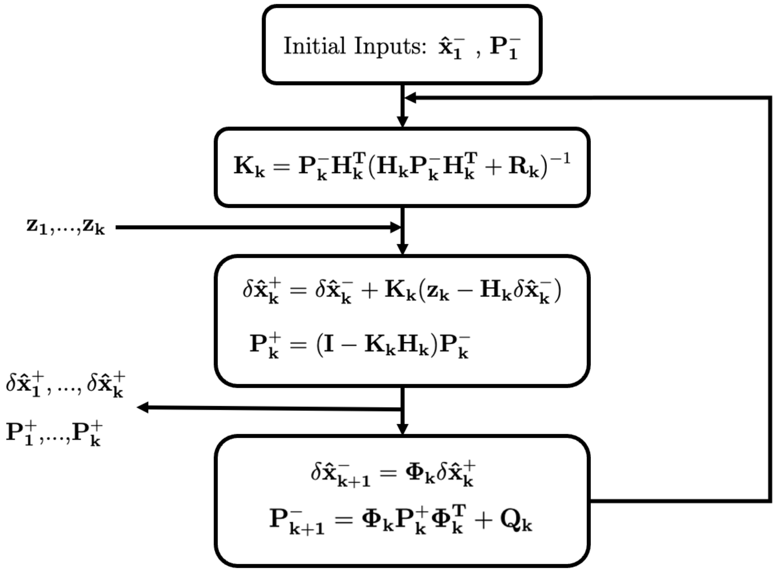

Figure 2.1. A flowchart of Kalman filtering loop. The initial inputs, $\mathbf{\hat{x}_1^-}$ and $\mathbf{P_1^-}$, represent the state vector and state covariance at the beginning of the process. The observation matrix is denoted as $\mathbf{H_k}$. The matrices $\mathbf{P_k^+}$ and $\mathbf{P_k^-}$ represent the post-measurement and prior-measurement state error covariances at the k-th time epoch, respectively. Correspondingly, $\delta\mathbf{\hat{x}_k^+}$ and $\delta\mathbf{\hat{x}_k^-}$ represent the post-measurement and prior-measurement estimated state vectors. The measurement vector is denoted as $\mathbf{z_k}$, with $\mathbf{R_k}$ as the measurement error covariance matrix and $\mathbf{Q_k}$ as the process error covariance matrix at time step k. Additionally, $\mathbf{\Phi_K}$ represents the state transition matrix. At the time step of $k+1$, $\mathbf{\hat{x}_{k+1}^-}$ is the prior-measurement state estimate, and $\mathbf{P_{k+1}^-}$ is the prior-measurement state covariance.

2.2 Ion continuity equation

To simplify the dynamic modeling processes that characterize the relationship between electron density, ions, and neutrals, O^+ is assumed in this work to be the predominant ion species in the IT coupled region and our investigation focuses on the F region. Assuming an equal number of electrons and ions, with dominant ions being O^+, a valid assumption for the F-region ionosphere, the ion continuity equation is represented by Eq. (2.17). This equation describes, $\frac{\partial N}{\partial t}$, the time rate of change of electron density N in a finite volume.

$$\frac{\partial N}{\partial t} = \underbrace{a_{prod} + a_{loss}}_{Source\ terms} + \underbrace{\nabla \cdot (N\vec{v})}_{Convective\ terms} \tag{2.17}$$

The source terms include the production rate a_{prod} and loss rate a_{loss} of the ion species. The convective term involves the divergence ∇ of the electron density N dotted with the ion velocity $\vec{v}$. Ion velocity can be categorized into two components: (1) Ion transport in the presence of electric and magnetic fields. (2) Ion drag due to collisions between ionized and neutral species. In the first category, when a charged particle is subjected to magnetic and electric fields that are perpendicular to each other, the ion transport involves circular gyrations, and the direction of drift is determined by the cross product of the two fields. This type of drift is referred to as "E × B" drift, and $\vec{v}$ is the motion of the guiding center, averaging out gyrational motion.

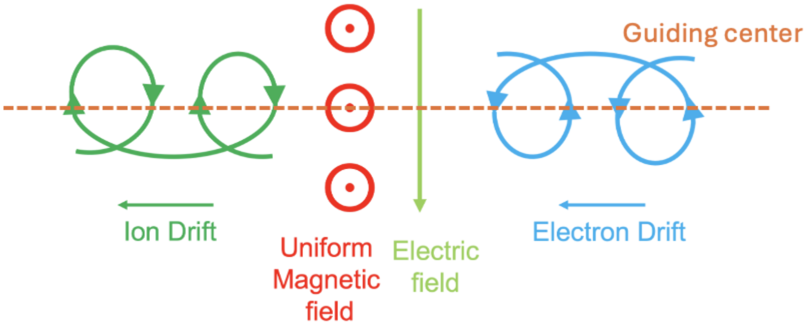

Figure 2.2. Ion and electron drifts due to uniform perpendicular electric and magnetic fields [34].

The formulation of the E × B drift $\vec{v}_\perp$ is given by:

$$\begin{aligned}\vec{v}_\perp &= \frac{\vec{E} \times \vec{B}}{||\vec{B}||^2} \\ &= \frac{-\nabla(V) \times \vec{B}}{B^2}\end{aligned} \tag{2.18}$$

Based on Eq. (2.19), ion drag due to the neutral wind dynamo $\vec{v}_N$ can be mathematically modeled in relation to the ratio of ion-neutral collisions to gyro frequency ρ_+. This modeling assumes the absence of an electric field, and the sole driving force is the magnetic field [35]. Here, $\hat{b}$ represents the magnetic field normal vector, and $\vec{u}$ is the neutral wind.

$$\vec{v_N} = \frac{1}{1+\rho_+^2}\left(\rho_+^2\vec{u} + \rho_+\vec{u}\times\hat{b} + (\vec{u}\cdot\hat{b})\hat{b}\right) \tag{2.19}$$

In the F-region, where $\rho_+ << 1$, the ion drag can be further simplified. It is important to note that its direction is along the magnetic fieldline.

$$\vec{v_N} = (\vec{u}\cdot\hat{b})\hat{b}$$

Other transport drivers that align with the magnetic field include gravitational $\vec{v}_{grav}$ and diffusive $\vec{v}_{dfsn}$ effects [36]. We assume that $\vec{E}$ parallel to $\vec{B}$ cannot be sustained because charges would rapidly move unimpeded to make the field line an equipotential. Therefore, the ion motion in the magnetic field-parallel direction $\vec{v}_{\|}$ is obtained by summing:

$$\vec{v_{\|}} = \vec{u} + \vec{v_{dfsn}} + \vec{v_{grav}} \tag{2.20}$$

Upon decomposing the convective terms into the field-perpendicular and field-parallel directions, Eq. (2.17) is expanded to:

$$\frac{\partial N}{\partial t} = a_{prod} + a_{loss}\underbrace{-\nabla\cdot(N\vec{v}_{\perp})}_{a_{exb}}\underbrace{-\nabla\cdot(N\vec{v}_{\|})}_{a_{\|}} \tag{2.21}$$

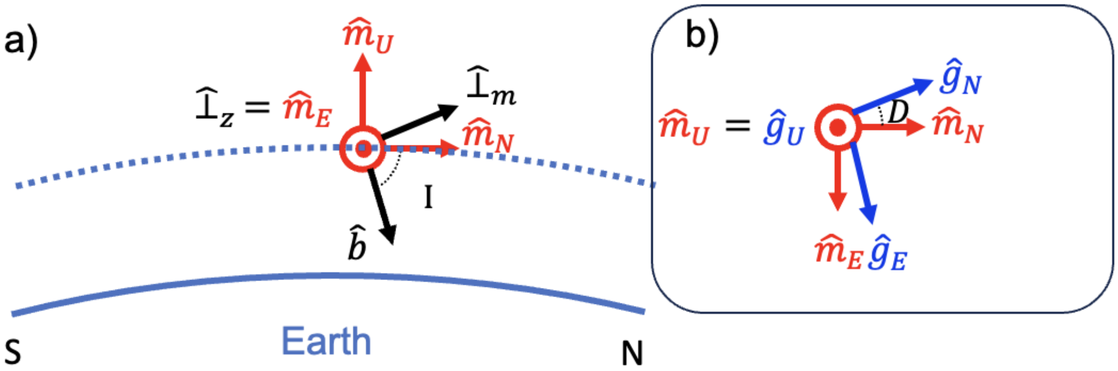

Figure 2.3. (a) Representations for Magnetic field and geomagnetic coordinates. Geomagnetic coordinates are denoted in red text, East-North-Up are labeled as $\hat{m}_E$, $\hat{m}_N$, and $\hat{m}_U$ respectively. Field coordinate axes are in field-perpendicular zonal ($\hat{\perp}_z$), field-parallel ($\hat{b}$), and field-perpendicular meridional ($\hat{\perp}_m$) directions. Rotation angle is the inclination angle I between $\hat{m}_N$ and $\hat{b}$. (b) Representation for magnetic and geographic coordinates, and geographic East-North-Up are denoted by $\hat{g}_E$-$\hat{g}_N$-$\hat{g}_U$ in blue. The declination angle I is between $\hat{m}_N$ and $\hat{g}_N$.

2.3 EMPIRE

2.3.1 Coordinate transformation.

EMPIRE spatial grids are constructed on geomagnetic coordinates, and the previous subsection 2.2 introduced the leading ion continuity equation in magnetic field coordinates, in which ion velocity is decomposed to two vectors: one in the magnetic-field-perpendicular plane and align with the magnetic field lines. The vector in the magnetic-field-perpendicular plane includes two components of zonal and meridional direction, with the field-perpendicular zonal same as geomagnetic east direction. Fig. 2.3 (a) shows the geomagnetic coordinates of east, north and up directions, labeled in red text as $\hat{m}_E$, $\hat{m}_N$, and $\hat{m}_U$ respectively. The field-perpendicular zonal and meridional directions are noted in black text ($\hat{\perp}_z$ and $\hat{\perp}_m$ correspondingly). Inclination angle I is the angle between magnetic field-align unit vector $\hat{b}$ and $\hat{m}_N$, and is a positive angle for fieldlines pointing toward the Earth. The transformation matrix is formulated in Eq. (C.1) in Appendix C.1.

Another important transformation is from geomagnetic to geographic coordinates, because data are often provided in geographic coordinates. Figure 2.3 (b) indicates that geographic up unit direction ($\hat{g}_U$) is same as $\hat{m}_U$, and geographic north and east are labeled in blue text, $\hat{g}_N$ and $\hat{g}_E$ respectively. The declination angle D measures the rotation angle between $\hat{g}_N$ and $\hat{m}_N$, and positive D indicates $\hat{m}_N$ points east of $\hat{g}_N$ (Figure 2.3 (b) shows positive D). The rotation matrix is constructed in Eq. (C.5).

2.3.2 System setup. Substituting Eq. (2.18) and Eq. (2.20) into Eq. (2.21) and rearranging the terms, the electron density rate is reformulated as Eq. (2.22).

$$\frac{\partial N}{\partial t} - \underbrace{(a_{prod} + a_{loss} + a_{dfsn} + a_{grav} + a_u + a_{exb})}_{a_0} = \delta a_u + \delta a_{exb}. \tag{2.22}$$

The sum of terms obtained from the background models is denoted as a_0. From the background models, the terms a_{dfsn} and a_{grav} are the transport terms due to the diffusive and gravitational effects, respectively. The modeled transport due to the neutral wind effect and ExB drift are a_u and a_{exb}, respectively. In the equation, δa_u and δa_{exb} are the corrections to be estimated in the EMPIRE algorithm. We stack the equations from all grid points together to build a system of equations, denoted with bold text, for the EMPIRE linear system:

$$\frac{\partial \mathbf{N}}{\partial t} - \mathbf{a_0} = \delta \mathbf{a_u} + \delta \mathbf{a_{exb}} \tag{2.23}$$

The difference between electron density rate and background modeled terms, on the left side of Eq. (2.23), is treated as the observation vector $\mathbf{z_{\partial N/\partial t}}$ in Eq. (2.24). The state $\delta\mathbf{x}$ consists of coefficients for a spherical harmonic electric potential corrections and coefficients for a vector spherical harmonic representation of the neutral wind corrections [37, 38]. The linear observation matrix $\mathbf{H}$ maps the state vector $\delta\mathbf{x}$ to the the sum of neutral wind and ExB correction terms $\delta\mathbf{a_u}, \delta\mathbf{a_{exb}}$. The measurement error term in the Kalman filter equation is ϵ.

$$\mathbf{z}_{\partial\mathbf{N}/\partial\mathbf{t}} = \frac{\partial\mathbf{N}}{\partial t} - \mathbf{a_0} = \mathbf{H}\delta\mathbf{x} + \epsilon \tag{2.24}$$

As the velocity is separated into two components parallel and perpendicular to the magnetic field, the observation matrix $\mathbf{H}$ and state vector $\delta\mathbf{x}$ are composed of two block matrices: Electric potential mapping matrix $\mathbf{H_V}$ for $\delta\mathbf{x_V}$, neutral wind mapping matrix $\mathbf{H_u}$ for $\delta\mathbf{x_u}$ in Eq. (2.25). For the neutral wind mapping matrix $\mathbf{H_u}$, obtained from the vector spherical harmonics expansion and its associated coefficients $\delta\mathbf{x_u}$, the full description can be found in [39]. The matrix $\mathbf{H_v}$ is formed in three steps: (1) taking the negative gradient of δV to form $\delta\vec{E}$, (2) crossing that $\delta\vec{E}$ with the $\vec{B}_0$ to form ExB correction drift denoted as $\delta\vec{v}_\perp$, and (3) computing the divergence for the correction transport term δa_{exb}. For the full expression for $\mathbf{H_v}$, please refer to [37].

$$\mathbf{z}_{\partial\mathbf{N}/\partial\mathbf{t}} = \begin{bmatrix} \mathbf{H_V} & \mathbf{H_u} \end{bmatrix} \begin{bmatrix} \delta\mathbf{x_V} \\ \\ \delta\mathbf{x_u} \end{bmatrix} + \epsilon \tag{2.25}$$

For EMPIRE, the error covariance is user-defined relying on the assumption of a Gauss-Markov process. Three assumptions are made: (1) The mean value of error is 0. (2) The error terms are Gaussian distributed with finite variance. (3) Each distinct error term is uncorrelated. Based on these assumptions, the error covariance matrice for electron density rates $\mathbf{R}$ is diagonally distributed as the mathematical representation shown in Eq. (2.26). Here k refers to the analysis time epoch, to be used in the Kalman filter.

$$\mathbf{z_k} = \mathbf{H_k}\delta\mathbf{x_k} + \epsilon_\mathbf{k}, \epsilon_\mathbf{k} \sim \mathcal{N}(\mathbf{0},\, \mathbf{R_k}) \tag{2.26}$$

At the next process time epoch $k+1$, the state vector $\delta\mathbf{x_{k+1}}$ can be updated as a Gauss-Markov process expressed in Eq. (2.27). The state $\delta\mathbf{x_k}$ at time k is the stack of coefficients for electric potential $\delta\mathbf{x_V}$ and neutral wind $\delta\mathbf{x_u}$.

$$\delta\mathbf{x_{k+1}} = \mathbf{\Phi_k}\delta\mathbf{x_k} + \eta_\mathbf{k}, \eta_\mathbf{k} \sim \mathcal{N}(\mathbf{0},\, \mathbf{Q_k}) \tag{2.27}$$

$\mathbf{\Phi_k}$ is the state transition matrix, while $\eta_\mathbf{k}$ is the normally distributed process noise vector with the same assumptions as for measurement noise. The state transition matrix $\mathbf{\Phi_k}$ is defined by an exponential function with respect to process time difference, and τ is a predefined time constant representing the measurement information decay speed.

$$\mathbf{\Phi_k} = \exp(-\frac{t_{k+1} - t_k}{\tau})\mathbf{I}$$

The covariance of the process noise $\mathbf{Q_k}$ is the user-defined background model covariance matrix $\mathbf{P_0}$.

$$\mathbf{Q_k} = \left(1 - \exp(-\frac{t_{k+1} - t_k}{\tau})\right)^2 \mathbf{P_0} \tag{2.28}$$

here the background model covariance matrix $\mathbf{P_0}$ is derived in Appendix B.3.

2.3.3 The modeling of ExB ion motion.

Recall the field-perpendicular component of ion motion in Eq. (2.18). For it, we review the formulation of $\delta\vec{v}_\perp$ here from the work of [37], as it will be needed in later sections. The field-perpendicular correction ion drift $\delta\vec{v}_\perp$ is calculated from the cross product of the negative gradient of electric potential correction δV by EMPIRE and modeled magnetic field $\vec{B}_0$, in Eq. (2.29):

$$\delta\vec{v}_\perp = \frac{-\nabla(\delta V) \times \vec{B}_0}{B_0^2} \tag{2.29}$$

Earth's internally generated magnetic field $\vec{B}_0$ is modeled with the International Geomagnetic Reference Field (IGRF-11) [40], and is largely dipolar. The equation for a dipole field line in units of Earth radii R_e is:

$$L(r,\theta) = \frac{r}{R_e \sin^2\theta} \tag{2.30}$$

and is referred to as the "L shell". The calculation of L-shell $L(r,\theta)$ is defined by Eq. (2.30), in which r is the radial distance, and θ is the centered dipole co-latitude. In EMPIRE, we model the correction electric potential δV as being constant along a field line, assuming plasma flow is unrestricted along the field line. As a result the potential is a function of only two independent variables: L-shell L and centered dipole longitude ϕ.

The correction electric potential δV is modeled in EMPIRE using a spherical harmonic expansion [6]:

$$\delta V(u(L(r,\theta)),\phi) = \sum_{l=1}^{l_{max}} \sum_{m=1}^{l} N_l^m P_l^m(u)[x_c^{lm}\cos(m\phi) + x_s^{lm}\sin(m\phi)] \tag{2.31}$$

In the harmonic expansion, N_l^m is the normalization factor, and P_l^m is the Legendre polynomial, of degree l and order m [37]. The function u is defined in EMPIRE as:

$$u(L(r,\theta)) = -1 + \frac{2}{L_{max} - L_{min}}(L(r,\theta) - L_{min}) \tag{2.32}$$

In Eq. (2.32), L_{min} and L_{max} refer to the minimum and maximum L-shell numbers for the fitting domain. By using the mapping function in Eq. (2.32), the L-shell span of the estimation domain is mapped to the interval $u : [-1, 1]$ [6], over which Legendre polynomials are orthogonal [41].

The coefficients x_c^{lm}, x_s^{lm} from Eq. (2.31) are stacked to form column array $\delta \mathbf{x_V}$, consisting of a sub-array of the cosine coefficients $\mathbf{x_c^{lm}}$ and of the sine coefficients $\mathbf{x_s^{lm}}$:

$$\delta \mathbf{x_V} \equiv \begin{bmatrix} \mathbf{x_c^{lm}} \\ \\ \mathbf{x_s^{lm}} \end{bmatrix} \tag{2.33}$$

The correction perpendicular velocity components at a single location are mapped to centered dipole spherical coordinate components by the block matrices $\mathbf{H}_\perp\mathbf{r}$, $\mathbf{H}_{\perp\theta}$, $\mathbf{H}_{\perp\phi}$. A correction is made to the first derivative of $P_l^m(u)$ for ExB drift correction $\delta\vec{v}_\perp$ is derived in A.1. The detailed derivation of the mapping matrices is reviewed in Appendix B.5.

$$\delta\vec{v}_\perp = \begin{bmatrix} \delta v_{\perp r} \\ \\ \delta v_{\perp\theta} \\ \\ \delta v_{\perp\phi} \end{bmatrix} = \begin{bmatrix} \mathbf{H_{\perp r}} \\ \\ \mathbf{H}_{\perp\theta} \\ \\ \mathbf{H}_{\perp\phi} \end{bmatrix} \begin{bmatrix} \delta \mathbf{x_V} \end{bmatrix} \tag{2.34}$$

The block matrix form of the observation system in Eq. (2.25) is the simplest over-determined system of EMPIRE. The solutions for correction electric potential and neutral winds are indirectly estimated from observations of plasma density rate, usually derived from primarily GNSS TEC. However, when measurements of the drivers themselves are available, the system can be augmented. EMPIRE was augmented with block matrices to include direct measurements of the neutral winds, to improve the estimation of neutral winds themselves [42].

2.4 Storm-related phenomenon

For each storm, the solar wind conditions and geomagnetic indices provide general characteristics. In this work, Ap and Dst indices $[nT]$, proton density $[cm^{-3}]$, solar wind speed $[km/s]$, and the y and z components of the interplanetary magnetic field $[nT]$ in the geocentric solar magnetospheric coordinates (GSM) will be used for describing geomagnetic characteristics. Similar to hourly Dst index, Ap index is the measure of the general level of geomagnetic activity over the globe for a given (UT) day in 3-hour cadence [15], and both indices are provided by the World Data Center (WDC) for Geomagnetism, Kyoto [43, 1]. The solar wind was described by the proton density and velocity measurement of incoming plasma flow. The GSM y and z components of local IMF strength indicate Earth's response to solar activity. The solar wind parameters are archived from the Advanced Composition Explorer (ACE) science center operated by Caltech [2]. ACE was launched on August 25th, 1997 with six high-resolution spectrometers by NASA [44]. The solar wind is measured by the Solar Wind Electron, Proton, and Alpha Monitor (SWEPAM), and the onboard magnetometer (MAG) provides the Earth's magnetic field strength. The obtained data is processed by the ACE Science Center and distributed to the research community. On February 2015, the National Oceanic and Atmospheric Administration (NOAA) Deep Space Climate Observatory (DSCOVR) mission was launched onboard with the PlasMag suite, which includes the solar wind monitoring plasma (Faraday Cup) and magnetometer instruments, the Earth-observing NIST Advanced

Radiometer (NISTAR), and the Earth Polychromatic Imaging Camera (EPIC) [45]. The DSCOVR mission provides IMF and solar wind characteristics for NOAA space weather predictions, starting from June 2015. Hence, the storm that occurred afterwards is described from DSCOVR data [46, 3].

2.4.1 NILE.

During certain geomagnetic storms, a distinct region of heightened TEC at northern midlatitudes has been consistently observed, co-rotating with the Earth during the late evening hours, typically from around 18:00 LT to 24:00 LT. This phenomenon is referred to as the NILE. The compact nature of NILE poses challenges to differential GNSS augmentation systems that aim to ensure user integrity. In the initial identification of this phenomenon, initially termed the "Florida effect," ground-based multi-frequency GNSS measurements were collected from nearly 400 receivers. These measurements were then used to generate Vertical Total Electron Content (VTEC) maps for the extreme storm in October 2003 [20]. The concentration of TEC and its persistent nature prompted the development of the Extreme Storm Detector in the Federal Aviation Administration (FAA) Wide Area Augmentation System (WAAS) for aircraft navigation [47].

A study of the NILE during the August 2018 and November 2003 storm events utilized the data assimilation tool IDA4D [26] coupled with the ionosphere model SAMI3 [32]. This study revealed the evolution of NILE in terms of occurrence time and region, supported by GPS and ionosonde validations [21]. In comparison to the more concentrated and severe mid-latitude effects observed during the October 2003 storm, the mid-latitude events in August 2018 and November 2003 were found to be less spatially extensive and less intense in density. This raised the question of whether the effects observed during these storms could be classified as NILE. To gain a deeper understanding of the driving mechanisms behind NILE, it is crucial to assess major ionospheric factors during storm periods, including electric fields and neutral winds that contribute to ion drift motion. In order to better characterize the NILE phenomenon, efforts are being made to identify the underlying electromagnetic mechanisms that give rise to it. One proposed explanation for the formation of NILE is the concept of the polarization terminator [48]. The polarization terminator incorporates theories related to the pre-reversal enhancement (PRE) [49] and the equatorial ionization anomaly (EIA) [50], particularly those associated with the dusk terminator. This combination generates an electric field and induces plasma drifting mechanisms during storm times. [31] validated neutral wind meridional behaviors might be a contributing factor EIA asymmetry related to NILE phenomenon.

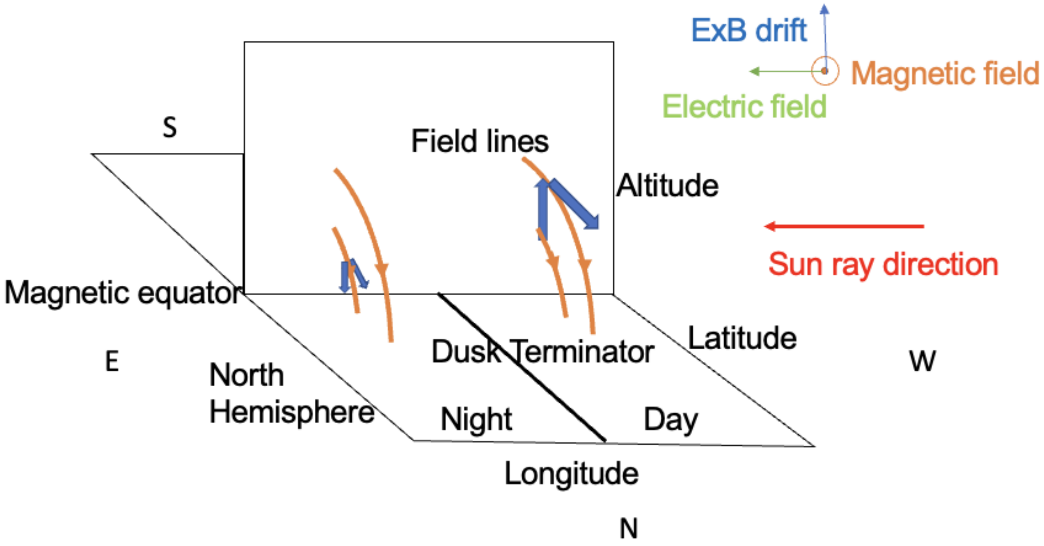

Figure 2.4. A simplified representation of plasma drifts (blue arrows) under the PRE effect. The orange curves indicate magnetic field lines. Blue arrows are the directions of plasma motion, given by the cross product of electric field (green) and magnetic field (orange). Dayward of the dusk terminator, the plasma is uplifted and diffuses along the magnetic field-lines. Downward motion is induced on the night side of the terminator.

2.4.2 Pre-reversal Enhancement (PRE).

PRE phenomenon takes place at low magnetic latitudes and involves an eastward electric field that intensifies before sun-

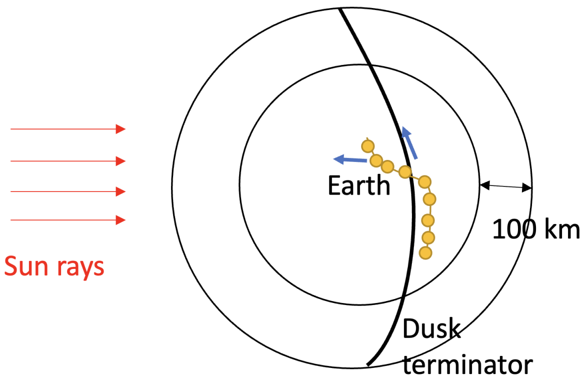

Figure 2.5. A simplified plot of the polarization terminator. The dusk terminator is drawn at the 100 km shadow height. The field lines passing through the dusk terminator in the southern hemisphere are marked as yellow dots. Due to the penetration of electric field during the storm time, the tracing points of the field-lines are also presented as the yellow dots in the day time. The polarization terminator is defined by connecting the yellow dots.

set, followed by a westward electric field after dusk. PRE enhances the EIA, which is a daily scenario that equatorial plasma is transported and accumulated at the magnetic latitudes of ±20° [51]. The pre-dusk eastward electric field uplifts the equatorial ionosphere to altitudes 100 kilometers or more above its typical position. Subsequently, as the plasma drifts upward, it diffuses along the magnetic field lines, typically within ± 15-20 degrees off the dip equator, a region known as the Appleton anomaly [52]. As the sunset terminator progresses, the conductivity in the E region decreases, leading to a downward plasma motion for the remainder of the nighttime and attenuating the Appleton anomaly phenomenon [49]. While the Appleton anomaly is a common occurrence, the PRE involves a stronger eastward field, resulting in more uplift than usual. During storms, it has been suggested that extreme uplift may occur, manifesting as a “super-fountain” effect, as observed during the “Halloween” storm in November 2003 [53]. Figure 2.4 provides a simplified illustration of the plasma drifts associated with the PRE mechanism.

2.4.3 Polarization Terminator (PT). PT illustrated in Figure 2.5 is defined as a distorted dusk terminator, determined based on the E-region shadow height at either end of the field line corresponding to 100 km [54]. The PT delineates the electric field driving mechanism, causing the plasma to drift upward. This induces a westward electric field on the west side of the PT and directs the motion toward the polar region on the east side of the PT [48]. According to [21], the plasma is hypothesized to be transported into the American sector due to the upward and poleward motion induced by the PT, potentially contributing to the NILE phenomenon. Our objective is to investigate whether westward and poleward (i.e., northward) motion is observed in the vicinity of NILE.

CHAPTER 3

REPRESENTATION ERROR COVARIANCE MATRICES IN EMPIRE KALMAN FILTER

This chapter was previously accepted by AGU Space Weather journal for publication [4].

Space weather forecasting is extremely desirable for alerting about geomagnetic storms, since forecasts can give operators of technological systems affected by space weather time to react to minimize the impact of these events. Data assimilation algorithms combine regional measurements with global background models to improve estimation and forecasting of a state, and can be used for space weather analysis.

Data assimilation methods have been developed to study the ionosphere. Different studies [55, 56, 57, 58, 59, 60, 61, 62] have estimated the ionospheric density by ingesting GNSS global TEC measurements. The application of particle filter in Assimilative Canadian High Arctic Ionospheric Model (A-CHAIM) provides high-latitude ionosphere from ingesting slant TEC data from ionosondes and GNSS receivers, and vertical TEC from JASON-3 altimeter [63]. Global TEC measurements is also ingested to update the background model International Reference Ionosphere (IRI) [64]. [65] developed IRI Real-Time Assimilative Mapping (IRTAM), which also updates IRI in real time but by ingesting Global Ionospheric Radio Observatory (GIRO) data.

Efforts to estimate the plasma drivers in the coupled IT system, e.g. neutral winds and ion drifts, have been used before too. [66] updates the model TIEGCM by ingesting thermospheric temperatures. Additional examples of data assimilation algorithms are Assimilative Mapping Ionospheric Electrodynamics (AMIE) algorithm [67], Assimilative Mapping of Geospace Observations (AMGeo) [68], and the DART [30]. The Active Magnetosphere and Planetary Electrodynamics Response Experiment (AMPERE) applied to Iridium measurements improved the comparison of magnetic perturbation data from LEO satellite constellations [69]. [70] ingest ICON measurements of the neutral winds to update the outputs of the system WACCMX+DART. [71] also updates this model by ingesting GOLD thermospheric temperatures. The previous algorithms ingest measurements of the plasma or neutral parameters themselves to improve the model estimations. These measurements in some cases are less plentiful than, for example, global TEC measurements. There have been studies of data assimilation algorithms that estimate the plasma drivers by ingesting global TEC measurements, such as GAIM-FP (Full Physics) model [59, 72]. [73] have developed the Thermospheric Wind Assimilation Model (TWAM), that updates the winds from GAIM-FP at low and mid-latitudes.

There are different sources of error in data assimilation systems in general, such as the assumption of unbiased errors, the inaccuracy of the background climate models used, or the errors of the observations. Understanding, modeling, and quantifying the different uncertainties associated with data assimilation algorithms is necessary for the optimal use of the method [74]. By specifying the observation and model error statistics correctly, the states obtained from data assimilation algorithms can be further improved to capture atmospheric variabilities [75].

Errors of methods focused on studying the IT have been analyzed for specific assimilation methods. [59] have studied the model error of the GAIM-FP model. [76] and [77] study the model systematic bias of the TIEGCM algorithm and of a four-dimensional local ensemble transform Kalman filter (4D-LETKF) respectively. Calibration of the background climate models was analyzed by [78]. A method to estimate and account for the model error was also developed by [79].

Different studies to assess how well data assimilation algorithms work have been conducted. [80] analyzes the impacts of model, background and observation error produced by a data assimilation algorithm using a variational error estimation method [81]. [82] and the references within analyzed a method to determine the systematic model bias in ensemble Kalman filters.

One of the main challenges in data assimilation is to characterize the errors from discrepancies between observations and the physics-based model used in the data assimilation algorithm to describe them [83]. This error includes the representation error, which describes the error of using a discrete physical model that is not able to represent all the scales [84] and all the physical processes and dynamics of a system [85]. [85] describes 3 main sources for the representation error: errors due to different scales represented in the observations and the model, due to the observation operator used to convert measurements into state space, and due to quality control or pre-processing of observations. Specifically, [85] defines pre-processing error as distinct from measurement errors by being due to obtaining derived quantities from the instrument measurement, such as retrieval of atmospheric variables from satellite radiance.

Note that this contribution ties work begun in Chapter 4 of [31], to literature review and error statistics. The goal of this study is to define a method to, and then quantify, the representation error of an IT data assimilation algorithm that estimates electric potentials and neutral winds globally from density rates. We focus on the algorithm EMPIRE [86], which estimates the ionospheric convective drivers of neutral wind and electric potential by ingesting global electron density. Input densities have typically been derived from another data assimilation algorithm: IDA4D [58], which ingests primarily GNSS TEC measurements, and interpolated onto EMPIRE grid for ingestion. The ingesting spatial data processed from another algorithm instead of raw measurements includes reducing the interpolation or extrapolation errors. EMPIRE estimations might be biased due the sparsity of raw measurements, if the information gap source was not on a global scale. EMPIRE separates the estimation of the drivers from the estimation of plasma density, allowing EMPIRE to have a more robustly-conditioned observation operator.

In previous work [87, 88, 89, 90], the drivers have been estimated and studied during different geomagnetic events, but they have not focused directly on an assessment of the error of the estimations. [38] transitioned from using power series-based neutral wind basis functions to vector spherical harmonics. In that work, the representation errors were not considered, and the model error covariances were pre-processed and fixed as constants. The goals of the analysis in this work are to incorporate representation error in the EMPIRE filter and to give context to future conclusions made from interpreting the outputs.

The governing equation in EMPIRE is the ion continuity equation of ionized atomic oxygen (O^+), as this ionized species primarily dominates the F layer ionosphere in which plasma density peaks. The EMPIRE observation equation is a simplification of the behavior that excludes chemistry, as well as momentum and energy physics of the plasma. This reduction of the physics to the ion continuity equation and finite state basis functions will each introduce a representation error in the algorithm. The objective of this work is to quantify the representation error and then analyze how well EMPIRE, by reducing the observation operator to the ion continuity equation for one species, is able to predict the global ionospheric drivers.

To achieve the objective we use a self-consistent source that supplies both the background model and simulated measurements that EMPIRE assimilates, as well as the validation "truth" with which to compare the resulting estimates. A perfect representation of the ionosphere to use as this source does not exist, but we will use a background model as if it were, and it will be considered as our "truth." The self-consistent physics model that we use is the SAMI3 algorithm [91]. SAMI3 models the ionosphere by solving the continuity and momentum equations of seven different ion species (H^+, He^+, N^+, O^+, NO^+, N_2^+ and O_2^+) and the energy equations of three of them (H^+,He^+ and O^+). Comparing the results to the chosen self-consistent model, we see how well the EMPIRE simplification of considering only the ion continuity equation captures the dynamics. This comparison and characterization of the representation error will help us understand the strengths and limitations of the data algorithm. The methodology can then be applied in future runs to concurrently estimate a more accurate error covariance.

Section 3.1 discusses representation error estimation and algorithm performance analysis for this study. Section 3.2 describes the synthetic data used to run the EMPIRE algorithm as well as the configuration parameters for EMPIRE. Analysis of the EMPIRE results is shown in Section 3.3. Section 3.4 presents the main conclusions.

3.1 Representation error covariance re-construction

Observation error is an essential component that needs to be well-defined in the data assimilation algorithm. Other than the measurement error that might be due to the surrounding environment and instruments, [85] also noted that because of the representation error, which is associated with unresolved scales and the observation operator, there should be another error term in the modeling of observation error covariance $\mathbf{R}$. Figure 3.1 conceptually explains the relationship between the real physical system $\mathcal{H}(x)$ ("Real world"), linear approximations $\mathbf{H}\hat{x}$ ("Model world") and corresponding measurements y in the observation space. The error between true and modeled variables is the representation error ϵ_{rep} with error covariance $\mathbf{R_{rep}}$. The measurement error between the truth and measured quantity y is denoted as ϵ_{msmt}

with error covariance $\mathbf{R_{msmt}}$. The sum of these two error sources is the observation error ϵ in data assimilation with covariance $\mathbf{R}$, as in Equations (3.1)-(3.2).

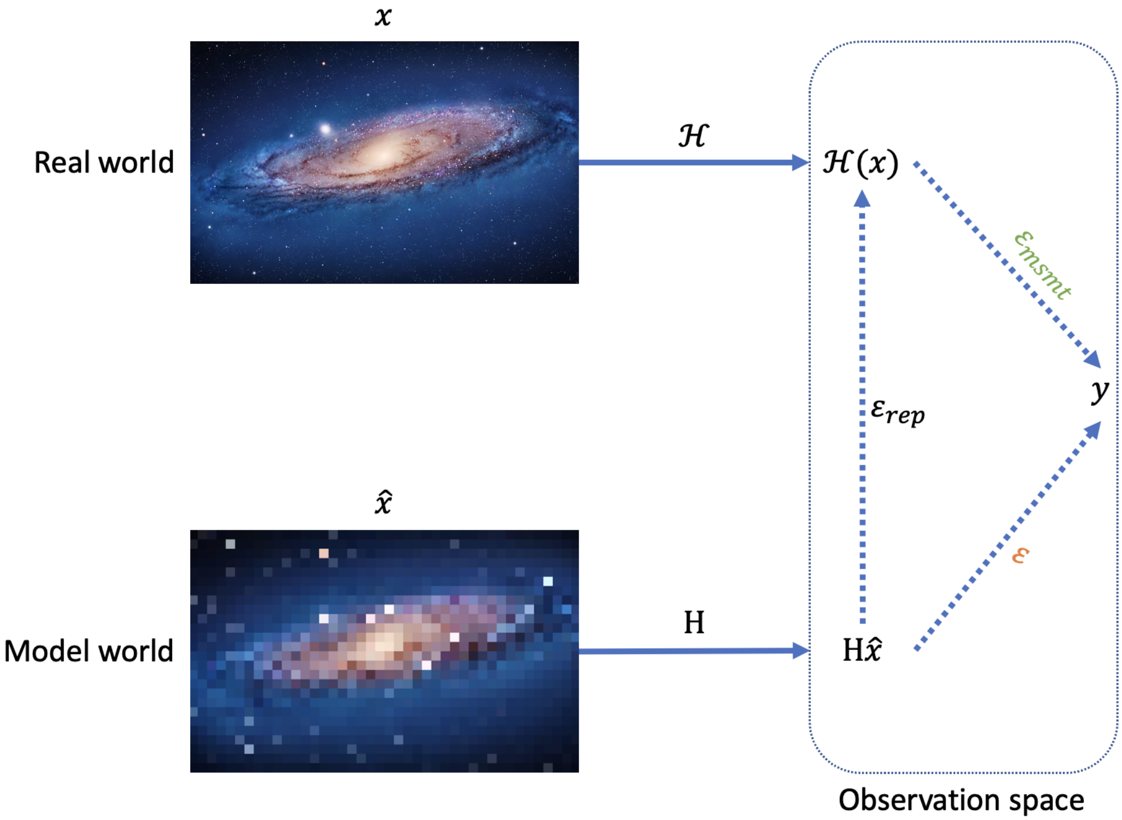

Figure 3.1. Conceptual relationship among the real world, model world, and the corresponding observations. Photo images are retrieved from [92]. The real world is described by true state x transformed by the relationship $\mathcal{H}$, modeled variables are the estimated state vector $\hat{x}$ mapped by the linearized transformation matrix H, and y is the measurement vector. The difference between the true and modeled world are represented in error ϵ_{rep} (black). The difference between the true world and the measurement is measurement error ϵ_{msmt} (green). The sum of these errors is the observation error ϵ (orange).

$$\epsilon = \epsilon_{rep} + \epsilon_{msmt} \tag{3.1}$$

$$\mathbf{R} = \mathbf{R_{rep}} + \mathbf{R_{msmt}} \tag{3.2}$$

In previous EMPIRE implementation [31], we neglected the representation error, so $\epsilon_{\mathbf{rep}}$ and $\mathbf{R_{rep}}$ were zero. [31] did the representation error quantification for EMPIRE performance, but did not formulate the error source into the algorithm implementations. In the present study, we consider both the representation error ϵ_{msmt} and the measurement error ϵ_{rep} in the EMPIRE framework. These errors are assumed to follow a normal distribution and have error covariances $\mathbf{R}_{\mathrm{msmt}}$ and $\mathbf{R}_{\mathrm{rep}}$, respectively.

The representation error ϵ_{rep} distributed with $\mathbf{R_{rep}}$ in the present study will be analyzed numerically. Let δx be the true state, which may be infinitely long. The unresolved scales arise from truncating δx to be discrete and finite $\delta \mathbf{x}$. Let $\mathcal{H}$ be the "true" relationship to the true state, which may be a non-linear function or have unknown physics. The matrix $\mathbf{H}$ is a linearization of the known relationships in $\mathcal{H}$ that by definition does not include unknown physics and may even leave some known physics unmodeled. In EMPIRE, the linearization of physics model and the assumption of a single ion species of O^+ in EMPIRE algorithm setup should also be attributed to the observation error ϵ. Specifically, the [93] model is used to specify the production, loss, gravity and diffusion effects ($a_{loss,0}$, $a_{prod,0}$, $\vec{v}_{grav,0}$ and $\vec{v}_{dfsn,0}$) in EMPIRE. The representation error $\epsilon_{\mathbf{rep}}$ that we want to characterize for the data assimilation algorithm EMPIRE comes from the discrepancy between the true observation $\mathcal{H}(\delta \mathbf{x})$ and an estimate $\mathbf{H}\delta\hat{\mathbf{x}}$ (see Figure 3.1) from the ion continuity equation:

$$\epsilon_{\mathbf{rep}} = \mathcal{H}(\delta \mathbf{x}) - \mathbf{H}\delta\hat{\mathbf{x}}$$

In general use, we cannot know $\mathcal{H}(\delta \mathbf{x})$ exactly. However, in this work, we create a simulated truth to approximate the representation error due to the observation operator and unresolved states, and we treat the pseudo-observation $\mathbf{z}$ as the "truth" $\mathcal{H}(\delta \mathbf{x})$. Let us assume the error ϵ_{rep} is normally distributed with representation error covariance $\mathbf{R_{rep}}$:

$$\epsilon_{\mathbf{rep}} = \mathbf{z} - \mathbf{H}(\mathbf{H}^{\dagger}\mathbf{z}) \tag{3.3}$$

$$\mathbf{R_{rep}} = diag[(std(\epsilon_{\mathbf{rep}}))^2] \tag{3.4}$$

where the estimate of $\delta\hat{\mathbf{x}}$ is calculated with the Moore–Penrose inverse operator is denoted with the super-scripted dagger.

Since the electron density rates are assumed to be exact from a self-consistent source, the electron density rate error covariance matrix is considered to be zero.

$$\mathbf{R_{msmt}} = \mathbf{R_{a0}} + \underbrace{\mathbf{R_N}}_{\mathbf{0}} \tag{3.5}$$

Independently from the setup of observation error covariance $\mathbf{R}$, the $\mathbf{P_0}$ [38] was constructed with pre-processed (i.e., before the EMPIRE Kalman filtering) background model variance thereby losing any time-dependent variation. In this study, the model covariance $\mathbf{P_0}$ for this study is reformulated in B.3, concurrently updating the model information to the EMPIRE system.

In the analysis of how EMPIRE performs, after numerically quantifying $\epsilon_{\mathbf{rep}}$, $\mathbf{R_{rep}}$ and $\mathbf{P_0}$ as inputs to the EMPIRE Kalman filter, the true values are compared with the ion drifts and neutral wind estimated from $\delta\hat{\mathbf{x}}_{\mathbf{k}}^{+}$. For an individual component in field-perpendicular zonal and meridional, and field-aligned directions $\mathbf{v_i} = \{v_{\perp,z}, v_{\perp,m}, u_{\|}\}$, our "truth" is known and the residual in the velocity space $\epsilon_{\mathbf{v_i}}$ can be characterized by comparing the estimates $\hat{\mathbf{v}}_{\mathbf{i}}$ to the original values that are self-consistent with the data that were ingested:

$$\epsilon_{\mathbf{v_i}} = \mathbf{v_{i,true}} - \hat{\mathbf{v}}_{\mathbf{i}} \tag{3.6}$$

where $\epsilon_{\mathbf{v_i}}$ is the analysis error of each individual component $\mathbf{v_i}$. For ExB drifts ($\mathbf{v_i} = \{v_{\perp,z}, v_{\perp,m}$), which are projected from ion drifts in geomagnetic radial ($v_{\perp,r}$), co-latitudinal ($v_{\perp,\theta}$) and longitudinal ($v_{\perp,\phi}$) directions, and $\hat{\mathbf{v}}_\mathbf{i}$ is the sum of EMPIRE correction $\delta\mathbf{v_i}$ and model calculation $\mathbf{v_{i,0}}$. For neutral wind $\mathbf{v_i} = \{u_\parallel\}$, the analysis error $\epsilon_{\mathbf{vi}}$ is the EMPIRE correction alone because Horizontal Wind Model (HWM) 14 neutral wind serves as the background model inputs and the validation truth, and is projected onto the field-parallel direction.

3.2 Experimental setup

The goal of this study is to quantify the representation error in density rate space as Eq. (3.3), in which $\mathbf{H}$ is the mapping function from coefficients to time-differenced density $\frac{\mathbf{dN}}{\mathbf{dt}}$, and $\mathbf{z}$ is the gap between measurements and modeled electron density rates. Another goal is to analyze the performance in velocity space $\epsilon_{\mathbf{v_i}}$ in Eq. (3.6) in response to different geomagnetic activity levels, for a quiet day and a storm day. To do this we use a self-consistent source to provide the measurements N, and background $\mathbf{a}_0$. The self-consistent source used to estimate the representation error ϵ_{rep} of EMPIRE in this study is SAMI3. The magnetic field is provided by the IGRF model [91] and the electric field is solved with a potential solver derived from current conservation [94]. The ion drift is calculated self-consistently with the solved perpendicular electric field in the low to mid-latitude region of the ionosphere. At high latitudes, SAMI3 uses the [95] model. The neutral winds are obtained from HWM14 [96], including DWM (Disturbance Wind Model) when the Kp index reaches a certain threshold. The neutral properties are characterized by the NRL-MSISE00 model [97]. The continuity and momentum equations of seven different ion species (H^+, He^+, N^+, O^+, NO^+, N_2 and O_2^+) and the energy equations of three of them (H^+, He^+ and O^+) are used to represent the ionosphere. In summary, SAMI3 is driven by Weimer, HWM14 and NRLMSISE00 just as EMPIRE's background is.

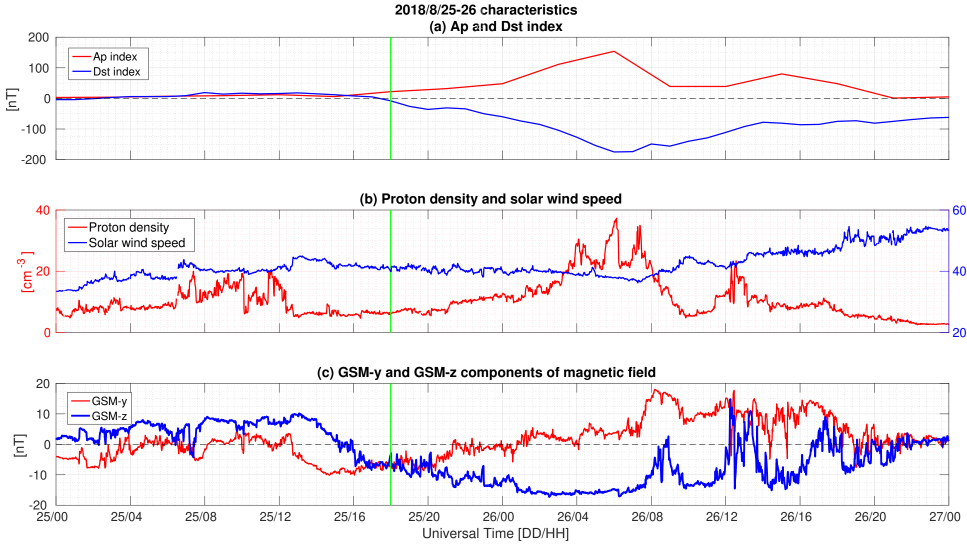

Figure 3.2. Solar wind and geomagnetic conditions 25-26 August 2018. (a) Ap and Dst indices in units of nT, represented by red and blue lines, respectively. The raw data used for subplot (a) is obtained from World Data Center for Geomagnetism [43]. (b) Proton density in units of cm^{-3} and solar wind speed in km/s, shown by red and blue lines, respectively. (c) Interplanetary magnetic field y and z components in GSM coordinate, in units of nT. The vertical green line at 18 UT August 25th separates the quiet period from the storm period being investigated. The raw data for subplots (b) and (c) are obtained from DSCOVR satellite observations [3]. The horizontal dashed line indicates 0 nT in (a) and (c).

A case that is primarily a quiet day is selected for this study, 25 August 2018, and the subsequent day is selected as a storm day. Figure 2 plots (a) the Ap and Dst indices, (b) the solar wind density and speed, and (c) IMF By and Bz components for these dates. Given the classification by [98], a quiet-minor event corresponds to an Ap index between $0-20$ nT while indices from $30-50$ nT corresponds to a moderate storm. The Ap index reaches values higher than 20 nT between 17 UT and 18 UT, and afterward the index starts to increase, indicating that the geomagnetic storm starts to develop. Figure 3.2 also indicates that 18 UT is the beginning of the main phase as the Dst index drops below zero. The interplanetary magnetic field Bz turns southward reaching -10 nT at 17 UT. We consider the storm time period as being after 18 UT on 25 August 2018.

SAMI3 values of the electron density N at altitude range from 100 km to 3000 km will be used as the pseudo-measurements in the data assimilation algorithm. The electron density N from SAMI3 is then finite differenced to obtain the electron density rate $\partial N/\partial t$, that EMPIRE ingests. Also, in EMPIRE we use the same background models that SAMI3 uses, to make all the sources that EMPIRE ingests consistent with SAMI3. The IGRF-11 model [99] is used to describe the magnetic field $\vec{B}_0$. The neutral wind is modeled by the updated HWM14 [96]. The neutral properties will be given by the NRL-MSISE00 model as in SAMI3. Also, the electron and ion temperature are provided by the IRI model, instead of by the SAMI3 output values, as they were not available for the chosen cases. The temperatures are inputs to the calculation of collision frequency, diffusion coefficient and loss term in the ion continuity Equation (Eq. (2.21)) of the Kirchengast model [86, 89]. The impact of ion temperature variations is negligible to calculations of the loss term [86, 100]. It is shown in Appendix B.4 that the diffusion coefficient and collision frequency are not very sensitive to a change in these temperatures, so using IRI instead of SAMI3 will not change the EMPIRE estimation.

A block diagram of how SAMI3 is fed in and subsequently compared to EMPIRE is shown in Figure 3.3. We run EMPIRE with the newly derived observation covariance $\mathbf{R}$ as defined in Eq. (3.2), with $\mathbf{R_{rep}}$ formulated by treating the difference between SAMI3 electron density rates and background modeled values as $\mathbf{z}$ in Equation (3.4). The $\mathbf{R_{msmt}}$ is only due to the error source of background models $\mathbf{R_{a0}}$. Large uncertainties are expected for model outputs during storms, thus $\mathbf{R_{a0}}$ in Eq. (3.5) is assumed to be 70 percent of the sum of background modeled values $\mathbf{a_0}$.

$$\mathbf{R_{a0}} = 70\%\mathbf{a_0}$$

Note that $\mathbf{R_{a0}}$ is assumed to be a diagonal matrix in this study. We acknowledge that ionospheric states are highly correlated [101], such as strongly divergence-free flow at high latitudes [102] and spatially correlated neutral densities and temperature [103]. In a realistic setting, $\mathbf{R_{a0}}$ should be constructed with off-diagonal terms indicating the spatial and temporal correlations between states. One reason for our simplification is that the background models only yield global values at each time epoch, without providing information on the standard deviation and correlation. Another reason to assume that $\mathbf{R_{a0}}$ is a diagonal matrix in this work is to reduce the computational cost of matrix inversion. However, the setup of diagonal error matrices in a Kalman gain calculation can lead to biased weight on the innovation vector $(\mathbf{z_k} - \mathbf{H}\delta\hat{\mathbf{x}}_{\mathbf{k}}^{-})$ in Eq. (2.12), and loss of information in state correlation, which yields less optimal estimates of posterior state $\delta\hat{\mathbf{x}}_{\mathbf{k}}^{+}$.

After adjusting the error covariance, the correction state $\delta\hat{\mathbf{x}}$ is estimated by the Kalman filter, and EMPIRE estimated ion drifts are compared with the ion drifts from the sum of SAMI3 and Weimer for validation purposes, since Weimer supplies the high-latitude electric potentials and SAMI3 solves for electrodynamics in the low-to-mid latitudes. The estimated neutral wind correction $\mathbf{F_u}\delta\hat{\mathbf{x}}_{\mathbf{u}}$ [38] is compared with u produced by HWM14 model since SAMI3 is driven by HWM14.

The difference $\epsilon_{\mathbf{vi}}$ between the EMPIRE-estimated drivers and the SAMI3 values will be computed using Eq. (3.6) to assess mean and standard deviation of the representation error in velocity space of EMPIRE.

A global analysis is performed using a grid of magnetic co-latitude θ between 3 and 177 degrees with a resolution of 6 degrees, magnetic longitude ϕ between -180 and 180 degrees with a step of 6 degrees and altitude h between 200 km and 500 km with a step of 50 km. The grid has 12810 points at each time step. The analysis period spans 48 hours starting at 0 UT on 25 August 2018 at 15-minute increments.

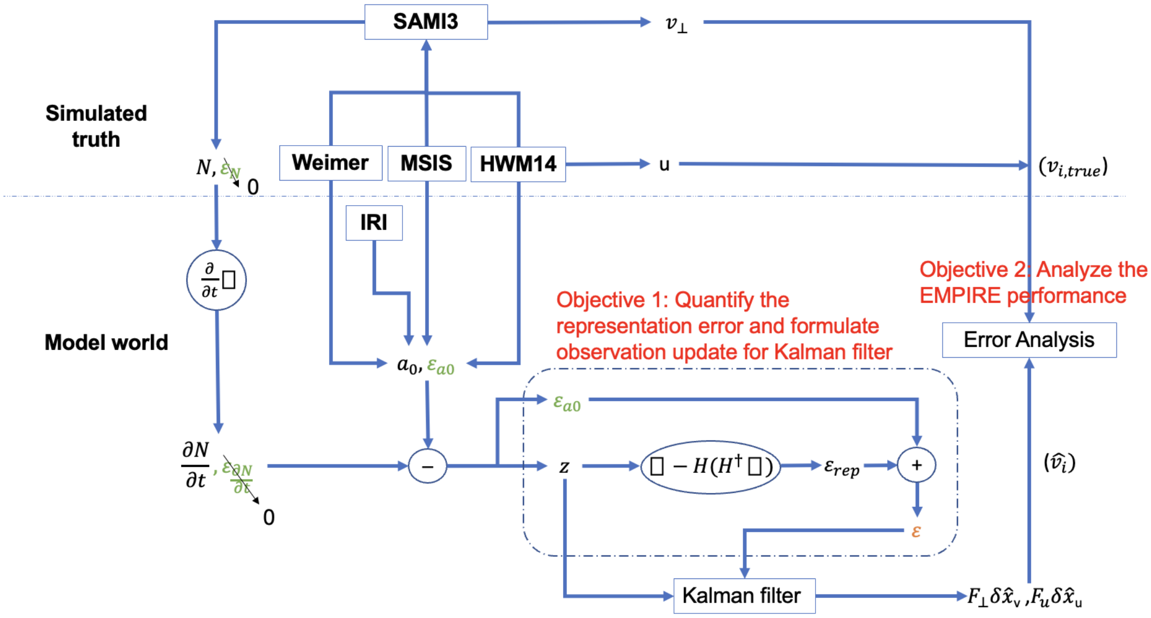

Figure 3.3. Block diagram of EMPIRE representation error quantification relative to SAMI3 as the self-consistent truth source. The electron density rate $\partial N/\partial t$ is obtained from the electron density N from the SAMI3 model, and the time-differencing error is $\epsilon_{\partial N/\partial t}$, counted as one component of measurement error. Another measurement error ϵ_{a_0} is due to the background modeled term a_0, which is modeled by Weimer, HWM14, IRI and MSIS. The gap between $\partial N/\partial t$ and a_0 is treated as the measurement vector. The representation error ϵ_{rep} is analyzed as an error source in observation error ϵ. Errors are color-coded to correspond to their roles in Figure (1).

Once the filter is configured as described, the state is estimated with EMPIRE at each time step using Equations (2.12) and (2.15). Then the estimated ion drifts and neutral winds are obtained at every grid point for the desired period of time.

To assess the effects of representation error on the ion drifts, we compare our results to the SAMI3 drift output following Eq. (3.6) in the perpendicular-to-the-magnetic-field zonal and meridional component directions. The zonal mean of the difference between the background (Weimer) plus EMPIRE estimate and SAMI3 values of the two components, perpendicular meridional $\bar{\epsilon}_{v_{\perp_m}}$ and zonal $\bar{\epsilon}_{v_{\perp_z}}$ to the magnetic field line direction, will be shown over time and magnetic latitude at an altitude of 300 km.

$$\bar{\epsilon}_{v_i}(\theta; t) = \frac{1}{n_\phi} \sum_{\phi=-180}^{\phi=180} \epsilon_{v_i}(\theta, \phi; t) \tag{3.7}$$

where ϵ_{v_i} is the representation error in velocity space defined as each element of in Eq. (3.6), the magnetic longitude step is 6 degrees and the number of magnetic longitudes used in the EMPIRE grid is $n_\phi = 61$.

For the neutral wind estimation, the parallel-to-the-field neutral wind is decomposed into geographic east and north. In this work the geographic east transport due to neutral wind is assumed 0 (i.e. not corrected) because in general field lines are oriented largely in the meridional plane. To study the neutral wind representation error we will compare our results to the HWM14 model, as it is the neutral wind input that SAMI3 uses, also following Eq. (3.6). The geographic meridional direction is analyzed using the zonal mean difference between the estimation and the values from HWM14 that drove SAMI3, of the component, which will be projected onto the field-parallel direction $\bar{\epsilon}_{u\|}$ as EMPIRE only observes neutral wind parallel to the magnetic field lines. They will also be calculated at the altitude of 300 km. The zonally averaged difference for all of the terms will be calculated at each time and magnetic colatitude using Eq. (3.7).

The mean and standard deviation of the difference between the estimation of each of the components of the drivers and the model SAMI3 will also be calculated to assess the representation error in the EMPIRE velocity space, which will be easier to interpret than ϵ_{rep} in density rate space. They will be calculated over magnetic latitude by taking the zonal mean $\mu_{\epsilon_{v_i}}(\theta)$ and the standard deviation $\sigma_{\epsilon_{v_i}}(\theta)$ over longitude and time:

$$\mu_{\epsilon_{v_i}}(\theta) = \frac{1}{n_{times}} \sum_{t_0}^{t_f} \sum_{\phi=-180}^{\phi=180} \epsilon_{v_i}(\theta, \phi; t)$$

Zonally averaged difference $\bar{\epsilon}_{vi}(\theta;t)$ [SAMI3 - EMPIRE]

(a) Perp-zonal $\bar{\epsilon}_{vi}(\theta;t)$

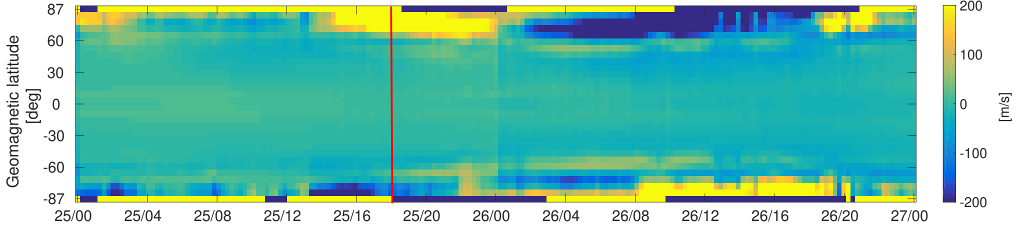

(b) Perp-meridional $\bar{\epsilon}_{vi}(\theta;t)$

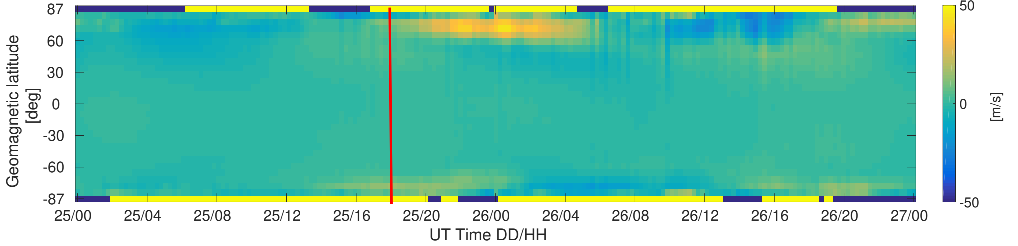

Figure 3.4. Zonally averaged differences between SAMI3 and EMPIRE correction of ion drifts in the (a) field-perpendicular zonal and (b) field-perpendicular meridional directions. The red vertical line separates the quiet and storm periods: 00 UT to 18 UT August 25th is the quiet period, and 18 UT August 25th to 00 UT August 27th is the storm period.

$$\sigma_{\epsilon_{v_i}}(\theta) = \left(\frac{1}{n_{times}} \sum_{t_0}^{t_f} \sum_{\phi=-180}^{\phi=180} \left[\epsilon_{v_i}(\theta,\phi;t) - \mu_{\epsilon_{v_i}}\right]^2 \right)^{1/2}$$

where n_{times} is the number of time steps. During quiet time $n_{times} = 72, t_0 =$0 UT on 25 Aug, and $t_f =$18 UT on 25 Aug. For the storm period, the error statistics are calculated similarily, with $t_0 =$18 UT August 25th, $t_f =$24 UT August 26th, giving $n_{times} = 120$.

3.3 Results

To characterize the representation error as projected into velocity space ϵ_{v_i}, we study the difference between EMPIRE and SAMI3 outputs over time over the whole global region, and we also study the dependence of the results on latitude. Figure 3.4 shows the zonally averaged ion drift difference $\bar{\epsilon}_{v_i}$ of Eq. (3.7) over time in the (a) perpendicular zonal direction and in the (b) perpendicular meridional di-

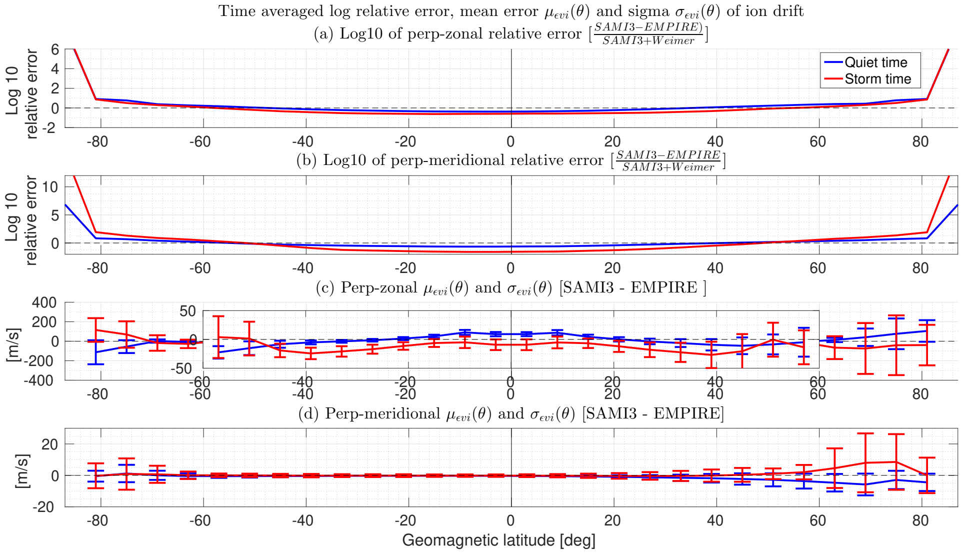

Figure 3.5. The time averaged ion drift relative errors on a log base-10 scale versus geomagnetic latitude are presented in (a) field-perpendicular zonal direction and (b) field-perpendicular meridional direction. The horizontal dashed line in (a) and (b) indicate that the relative error is 100%. The time-averaged error $\mu_{\mathbf{\epsilon vi}}(\theta)$ and standard deviation $\sigma_{\mathbf{\epsilon vi}}(\theta)$ between SAMI3 and EMPIRE corrected ion drifts versus magnetic latitude are plotted in the field-perpendicular (c) zonal and (d) meridional directions. The horizontal dashed line indicates 0 velocity components. The figure (c) inset plot zoom in on the mean error at the low-to-mid latitudes. For all of the subplots, the vertical black line is the 0° latitude line. Quiet and storm time error statistics are plotted with blue and red lines, respectively.

rection between EMPIRE results and SAMI3 “true” values. The perpendicular zonal direction coincides with the magnetic $\hat{\phi}$ direction. Positive values, in yellow, indicate EMPIRE+Weimer model is smaller than SAMI3+Weimer modeled values. Negative values in blue indicate overestimation by EMPIRE compared to the SAMI3 values. The parallel ion velocity is not shown, as the ion drift is only seen in the field-perpendicular field direction. We consider the quiet time interval as lasting until 18 UT.

In the perpendicular zonal direction, Figure 3.4 (a), the error is small at low-to-mid latitudes up to around ±60° magnetic. The magnitude of $\bar{\epsilon}_{vi}(\theta; t)$ increases dramatically poleward 60°, which indicates that EMPIRE does not provide as accurate zonal ion drift information in the high latitude bands. The estimation in the perpendicular meridional direction, shown in the Figure 3.4b, is close to the model SAMI3 values, as the error is close to 0 m/s in almost all regions except at boundary latitude of ±87°. We can see a higher disagreement saturating at the boundary latitudes of ±87° over time.

Figure 3.5 plots the relative errors $\mu_{\epsilon vi}(\theta)$ on a $\log_{10}$ scale at each latitude band in the (a) perpendicular zonal and (b) perpendicular meridional directions. The blue and red lines represent quiet time and storm time error statistics, respectively. The dashed line at 0 indicates errors that are 100% of the reference truth. As latitude increases in the low-to-mid latitude region (within ±60°), the relative error for the perpendicular-zonal and perpendicular meridional directions increases from 50% to 100% during quiet time, and 30% to 100% during storm time for perpendicular zonal direction and 5% to 100% for the perpendicular meridional direction. As hinted at in Figure 3.4, the relative errors at the boundary latitudes of ±87° are clearly off by orders of magnitude. This is likely a boundary effect of mapping latitudes to L-shell in the spherical harmonic fitting. The values at the 87-degree latitude will be removed in the subsequent plots to maintain a legible plotting scale.

The time-averaged mean error $\mu_{\epsilon vi}(\theta)$ with standard deviation $\sigma_{\epsilon vi}(\theta)$ as error bars are shown in two directions, Figure 3.5(c) field-perpendicular zonal and Figure 3.5(d) field-perpendicular meridional. Figure 3.5(c) plots zonal drift errors at two scales: for the latitude region within ±60°, the mean errors calculated for quiet time and storm time are bounded within the magnitude range of 20 m/s. For the high latitude region beyond ±60°, the mean zonal errors exceed 50 m/s. Also, the storm time variance is larger than the quiet time. These trends also hold in the perpendicular meridional direction (Figure 3.5(d)) but absolute speeds are smaller overall. While the absolute errors appear larger in Figure 3.5(c) and 3.5(d) at the northern high latitudes than the southern, Figure 3.5(a) and 3.5(b) show that the relative errors are comparable in both hemispheres.

The EMPIRE results if ϵ_{rep} is neglected are shown in Appendix B.5 inclusion of ϵ_{rep} is necessary for EMPIRE performance. From Figure 3.5 it is evident that EMPIRE corrections in the region where the magnetic latitude exceeds ±60° deviate more from SAMI3 outputs for both quiet and storm periods. For a closer examination of high latitudes, we show in Figure 3.6 the electric potential contours in the northern hemisphere in geographic coordinates, at six epochs: 8 UT, 12 UT, 16 UT on 25 August and on 26 August. Local noon is at the top of each subplot. Solid contour lines indicate EMPIRE estimates and dashed lines are SAMI3 contours. The color scale indicates kV but its span is specific to each plot. Due to the boundary latitude saturation of errors previously discussed, the contours are only plotted up to 81° geomagnetic, marked by a gray circle.

During storm periods (right column), the peak potentials of SAMI3 + Weimer and EMPIRE + Weimer are almost collocated, with slight variations in contour alignment. During the quiet time (left column) on 25 August, particularly at 8 UT and

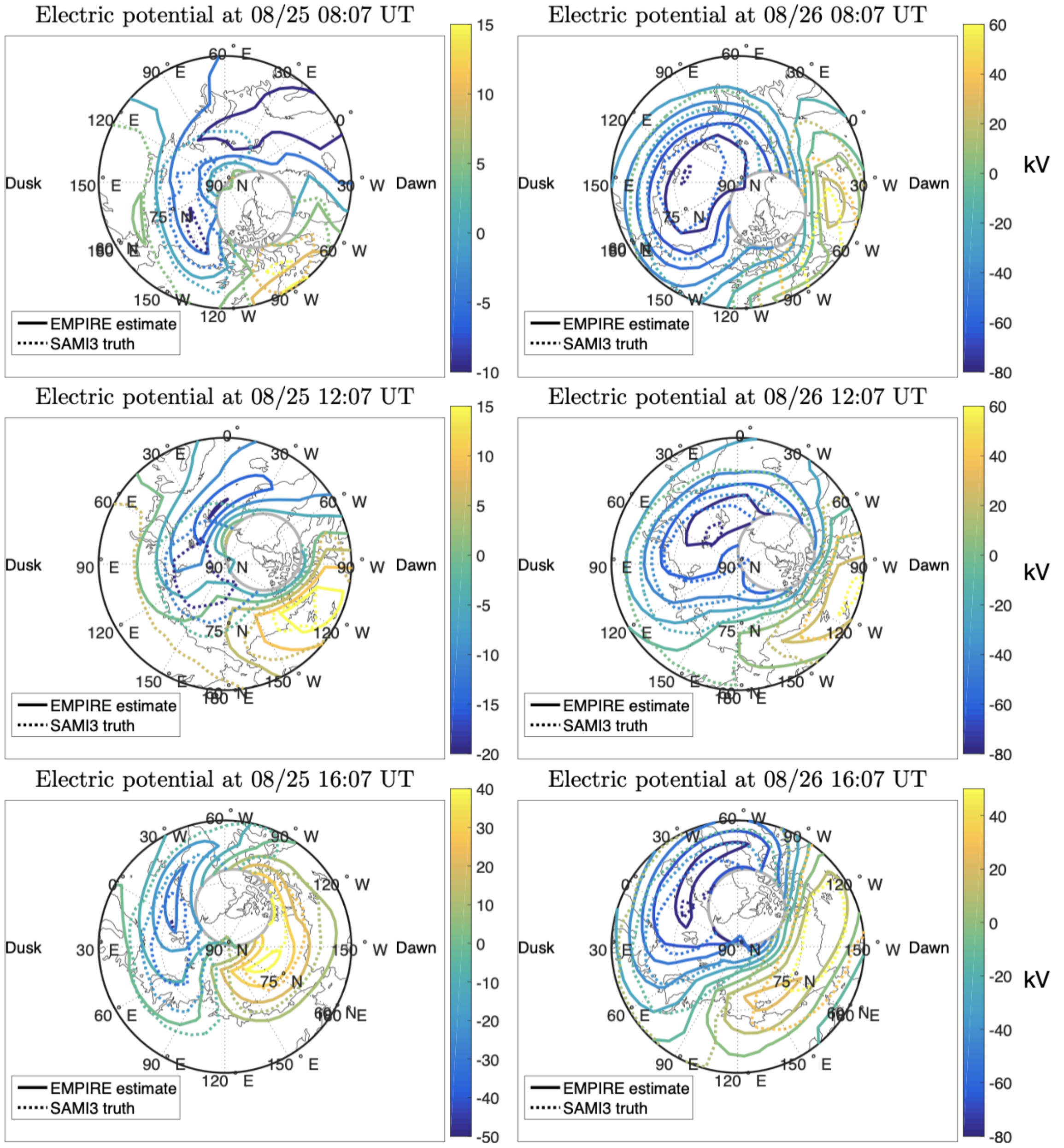

Figure 3.6. The northern hemisphere electric potential contour maps are plotted at 8 UT, 12 UT, 16 UT on August 25th (left) and 26th (right) in geographic coordinates. The EMPIRE-corrected outputs (i.e. EMPIRE + WEIMER) are plotted with solid color contours, and SAMI3 electric potentials driven by WEIMER are plotted with dashed color contours. The grey circle indicates our EMPIRE plotting limit of 81° magnetic. The dusk and dawn sides are denoted on the left and right of circle correspondingly. The colorbar indicates kilo-Volts.

12 UT, the EMPIRE corrected contour lines are noticeably displaced from SAMI3.

In both Figures 3.5 and 3.6, significant errors at high latitudes are observed in the ExB drifts and electric potential when compared to the EMPIRE corrections. A number of potential factors could influence these discrepancies in high-latitude estimations: The expansion used to estimate the potential field, described in [90], models the electric potential as constant along a dipole magnetic field line. This hypothesis becomes inaccurate around geomagnetic latitudes of $60 - 70$ degrees, when L-shell reaches values of 10 [90]. Also, the magnetic field lines at high latitudes are “open,” not represented in the dipole model. The increasing error in the EMPIRE estimations with respect to the model SAMI3 around these magnetic latitudes may be due to this hypothesis not being true in these locations. Another consideration is the grid mismatch between EMPIRE and SAMI3 at high latitudes. SAMI3 runs on the non-orthogonal field-aligned magnetic apex coordinate extending to 87 degrees of magnetic latitude [104, 105], and the outputs are transformed onto geographic coordinates with 2.5-degree resolution. Then the outputs are interpolated and ingested by EMPIRE in a uniform horizontal resolution of 6 degrees in geomagnetic coordinates. This disparity in resolutions may also contribute to larger errors observed near the magnetic poles. Another contributor might be due to the fact that [106] is the background electric potential model in EMPIRE but [95] drives SAMI3, but this is likely to be small compared to the other factors.

EMPIRE estimates the neutral wind contribution to the electron density change simultaneously with the ion drifts. Figure 3.7(a) shows the zonally averaged error of the field-parallel meridional neutral wind in comparison with the model HWM14 values, $\bar{\epsilon}_u$ from Eq. (3.7), over time. Figure 3.7(b) shows the mean error $\mu_{\epsilon u\|}$ and standard deviation $\sigma_{\epsilon u\|}$ of EMPIRE corrected field-parallel neutral wind over latitudes over quiet time (blue) and storm time (red). From Figure 3.7(a), EMPIRE

(a) Zonally averaged differences $\bar{\epsilon}_{u\|}(\theta;t)$ [EMPIRE]

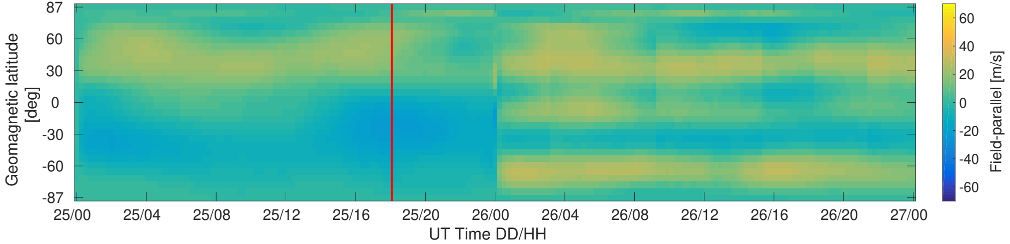

(b) Time-averaged neutral wind mean error $\mu_{\epsilon u\|}(\theta)$ and sigma $\sigma_{\epsilon u\|}(\theta)$ [EMPIRE]

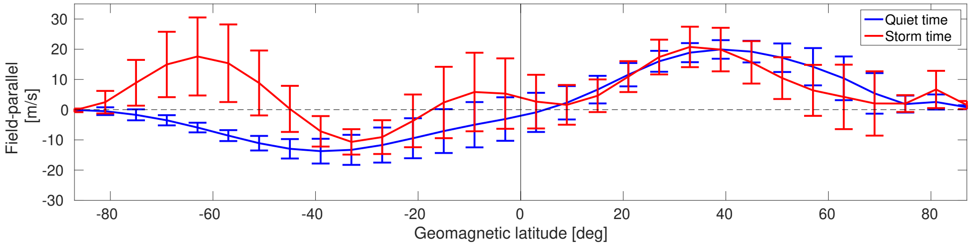

Figure 3.7. (a) Zonally averaged difference of neutral wind in the field-parallel direction from EMPIRE corrections $\bar{\epsilon}_{\mathbf{u}\|}(\theta, \mathbf{t})$ across analysis time. The red vertical line separates the quiet and storm periods. (b) Time-averaged EMPIRE field-parallel neutral wind mean errors $\mu_{\epsilon\mathbf{u}\|}$ and standard deviations $\sigma_{\epsilon\mathbf{u}\|}$ as a function of magnetic latitude.

overestimates the neutral wind in the northern hemisphere, and yields opposite results for the southern hemisphere. A hemispheric bias in the quiet time is seen in Figure 3.7(b), as the time-averaged mean error peaks are equal but opposite at ±40°. The mean error line is shaped like a sinusoidal wave, and converges to 0 approaching the magnetic poles during quiet time. The storm time-averaged neutral wind mean error yields different behaviors in the southern hemisphere compared to the quiet time.

We find the errors peaks at mid-latitudes because the measurement vector $\mathbf{z}$ fed into EMPIRE. Shown as Figure 3.8, which describes zonally averaged values at each latitude line during storm (red) and quiet time (blue) at 0808 UT, the information vector z feed into EMPIRE is more deviated from each other at Southern hemisphere, that contributes to the neutral wind driver calculations. In addition, we compare the same UT time on the quiet day and storm day: 0807 UT on August 25th and 26th.

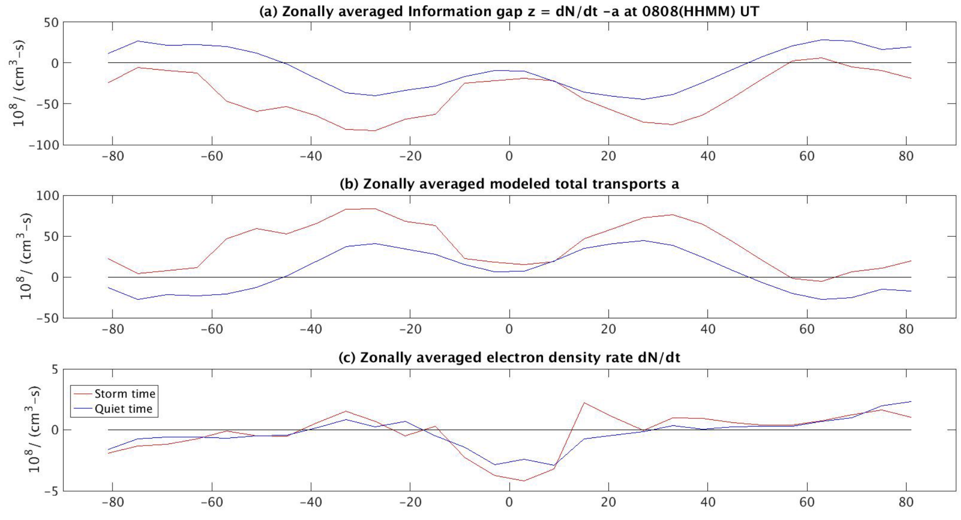

Figure 3.8. 300 KM zonally averaged (a) information gap $z = \frac{\partial N}{\partial t}$ (b) model total transports a (c) electron density rate $\frac{\partial N}{\partial t}$

A global geomagnetic map of the information gap ($\frac{\partial N}{\partial t} - a_0$) at these two times is plotted as Figure 3.9 bottom and top, respectively. A large difference between storm (top) and quiet time (below) is visible in the blue and yellow regions, as can be seen by scanning across the +50 deg latitude line in both plots.

Ion continuity is a scalar equation at each point, which means that total transport is not inherently directional decomposed. The decomposition and assumptions on motion due to the ExB drifts and neutral wind are made in our formulation of EMPIRE. Near the magnetic poles, the horizontal wind is largely perpendicular to the magnetic field-lines, thus no component from EMPIRE corrections to horizontal wind modeling is projected onto the field-parallel direction. However, in the low-to-mid latitude region, the EMPIRE calculations of neutral wind are highly impacted by the vector projection, and coordinate transformations might be contributing to the error, as EMPIRE only corrects the parallel transport in the geographic north direction. It is also possible that, because the correlation information is neglected

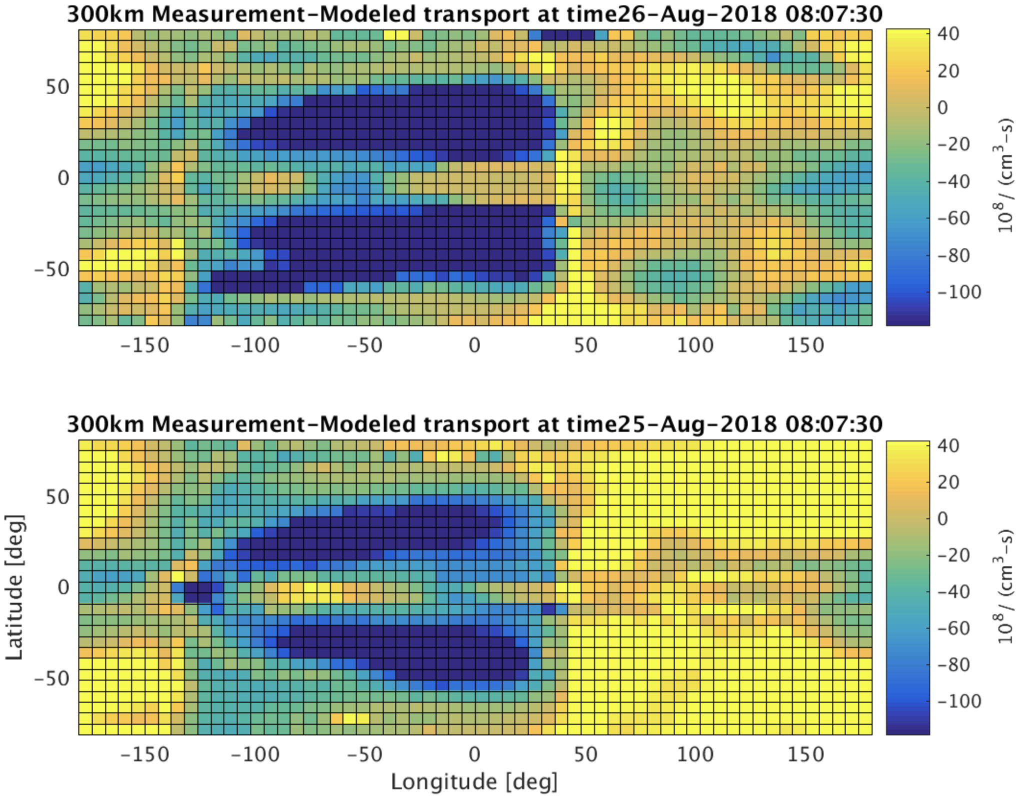

Figure 3.9. 300 KM altitude map of information gap $z = \dfrac{\partial N}{\partial t} - a_0$ on (a) August 26th 0807 UT, (b) August 25th 0807 UT.

in favor of diagonal covariance matrices in the interest of algorithmic simplicity, the Kalman filter yields biased results.

In this investigation, we analyzed the representation error for a quiet day followed by a storm day. As the Moore-Penrose inverse operator in representation error covariance calculation Eq. (3.4) is the least squares fitting process, various representation error values may be expected under different conditions. These variations can be due to factors such as solar activity levels and seasonal effects, introducing noise and changing the patterns in $\mathbf{z}$ that are then used in the fitting process. For example, the sudden change in zonally averaged differences at 00 UT August 26th in Figure 3.4 and Figure 3.7a also indicates notable daily change in estimations from day to day. This is due to the inputs to measurements and background modeled values from one day to the next. SAMI3 is driven by daily F10.7 indices, and the HWM is driven by daily F10.7 and Ap indices. Thus, the day-to-day, especially quiet-to-storm, change produces large input gaps, which leads to a sudden change in EMPIRE estimates. A comprehensive analysis of multiple periods under diverse conditions is beyond the scope of this work, but would be necessary to reveal the relationship between representation error and the other possible influencing factors.

Other limits on extrapolating conclusions from this study can be attributed to factors such as the model assumptions and simplification of physical processes. As a data assimilation algorithm based on the Kalman filter, EMPIRE is designed to analyze ionospheric drivers separately from electron density data associated with a single ion species of atomic oxygen. We also neglected spatial correlation information by diagonalizing the error covariance matrices. Furthermore, since EMPIRE correctes the geographic meridional wind, errors can arise from the Kalman filter setup representing the ion continuity equation. This is because the electron density rate is a scalar quantity and does not differentiate between the ExB effect in magnetic coordinates and the neutral wind effects in geographic coordinates.

Despite these challenges, we find the functionality of EMPIRE in calculating ion drifts and neutral winds from O^+ rate information quite promising at low-to-mid latitudes. Other assimilative methods, such as the ensemble Kalman filter or particle filter, may resolve the issue of specifying error covariance matrices in calculations but could come at the cost of reduced computational efficiency. Additionally, the state vector's length $[90 \times 1]$ for neutral wind and ion drift is not overly large for the Kalman filter to handle. Moreover, we believe that the Kalman filter's performance can be further enhanced in the future by: (1) re-scaling the error information at high latitudes compared to low-to-mid latitudes, (2) incorporating spatial correlation information between various states, and (3) revising the mapping matrices to explicitly project the transport onto field-perpendicular and field-parallel directions. These enhancements and considerations have the potential to mitigate some of the limitations found in our current approach.

3.4 Conclusion

The goal of this study was to analyze the uncertainties of the EMPIRE data assimilation method: how precise the model is in estimating the ionosphere with just the ion continuity equation from O^+, compared to a more complete ionospheric model, SAMI3. We first quantified the representation error in EMPIRE estimation of ionospheric drivers (neutral winds and ion drifts) during quiet and storm time, formulated in Section 3.1. Then EMPIRE ingested electron densities provided from SAMI3, which is the self-consistent model used for this analysis as well as the observation source and then the truth comparison.

We investigated the ionosphere behavior during 25-26 August 2018, so that all the inputs in EMPIRE were self-consistent with SAMI3. The effect of neglecting ϵ_{rep}

were shown in Appendix B.4 and show inclusion of ϵ_{rep} is needed. Latitude-dependent error statistics in response to geomagnetic activity level were shown. The ion drift estimations from EMPIRE were compared to SAMI3 ion drifts, as the estimated results were expected to be close to the modeled values. We showed that EMPIRE is able to estimate the ion drifts with smaller errors at low and mid geomagnetic latitudes. In the perpendicular-zonal direction, storm time ion drift errors are found to be limited to a magnitude of 50 m/s, while during quiet times, they remain below 25 m/s in the low-to-mid latitude region. In the perpendicular-meridional direction, both storm and quiet time ion drift errors are confined within a range of ± 10 m/s. As anticipated, it is noted that the variance of storm time errors is greater than that of quiet times. The simplification to use the ion continuity equation only is good enough at the low-to-mid latitude region, as the main component of the representation error is due to the fitting done to model the potential field with basis functions.

The field-parallel neutral wind estimation have lower errors at high and low latitudes, peaking at mid-latitudes. At the location of $\pm 40^{\circ} N$, the EMPIRE neutral wind mean error reaches the maximum magnitudes and opposite signs during quiet times. In the southern hemisphere, the time-averaged neutral wind error in the field-parallel direction during a storm exceeds that observed during quiet times. Storm-time neutral wind correction error bars are larger than quiet time in general, which implies the neutral wind during storm time is less precise than quiet time. It is due to the enhanced storm-time ionospheric variability than quiet time, leading to larger error statistics incorporated into the algorithm during storm periods.

CHAPTER 4

NEW AUGMENTATION OF SUPERDARN ION DRIFT MEASUREMENTS TO EMPIRE ALGORTIHM

During geomagnetic storms, the Earth's ionosphere-thermosphere (IT) coupled region undergoes drastic variation in its composition and dynamics. One phenomenon, the storm enhanced density (SED), is often observed in the mid-latitude and sub-auroral region on the dayside, then convects sunward and extends into higher latitudes [107]. The SED sometimes extends poleward as a tongue of ionization (TOI) across the polar cap from the day-side to night-side, and possibly into high altitudes [108]. [109] collected measurements from multiple incoherent scatter radars (ISRs), a high-latitude convection map from the Super Dual Auroral Radar Network (SuperDARN), and plasma parameters from Defense Meteorological Satellite Program (DMSP) to infer a global view of this storm-related ionospheric behavior. Supported by TEC and convection maps, [110] proposed the motion-driving mechanism for the SED to be an enhanced poleward electric field.

Because of an insufficient number of sites and measurement errors, a global map of ion drifts is challenging to obtain solely from the measurements. SuperDARN measurement-based convection maps are one example that aims to provide high-latitude convection patterns [111, 112]. Climate models are also limited in their accuracy due to the storm disturbance processes that are still not fully understood [113]. Assessment of models is ongoing [114], and prediction methods should be assessed by appropriate metrics [115].

Data assimilation (DA) approaches are used to optimally calculate the ionospheric drivers, combining model information with prior estimates of ionospheric drivers at each time epoch and updating the calculation with available measurements recursively. DA techniques can be used to optimize the calculations by ingesting both information from models and measurements. The traditional branches of DA algorithm include variational, sequential or hybrids methods [116]. For each analysis time epoch, the variational (4D-Var) DA algorithm requires linearized observation and forecast operators, as well as pre-defined Gaussian uncertainty statistics for the models and observation, then yields the optimized state from minimizing the cost function. The sequential DA algorithm, based on Bayes' theorem, yields the optimized state calculations based on the optimized gain calculations using the defined error statistics. The sub-branhes of sequential DA algorithm include the conventional Kalman filter, Ensemble filter, and Monte-Carlo method (i.e. particle filer).

One solution to the challenge of predicting storm-time IT behavior has been to leverage measurements that *are* plentiful, i.e., GNSS TEC. Over the past two solar cycles, multi-frequency GNSS measurements have grown to form the backbone of ionospheric TEC imaging. The plentiful nature of these measurements has changed our view of the ionosphere from a single point of sensing to a global view of plasma, continuously changing over time. The IDA4D is a variational method that solves for the log of electron density from satellite and ground-based measurements [26, 117]. Another variational DA algorithm that has been developed is the Global Assimilative Ionospheric Model (GAIM) developed by the University of Southern California and Jet Propulsion Laboratory (USC/JPL) [118, 119, 120]. GAIM-USC/JPL uses a physics-based model derived from the University of Sheffield model, which solves the ion continuity and momentum equations for one ion species O^+ [121]. This algorithm decomposes the ion motions into the field-parallel and field-perpendicular components and solves the O^+ density. Coupling with the band-limited Kalman filter and 4DVAR technique, it ingests the line-of-sight TEC data by the GPS occultation receivers on board six FORMOSAT-3/COSMIC satellites and two hundred GPS ground receivers, the equatorial ExB velocity estimation was improved with validating the

ISR measurements at Jicamarca Radio Observatory [122, 123].

The Global Assimilation of Ionospheric Measurements Full Physics (GAIM-FP) is an ensemble-based DA developed by the Utah State University (USU), initially coupled with the reduced state Kalman filter then altered to the ensemble technique [124, 125]. It is updated to assimilate in-situ measurements from DMSP satellites, occulatation data from the six COSMIC satellites, GPS TEC from ground-based receivers, and electron density profiles from ionosondes, enables the calculations of neutral wind and electric fields at low-to-mid latitudes [126]. The ionospheric dynamics and electrodynamics-data assimilation (IDED-DA) model is also an ensemble-based DA algorithm, that assimilates the magnetic field differences measured by 92 ground magnetometers, cross-track drift velocities from DMSP satellites and LOS velocities from nine SuperDARN radars, to analyze the ionosphere and electrodynamics parameters [127, 128].

The ability to observe IT density changes also allows us to investigate what causes the changes in plasma density over time. Neutral winds are an important driver of ionospheric plasma through collisional and drag effects. As mentioned before, electric fields are also important, particularly at high and low magnetic latitudes, where they give rise to significant plasma “E cross B” drifting in a direction that is perpendicular to both Earth’s magnetic field and any electric field present. Together, these are significant contributors to storm-time global plasma redistribution in the ionosphere.

If and when ion drift measurements are available, they indicate the presence of electric fields perpendicular to the magnetic field. AMIE develops a high-latitude convection pattern by ingesting SuperDARN measurements, magnetometer stations, and DMSP satellites [129, 130, 131]. AMGeO is in the process of integrating geospatial data with ground-based measurements which includes SuperDARN line-of-sight ion velocities [132].

This work presents a sequential DA algorithm that directly ingests the ion velocity measurements by ground-based instruments to investigate the ionospheric drivers. EMPIRE is a variational DA algorithm we have developed [36] focused on estimating the drivers of neutral wind and electric potential explicitly in a global or regional setup, primarily via the ion continuity equation of O^+. It primarily ingests the IDA4D-estimated electron density rates and outputs corrections to neutral winds relative to a background model and corrections to electric potential that give rise to ExB drifts. EMPIRE algorithm was then modified to ingest neutral wind measurements from Fabry-Perot Interferometers (FPI) at multiple locations, to improve the driver calculations [42]. Spherical harmonics for electric potential were derived and used for global correction electric fields [37]. It was noted that errors increases pole-ward of 60^o [4]. [39] developed a vector spherical harmonic expansion to globally map the neutral winds. By also assimilating drift measurements into EMPIRE, we will have a more direct measurement of the quantity of interest (the electric field), although fewer of them than plasma density since radars are more sparsely distributed globally than GNSS receivers.

Our objective in this work is to assimilate ion drift measurements from SuperDARN sites for estimating the ionospheric physical drivers, and to study the importance of data pre-processing to smooth out data noise. The storm event on March 17th 2015 is selected, for which strong westward zonal drifts were measured with the Millstone Hill Incoherent Scatter Radar (ISR) [133]. We investigate the effect of EMPIRE implementations augmenting ion drift measurements, and compare the results with the baseline configuration of ingesting electron density rates for this storm event. The IDA4D algorithm, using background model SAMI3, provides the electron density rates as the majority of the measurements assimilated.

The new mapping matrix for ingesting the SuperDARN measurements is derived in Section 4.1. Section 4.2 describes the methodology for assessing the impact of drift assimilation into EMPIRE, along with the experimental configurations of data inputs and error covariance. The results comparing ion drifts calculated from three experimental setups, and from the SAMI3 background model are presented in Section 4.3. Discussion in Section 4.4 interprets EMPIRE's capabilities of computing the ionospheric drivers globally.

4.1 Ingestion of line-of-sight ion drifts

During storm time, ionospheric velocities obtained from background models may not accurately describe plasma motion. The EMPIRE algorithm was developed to reduce the gap between background models and measured ion velocities, enabling a more accurate perspective on plasma behavior. In previous work, the EMPIRE algorithm ingested 630.0 nm Fabry–Perot interferometer (FPI) neutral wind observations and showed the improvement in the estimation of neutral winds [42]. By analogy, in this work we test whether the estimate of electric potential giving rise to ion drifts can be significantly improved by assimilating the difference between SuperDARN coherent scattering radar measurements of ion velocity from background model drift values directly into EMPIRE. By extending the application of the Kalman filter in EMPIRE, the gap ion velocities $\mathbf{z_{vel}}$ are stacked with the plasma density rates $\mathbf{z_{\partial N/\partial t}}$, potentially enabling better specification of the ionospheric electric field. The augmented linear system is expressed as:

$$\underbrace{\begin{bmatrix} \mathbf{z_{\partial N/\partial t}} \\ \mathbf{z_{vel}} \end{bmatrix}}_{\mathbf{z}} = \underbrace{\begin{bmatrix} \mathbf{H_V} & \mathbf{H_u} \\ \mathbf{H_{vel}} & \mathbf{0} \end{bmatrix}}_{\mathbf{H}} \underbrace{\begin{bmatrix} \delta\mathbf{x_V} \\ \delta\mathbf{x_u} \end{bmatrix}}_{\delta\mathbf{x}} + \underbrace{\begin{bmatrix} \varepsilon \\ \varepsilon_{\mathbf{vel}} \end{bmatrix}}_{\epsilon} \tag{4.1}$$

where $\mathbf{0}$ is a block matrix of zeros in the coefficient matrix. The augmented linear system is then used to estimate $\delta\mathbf{x}$ via Kalman filter of Eq. (2.26).

Section 2.3.3 defined $\delta\mathbf{x}_V$ in Eq. (2.33) and $\delta\vec{v}_\perp$ in Eq. (2.34) for this new study in which we augment the EMPIRE observation array with direct measurements of ion velocity. In Eq. (4.1), the observation $\mathbf{z_{vel}}$ is a subarray of length j of measurement-model differences of ion velocity, made within estimation time interval dt stacked with the subarray $\mathbf{z_{\partial N/\partial t}}$. The matrix $\mathbf{H_{vel}}$ maps the coefficients $\delta\mathbf{x_V}$ for the correction potential δV in Eq. (2.31) that yields the ExB ion drift onto the observation space. The observation locations do not have to coincide with the grid points used in the EMPIRE continuity equation. The measurements from SuperDARN in $\mathbf{z_{vel}}$ will depend on the data product projection used, for which we compute the azimuth angles and magnitudes of the LOS ion velocities for formulating the mapping matrix $\mathbf{H_{vel}}$. The measurement noise is $\varepsilon_{\mathbf{vel}}$ from the instrument data providers of the ion drift.

Because there are two levels of data product—the raw fits to auto-correlation function, named "fit" data, and the gridded data of fits after outlier removal "grid"—the mapping matrix $\mathbf{H_{vel}}$ will differ slightly. The ion velocities from the fit data sets provide geographic locations, from which we must compute the geographic bearing angle between the line-of-sight direction and geographic north. Then the velocity components in EMPIRE geomagnetic coordinates are calculated from the coordinate transformations. The geomagnetic bearing angles are provided directly in the gridded data.

In the rest of this section, we define $\mathbf{H_{vel}}$ for the two data product types, by projecting the vector ExB drift difference $\delta\vec{v}_\perp$ onto the velocity measurement for each element of $\mathbf{z_{vel}}$. With coherent scatter radar, the measured line-of-sight (LOS) velocity vector lies entirely in the field-perpendicular plane. Figure 4.1(a) shows the measured ion velocity $\vec{v}_l$ (positive for motion away from the radar) as perpendicular

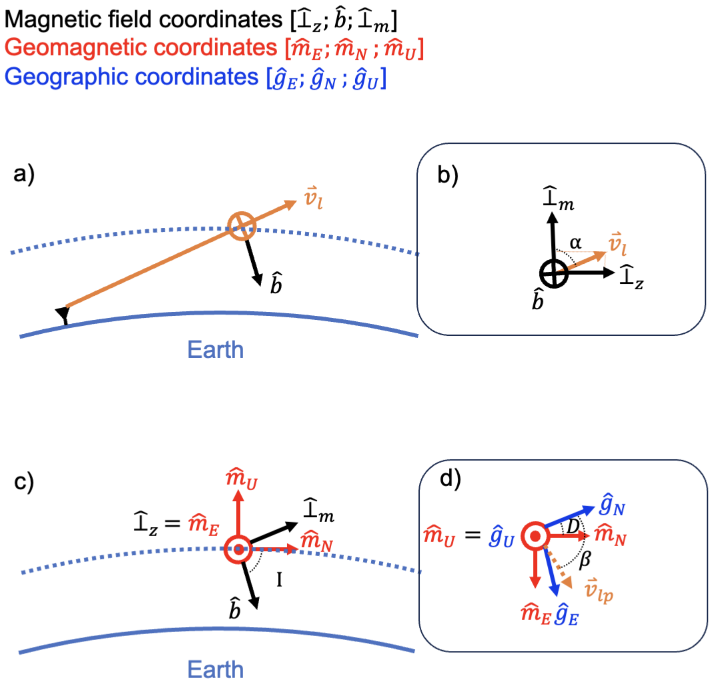

Figure 4.1. (a) A 2D view of one SuperDARN line-of-sight (LOS) ion drift vector measurement $\vec{v}_l$, indicating it is perpendicular to the field-aligned direction ($\hat{b}$ in black).(b) A 2D view showing $\vec{v}_l$ decomposition in the field-perpendicular zonal ($\hat{\perp}_z$ in black) and field-perpendicular meridional ($\hat{\perp}_m$ in black) frame, with $\hat{b}$ pointing into the page. The bearing angle between $\vec{v}_l$ and $\hat{\perp}_m$ is denoted as α. (c) A 2D view of coordinate transformation between field and geomagnetic coordinates and the sharing axes are $\hat{\perp}_z$ and geomagnetic east ($\hat{m}_E$ in red) is out of page. The geomagnetic north and up directions are denoted by $\hat{m}_N$ and $\hat{m}_U$ in red respectively. I is the inclination angle between $\hat{m}_N$ and $\hat{b}$. (d) A 2D view of $\vec{v}_l$ projection on the magnetic east-north plane, denoted as $\vec{v}_{lp}$. It also shows the rotation from geomagnetic coordinates to geographic coordinates. The geographic East-North-Up are denoted as $\hat{g}_E$, $\hat{g}_N$ and $\hat{g}_U$, correspondingly. The declination angle between $\hat{g}_N$ and $\hat{m}_N$ is D, and β is the bearing angle between $\vec{v}_{lp}$ and $\hat{g}_N$.

to $\hat{b}$. The magnetic field aligned direction is $\hat{b}$ drawn in black, the LOS vector is denoted as $\vec{v}_l$ in orange.

Figure 4.1(b) shows the decomposition of $\vec{v}_l$ onto field-perpendicular zonal and meridional directions, denoted as $\hat{\perp}_z$ and $\hat{\perp}_m$ in black, respectively. The bearing angle α is between $\hat{\perp}_m$ and $\vec{v}_l$. Figure 4.1(c) shows the coordinate transformations between field and geomagnetic coordinates. The geomagnetic East-North-Up directions are denoted as $\hat{m}_E$, $\hat{m}_N$ and $\hat{m}_U$, respectively, in red. The unit vector ($\hat{\perp}_z = \hat{m}_E$) is pointing out of page, and the inclination angle is I. Figure 4.1(d) represents the projection of $\vec{v}_l$ onto the geographic east-north plane, denoted as $\vec{v}_{lp}$ in orange. The declination angle D is defined by the rotation about the $\mathbf{\hat{m}_U}$ axis that gives geographic ENU coordinates $\mathbf{\hat{g}_E}$,$\mathbf{\hat{g}_N}$,$\mathbf{\hat{g}_U}$ (in blue). The angle between $\vec{v}_{lp}$ and $\hat{g}_N$ is marked as β. The relationship between $\vec{v}_l$ and $\vec{v}_{lp}$ is derived in Appendix C.1.

For the raw fit data, the line-of-sight velocity $\vec{v}_l$ in the field-perpendicular plane and the geographic location of the measurement are provided, but angles must be computed to obtain the projection of the state onto the line-of-sight. The angle β is estimated by computing the angle between geographic north $\mathbf{\hat{g}_N}$ and the projected velocity component v_{lp} on the horizontal plane. The angle α between the perpendicular meridional direction $\hat{\perp}_{\mathbf{merid}}$ and the radar measurement direction is in Equation (4.2), derived in Appendix C.1:

$$\alpha = \arctan(\tan(\beta - D)\sin I) \tag{4.2}$$

The observation z_{vel_fit} at one point is the difference between the line-of-sight measurement v_l and the modeled value of that line-of-sight speed v_{l0}. The observation

z_{vel} is mapped from the state $\delta\mathbf{x_V}$ as:

$$z_{vel\_fit} = \|\vec{v}_l - \vec{v}_{l0}\| = \underbrace{\begin{bmatrix}\sin\alpha & 0 & \cos\alpha\end{bmatrix} {}^{\mathbf{field}}\mathrm{R}^{\mathbf{gm}}\,{}^{\mathbf{gm}}\mathrm{R}^{\mathbf{sph}} \begin{bmatrix}\mathbf{H}_{\perp\mathbf{r}} \\ \mathbf{H}_{\perp\theta} \\ \mathbf{H}_{\perp\phi}\end{bmatrix}}_{\mathbf{H_{vel\_fit}}} \begin{bmatrix}\delta\mathbf{x_V}\end{bmatrix}$$

The rotation matrices ${}^{\mathbf{field}}\mathbf{R}^{\mathbf{gm}}$ and ${}^{\mathbf{gm}}\mathrm{R}^{\mathbf{sph}}$ are defined in Appendix C.1. Stacking the observations $z_{vel_{fit}}$ into a column matrix gives $\mathbf{z_{vel}}$ for the fit data to be used in Eq. (4.1). Stacking the row matrix in the brace for each observation gives the mapping matrix $\mathbf{H_{vel}}$ for fit data.

In the SuperDARN grid data, the magnitude of $\vec{v}_{lp}$ in the geographic east and north plane is provided from the files. The observation $z_{vel_{grid}}$ is the difference between the median velocity measured v_{lp} and the background model value at that location v_{lp0}. When the grid data are used, the observation is mapped from the state $\delta\mathbf{x_V}$ as follows, to give a row matrix $\mathbf{H_{vel}}$ for one observation:

$$z_{vel\_grid} = \|\vec{v}_{lp} - \vec{v}_{lp0}\| = \underbrace{\begin{bmatrix}\sin\beta & \cos\beta & 0\end{bmatrix} {}^{\mathbf{g}}\mathrm{R}^{\mathbf{gm}}\,{}^{\mathbf{gm}}\mathrm{R}^{\mathbf{sph}} \begin{bmatrix}\mathbf{H}_{\perp\mathbf{r}} \\ \mathbf{H}_{\perp\theta} \\ \mathbf{H}_{\perp\phi}\end{bmatrix}}_{\mathbf{H_{vel\_grid}}} \begin{bmatrix}\delta\mathbf{x_V}\end{bmatrix} \tag{4.3}$$

The observations z_{vel_grid} are stacked to form $\mathbf{z_{vel}}$ used in Eq. (4.1). Similarly, the row matrix bracketed in Eq. (4.3) is stacked for every observation made during the time window dt to form $\mathbf{H_{vel}}$ for grid data.

4.2 Experimental Method

To test the methodology of ingesting velocity measurements, the geomagnetic storm event on 17 March 2015 is investigated via EMPIRE with three scenarios: (1) ingesting the electron density rates only, (2) augmenting the rates with northern hemisphere fit line-of-sight ion velocities provided by SuperDARN, (3) augmenting the rates with northern hemisphere gridded ion velocities provided by SuperDARN smoothed data products, as shown in Figure 4.2.

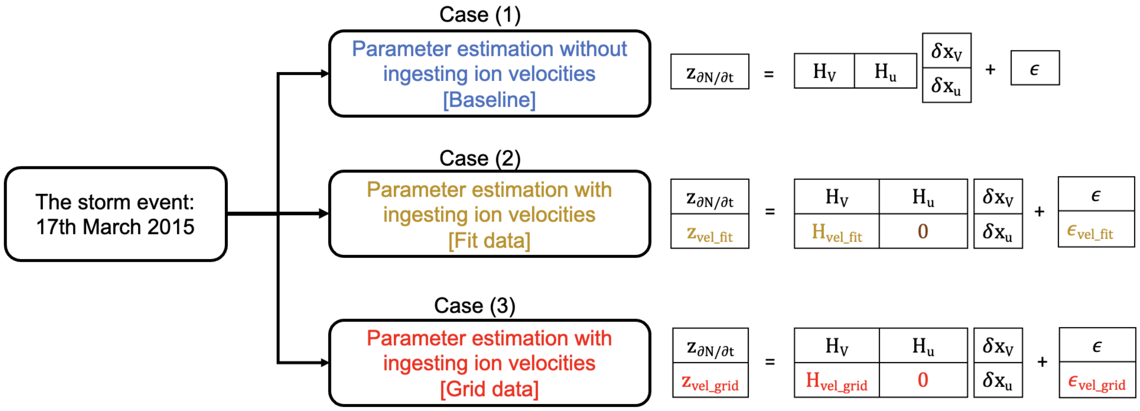

Figure 4.2. Summary of linear system for three EMPIRE run configurations for the March 2015 storm. Case (1) (blue) does not ingest ion velocity measurements, using only plasma density rates. Case (2) (gold) augments the density rate observations with SuperDARN fit velocities. Case (3) (red) is estimation augmenting density rates with gridded SuperDARN velocities. The same colors will be used for result plots.

To provide context for the analysis window for EMPIRE runs, the Disturbance storm time (Dst) index is shown in Figure 4.3 from 00 UT on March 16th to 00 UT on March 19th. The main phase time range of the storm is approximately from 06 UT to 23 UT on March 17th. The time prior to 06 UT on the 17th is pre-storm, and the window after 23 UT on the 17th is the recovery phase. The analysis interval spans from 00 UT on the 16th to 24 UT on the 18th. The order $l = 6$ is selected for spherical harmonic and vector spherical harmonic fitting function for electric potential and neutral wind correction drivers.

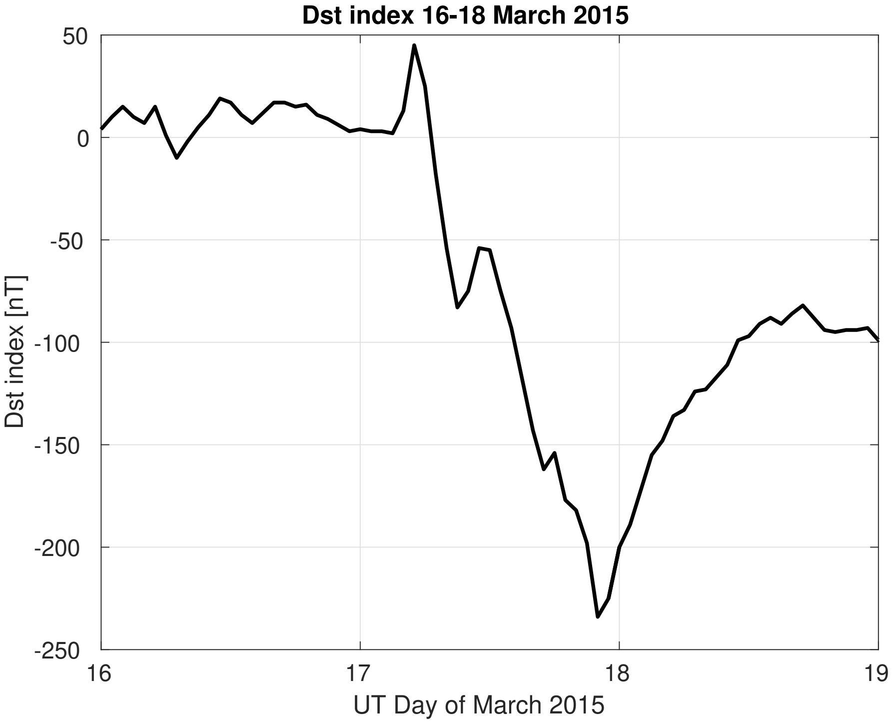

Figure 4.3. The Dst index in nanoTesla (nT) from 16-18 March 2015. The quiet period is March 16th until 06 UT on March 17th. The main phase is from 06 UT to 23 UT on the 17th, followed by the recovery phase.

The assessment procedure is summarized in Figure 4.4. The electrical potential correction drivers $\delta\mathbf{x_V}$ and neutral wind drivers $\delta\mathbf{x_u}$ calculated from these three setups are mapped to the observation space. The goal is to compare the ExB drifts accuracy improvement from the three EMPIRE configurations to the derived velocity vectors provided by Millstone Hill and two superDARN data sets at sites labeled in Figure 4.5 as validation sites and investigate the influence of the SuperDARN data pre-processing on EMPIRE ingestion of ion velocities.

4.2.1 Data inputs and EMPIRE 4D grid configuration. The EMPIRE algorithm primarily ingests global electron density rates for the evaluation time window. Electron densities are obtained from IDA4D [26], an assimilative estimation coupled to SAMI3 [32], which is a physics-based background model of the ionosphere. IDA4D

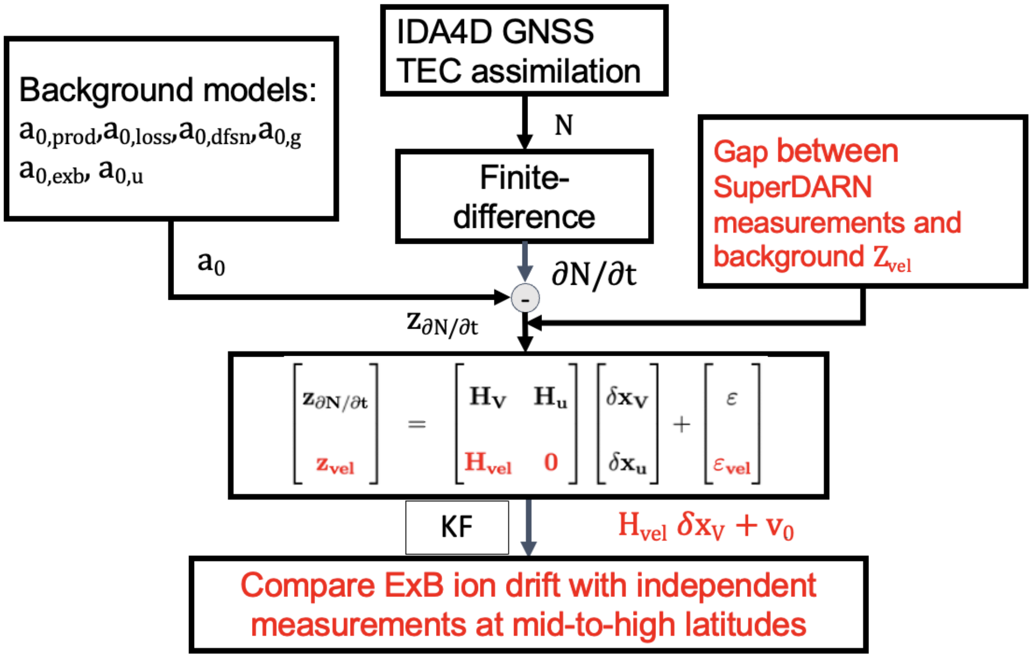

Figure 4.4. The flowchart of the EMPIRE setup and experimental procedure for assessing the improvements. The red text indicates the validation process of augmenting the LOS ion velocity measurements to the algorithm. KF stands for Kalman filter.

outputs are provided at 1° x 4° for horizontal resolution (latitude x longitude), and the time step of 15 minutes. The vertical resolution is 10 $[km]$ for the altitude range from 200 $[km]$ to 380 $[km]$, and 20 $[km]$ for the range from 380 $[km]$ to 500 $[km]$. The electron densities are time-differenced and then projected onto the EMPIRE spatial map. This process generates a measurement vector of dimensions [8650x1] for data assimilation at each time epoch, across a total of 288 time steps. Figure 4.5 plots examples of the SAMI3/IDA4D TEC integrated from the densities from 16 UT on March 17th to 04 UT on March 18th.

For the case of augmenting ion velocity measurements, we selected the SuperDARN sites located at the mid-to-high latitude range of the northern hemisphere. Figure 4.6 is an example plot of ingested SuperDARN fit data coverage within a 5-min interval at 00 UT on March 17th. Table 4.1 is a list of radar sites whose the data

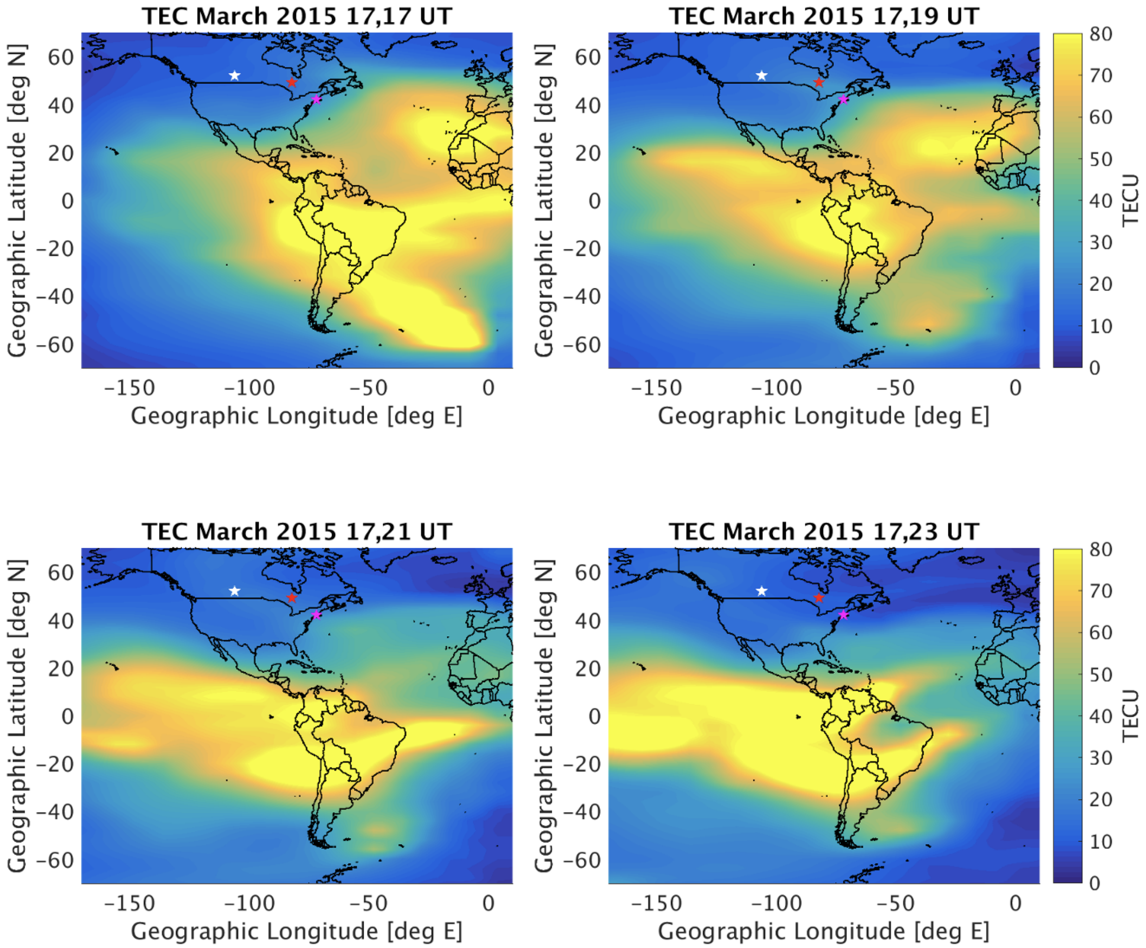

Figure 4.5. VTEC plot in TEC units (TECU), where 1 TECU $= 10^{16}[el/m^2]$. Top row: 17 UT, 19 UT on March 17th, 2015. Bottom row: 21 UT, 23 UT on March 17th, 2015. The magenta star is the Millstone Hill incoherent scatter radar location (41° N, 72° W). The SuperDARN Saskatoon (52° N, 106° W) and Kapuskasing (49° N, 82° W) radar sites are denoted by white and red stars, respectively.

are ingested into the algorithm. During the entire analysis interval, spanning from 00 UT on March 16th to 24 UT on March 18th, EMPIRE is supplied with a total of 100,713 data values for EMPIRE case (2) with fit data ingestion, and 2,271,532 data values for case (3) with gridded data ingestion.

For the background terms ingested to the EMPIRE algorithm, the production and loss rate terms are produced based on the Kirchengast model [134]. The Naval Research Laboratory mass spectrometer incoherent scatter model (NRL-MSISE-00)

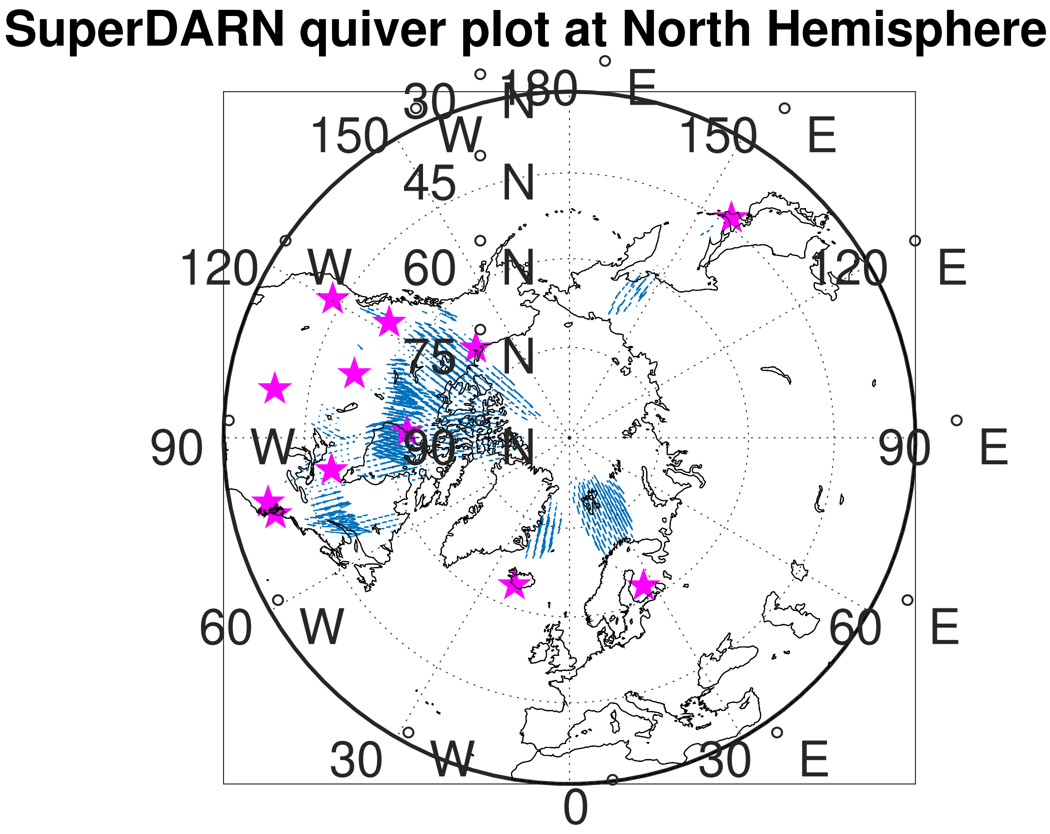

Figure 4.6. Quiver plot of SuperDARN data line-of-sight ion velocities during a 5-min time window at around 00 UT on March 17th ingested by EMPIRE. The magenta stars are the locations of the radar sites.

Table 4.1. List of SuperDARN radar site locations and magnetic latitudes whose data are ingested to the EMPIRE algorithm. The kap and sas sites with highlighted in red are used for validation and are not into EMPIRE.

Site name	Location	Mag lat	Site name	Location	Mag lat
bks	$37^{\circ}N$, $78^{\circ}W$	$46^{\circ}N$	cly	$70^{\circ}N$, $69^{\circ}W$	$80^{\circ}N$
fhw	$39^{\circ}N$, $100^{\circ}W$	$47^{\circ}N$	han	$62^{\circ}N$, $27^{\circ}E$	$59^{\circ}N$
hok	$44^{\circ}N$, $144^{\circ}W$	$46^{\circ}N$	inv	$68^{\circ}N$, $134^{\circ}W$	$71^{\circ}N$
cve/cvw	$43^{\circ}N$, $120^{\circ}W$	$49^{\circ}N$	pgr	$54^{\circ}N$, $123^{\circ}W$	$59^{\circ}N$
pyk	$64^{\circ}N$, $21^{\circ}W$	$69^{\circ}N$	rkn	$63^{\circ}N$, $92^{\circ}W$	$72^{\circ}N$
wal	$38^{\circ}N$, $76^{\circ}W$	$48^{\circ}N$			
kap	$50^{\circ}N$, $82^{\circ}W$	$60^{\circ}N$	sas	$52^{\circ}N$, $106^{\circ}W$	$60^{\circ}N$

provide the neutral densities and temperatures [135]. The electron and ion temperatures come from the SAMI3 model [32]. SAMI3 coupled with Weimer model [136], serves as the background model for electric potential driver. The neutral wind is computed by the HWM14 [137]. The magnetic field is calculated from the IGRF-11 model [40]. The background model quantities and density rate measurements are ingested in the EMPIRE algorithm with a 4D global grid map in geomagnetic coordinates. The longitude ranges from -180 ° to 180 °, and co-latitude is set from 3° to 177°, with 6° spacing for both. The height range is 200 to 500 kilometers, and 50 km as step size. The analysis time epoch is 15 minutes.

4.2.2 Measurement error covariance. In the Kalman filter, it is essential to construct the model-update and measurement-update error. The derivation of model covariance matrix $\mathbf{P_0}$ is described in Appendix B of [4]. The measurement error covariance $\mathbf{R}$ can be considered in two categories: measurement error covariance $\mathbf{R_{msmt}}$ and representation error covariance $\mathbf{R_{rep}}$. The representation errors are due to unresolved state, observation operator, and pre-processing procedures [138]. The mathematical notation is defined as:

$$\mathbf{R} = \mathbf{R_{msmt}} + \mathbf{R_{rep}}$$

We numerically compute the representation error $\epsilon_{\mathbf{rep}}$ [4] as the difference between numerical “truth” vector $\mathbf{z}$, and the representation error is normally distributed with representation error covariance $\mathbf{R_{rep}}$.

At each time epoch k, the measurement error covariance $\mathbf{R_{msmt}}$ is mathematically represented by the block matrices in small brackets:

$$\mathbf{R_{msmt}} = \begin{bmatrix} [\sigma^2_{\mathbf{\partial N/\partial t}} + \sigma^2_{\mathbf{a_0}}] \\ \\ [\sigma^2_{\mathbf{vel}} + \sigma^2_{\mathbf{vel,0}}] \end{bmatrix} \tag{4.4}$$

Assuming the error sources are linearly independent with Gaussian distribution, the $\sigma_{\partial N/\partial t}$ for each j^{th} point is the partial time derivative of the sum of $50\%N$ plus $10^{10}[el/m^3]$ as a base value to ensure the error bar is reasonable for small electron density values [118]:

$$\sigma_{\partial N/\partial t} = \frac{\partial(50\%N + 10^{10})}{\partial t}$$

The uncertainty σ_{vel} is the standard deviation of measured values by SuperDARN, plus 20% of the measured line-of-sight velocity vel, to account for the effects of the unresolved state and observation operator. The model uncertainties σ_{a0} and $\sigma_{vel,0}$ in Eq. (4.4) are assumed to be 20% of the modeled value a_0 and vel_0, respectively.

$$\sigma_{a0} = 20\%a_0$$

$$\sigma_{vel,0} = 20\%v_0$$

where $v_0 = v_{l0}$ for SuperDARN fit data ingestion, $v_0 = v_{lp0}$ for SuperDARN grid data ingestion.

4.3 Results

Figure 4.7 shows the results comparing the SAMI3 modeled ExB drifts (magenta), EMPIRE implementation of ingesting the IDA4D/SAMI3 electron density rates only (blue), and the new EMPIRE augmentation of case(2) (gold) and (3) (red) with the MHISR-derived ion velocity vectors (black) that are provided in the field-perpendicular (a) zonal and (b) meridional directions.

MHISR measures small zonal drifts until about 1900 UT on March 17th, turning more strongly westward until reaching 1000 m/s westward at 2130 UT. The westward drift then weakens through 2300 UT. The zonal drifts calculated from case (2) appear to be closest to the MHISR data. After 19 UT, the case (2) ingestion is slightly less westward than the SAMI3 model, which indicates the presence of equator-ward electric field in EMPIRE. Both the baseline case (blue) and case of ingesting grid (red) SuperDARN data yield estimates further from the actual MHISR zonal drift measurements until 0500 UT on March 18th.

In Figure 4.7(b), the MHISR measurements (black) indicate positive drifts, which are along $\hat{\perp}_{merid}$, meaning magnetically northward and upward. The meridional drift peaks at almost 1100 m/s at 2000 UT, and maintain high speed until 2200 UT. EMPIRE cases (1) and (3) yield similar results of decreasing to negative velocity in the field-perpendicular meridional direction at 1530 UT, which are the furthest from MHISR measurements. EMPIRE case of ingesting fit superDARN data yield larger meridional drifts than SAMI3 from 1500 UT to 1800 UT on March 17th, then both case (2) and SAMI3 merge with EMPIRE case (1) and (3) starting from 2100 UT. After 2200 UT, MHISR meridional drift decreased and turns to be negative, which is geomagnetic downward and equatorward.

Table 4.2 summarizes the mean error and residual sigma of the error from each estimation result and of SAMI3 compared to the ISR measurements for the field-perpendicular meridional and zonal directions. The lowest mean error in each direction is listed in bold. Based on the mean error comparisons, the SAMI3 model gives the best estimate in the zonal direction as the value is -168 m/s, and EMPIRE case (2) yields the lowest value of -229 m/s in the meridional direction. The lowest standard deviation in each direction is listed in bold and corresponds to the run with

(a) Field-perp zonal ion drifts at 47 °N 89 °W

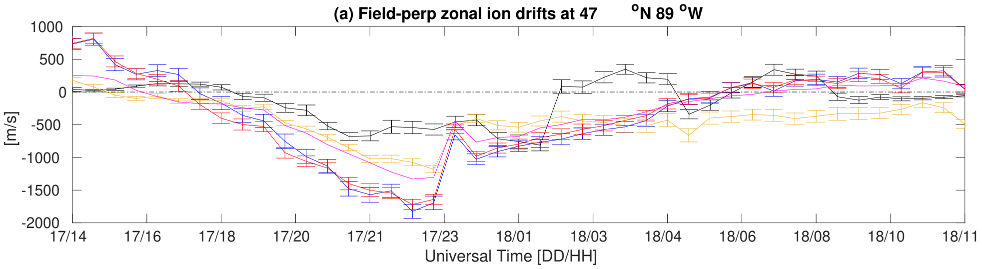

(b) Field-perp meridional ion drifts at 53 °N 75 °W

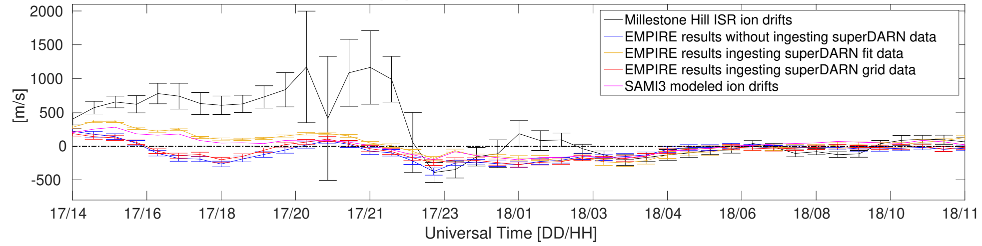

Figure 4.7. ExB drifts estimations from SAMI3 model (magenta), EMPIRE primary setup (blue), and new augmentation of ingesting SuperDARN gridded (red) or fit data (gold). They are compared with the MHISR-derived velocity components (black curves) in the field-perpendicular zonal and meridional directions. The black dashed line is the zero velocity line. The field-perpendicular zonal and meridional ion drift calculations are compared to MHISR measurements at geodetic locations of $47°N89°W$ and $53°N75°W$, and geomagnetic locations are $56°N20°W$ and $62°N3°W$

(a) Line of sight ion velocity validation with SuperDARN kap site at Geographic 50 ° N 82 ° W

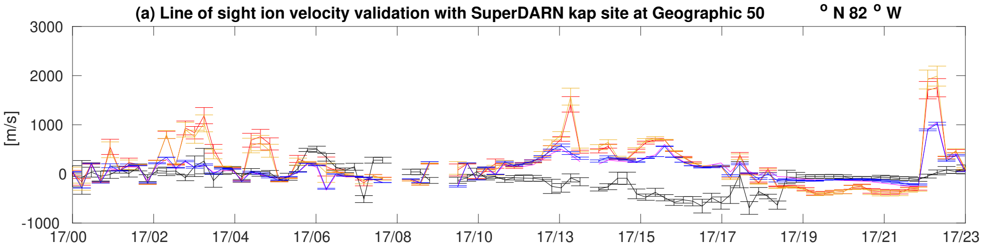

(b) Line of sight ion velocity validation with SuperDARN sas site at Geographic 52 ° N 106 ° W

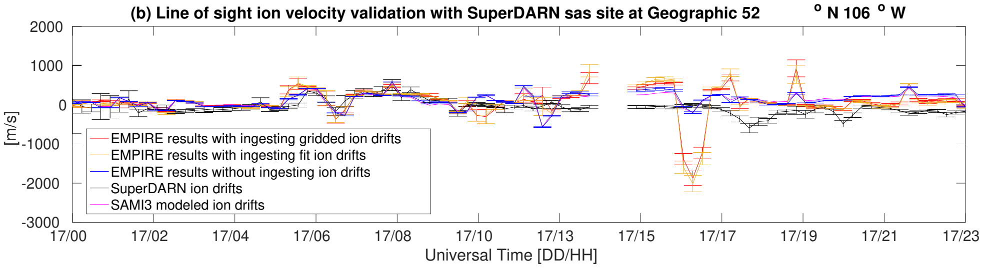

Figure 4.8. ExB drifts estimations from SAMI3 model (magenta), EMPIRE case (1) (blue), and new augmentation of case (3) ingesting SuperDARN gridded (red) or case (2) fit data (gold). They are compared with the line-of-sight superDARN velocity (black curves) at Kapuskasing (kap) and Saskatoon (sas) sites. The geodetic locations are $50°N82°W$ and $52°N106°W$ for Kap and Sas sites respectively, and the geomagnetic locations are $60°N12°W$ and $60°N42°W$.

the lowest mean error. Based on the standard deviation comparison in the zonal direction, EMPIRE case (2) gives the lowest uncertainty in the zonal and meridional directions as the sigma values are 276 m/s and 342 m/s respectively. The EMPIRE calculation performs worse than the model estimation, for the case of only ingesting IDA4D/SAMI3 electron density rates and the case of augmenting SuperDARN gridded ion drift measurements. When comparing the EMPIRE outputs from different setups, the residual sigma value for augmenting fit SuperDARN data is approximately 44% lower than the baseline setup in the zonal direction and 18% lower in the meridional direction. Conversely, augmenting grid SuperDARN data only shows 4% reduction compared to the baseline setup in both the zonal and meridional directions.

We also compared the EMPIRE cases and SAMI3 model with SuperDARN

Table 4.2. Mean error and residual sigma table of validation results for comparing the ExB drift calculations from different cases and the MHISR derived ion velocity vector. The bold text indicates the lowest magnitudes in a given direction.

Case	Zonal mean error [m/s]	Meridional mean error [m/s]	Zonal residual sigma [m/s]	Meridional residual sigma [m/s]
SAMI3 model	**-168**	-239	315	379
EMPIRE without ingesting ion drifts	-205	-328	507	418
EMPIRE ingesting fit ion drifts	-284	**-226**	**276**	**342**
EMPIRE ingesting grid ion drifts	-213	-316	488	403

Table 4.3. Mean error and residual sigma table of validation results for comparing the ExB drift calculations from different cases and the superDARN grid ion velocity. The bold text indicates the lowest magnitudes in a given direction.

	KAP site		SAS site	
Case	Mean error [m/s]	Residual sigma [m/s]	Mean error [m/s]	Residual Sigma [m/s]
SAMI3 model	**172**	360	159	227
EMPIRE without ingesting ion drifts	193	464	**89**	281
EMPIRE ingesting fit ion drifts	296	**336**	186	**225**
EMPIRE ingesting grid ion drifts	181	433	101	262

gridded data ($\vec{v}_{lp}$ in Figure 4.1(d)) provided by KAP and SAS sites that are not ingested by the EMPIRE algorithm. The magnetic bearing angles γ are provided by the data, and EMPIRE drift components are projected onto the same direction as $\vec{v}_{lp}$. Figure 4.8 shows the comparison results. SAMI3 outputs are denoted by magenta lines, and the EMPIRE baseline (case 1) estimations are plotted by blue lines. The

EMPIRE augmentation cases of ingesting superDARN fit and grid data are indicated by gold and red lines, respectively. Figure 4.8(a) is the comparison with KAP site measurements, and Figure 4.8(b) is with the SAS site measurements in black lines. From Figure 4.8(a), EMPIRE baseline case is very close to the case of ingesting fit SuperDARN data and SAMI3. As for the comparison with SAS site, cases (1) and (3) yield more agreement after 1700 UT on 17th.

The mean error and residual sigma are given in Table 4.3. From the comparison with KAP site, the SAMI3 model yields the lowest mean error of 172 m/s, and the EMPIRE case of ingesting grid ion drifts gives a higher mean error of 181 m/s. The mean errors for the case (2) of augmenting fit ion drift and baseline case are 296 m/s and 193 m/s, respectively. The EMPIRE case (2) yields the lowest residual sigma of 336 m/s, and SAMI3 model residual sigma is 360 m/s. Case (3) yields a lower residual sigma value (433 m/s) than the baseline case (464 m/s). For the comparison with SAS site, EMPIRE baseline case yields the lowest mean error value of 89 m/s, and the EMPIRE case of ingesting fit ion drifts yields the highest mean error of 186 m/s. The residual sigma calculated from EMPIRE case (2) is the lowest as 225 m/s, and the EMPIRE baseline case reaches the highest residual sigma value of 281 m/s.

4.4 Conclusion

The EMPIRE algorithm serves as a data assimilation technique designed to estimate the ionospheric drivers of electric potential and neutral wind. Primarily led by the ion continuity equation, this algorithm now incorporates direct measurements of ion drifts. The integration of ion drift measurements from SuperDARN sites is explored to assess potential improvements in the estimation of electric potential and ion drift. This study focuses on augmenting ion drift measurements obtained from SuperDARN sites at northern mid-to-high latitudes. The outputs are validated against the ion velocity vector derived from the MHISR and two ion velocity datasets from

SuperDARN. The March 2015 geomagnetic storm is selected for analysis due to data availability.

The comparisons reveal that the EMPIRE augmentation case ingesting fit line-of-sight SuperDARN data exhibits slightly closer alignment with MHISR measurements in the field-perpendicular meridional direction at the geomagnetic latitude of 56° N, than the SAMI3 model, the EMPIRE baseline case, and the case ingesting SuperDARN grid data. The lack of improvement in estimates even when ingesting grid data may be attributable to the data processing to produce the gridded outputs, which are projected onto the horizontal plane at 300 km. In contrast, the SuperDARN fit data provides line-of-sight velocities at a variety of latitudes, longitudes and altitudes throughout the ionosphere, giving more measurements overall. Over the entire analysis period, the quantity of fit data inputs to EMPIRE (case (2)) is larger than the total number of gridded data inputs (case (3)) by approximately 20 times, and this number is comparable to the total number of electron density rates ingested into EMPIRE.

Compared to the MHISR field-perpendicular zonal drift measurements at the geomagnetic latitude of 62°, SAMI3 demonstrates the lowest mean error. The lack of improvement of EMPIRE estimates at high latitudes, even when ingesting drift data at high latitudes is very likely due to large EMPIRE fitting errors observed at high-latitude regions in the field-perpendicular zonal direction [4].

The SAMI3 and EMPIRE cases are further evaluated against SuperDARN gridded data. The SAMI3 model and EMPIRE baseline case demonstrate the lowest mean errors for KAP and SAS sites, respectively. However, when EMPIRE incorporates SuperDARN fit ion drifts, it achieves slightly lower residual sigma values that are a few percent smaller than the SAMI3 model residuals.

One obvious concern is that the posterior state variance cannot fully capture the true state, indicated by the error bars do not encompass site measurement error bars in Figure 4.7 and Figure 4.8. The outputs are attributed to algorithm limitations, specifically the assumption of a single ion species within the ionosphere and the elimination of observation and state correlations. The simplifications lead to biased Kalman gain calculations in the computation of global state. Hence, future investigations are required for analyzing the error statistic inputs to the Kalman filter.

In conclusion, systematic errors in the EMPIRE are evidenced by prior studies [31] indicating much larger mapping matrix fitting errors exist for estimating electric potential at high latitudes compared to low-to-mid latitudes. As high-latitude measurements are incorporated, it becomes imperative to account for systematic errors within the calculation processes. The findings of this study indicate that augmenting high-latitude ion drifts from SuperDARN line-of-sight ion velocities provides more information in EMPIRE driver calculations, to conteract with the EMPIRE systematic errors from the fitting function.

CHAPTER 5

INVESTIGATION OF THE NILE DRIVING MECHANISM VIA EMPIRE AND WACCM-X+DART

Ionospheric nighttime enhancement is a phenomenon that has been widely studied in the past decades. Global Ionospheric Maps (GIM) have shown nighttime electron density over the equatorial ionosphere [139]. The ionospheric electron density generally decreases after sunset due to recombination, but sometimes nighttime enhancements are observed [140]. Characteristics of ionospheric nighttime enhancement have been studied in the mid-to-high latitude region, after they noted that previous papers focused on the low-to-mid latitude region [141]. Studies have also used COSMIC satellite measurements to analyze nighttime enhancement in F region electron density at mid-latitudes [142]. An analysis of seasonal morphology and solar activity dependence has shown anomalous enhancement of nighttime in the mid-latitude ionosphere, characterized by an increase in electron density of the ionospheric F2 layer [143, 144].

During some geomagnetic storms, there is an observed concentrated region of elevated TEC over the southeastern United States, referred to as a NILE, consistently co-rotating with the Earth from approximately 18:00 local time (LT) to 24:00 LT. A NILE was primarily detected by the dual-frequency GPS network, incorporating Continuously Operating Reference Station (CORS), International GNSS Service (IGS), WAAS, and Caribbean-North American Plate Boundary Experiment (CANAPE) [20]. The significant TEC concentration and its sustained occurrence threaten the accuracy and integrity of satellite-based augmentation system users' position estimations. The observation of the NILE led to the development of the 8-hour time window of the WAAS Extreme Storm Detector (ESD) hysteresis [47, 20, 145].

An examination of the NILE during the storm events of August 2018 and November 2003 was conducted [21] using the data assimilation tool IDA4D [26] coupled with the ionosphere model SAMI3 [32]. The investigation tracks the evolution of a NILE in terms of occurrence time and geographical region, and validates the findings from IDA4D/SAMI3 with GPS and ionosonde data. NILE events are found to be apparent between $30°N$ and $40°N$ at American sector, during the local nighttime of the recovery phase of some storms. In comparison to the more global effects observed in October 2003, these mid-latitude events exhibited lower plasma concentration in spatial extent and reduced severity in density. Another study [146] indicates the ionospheric night enhancements were observed on quiet days of 15 November 2020 and 2 December 2020. The enhancements are observed at low latitudes and near conjugate longitudes (F2 layer density peaks near $18°N$ $110°E$ reaching the extent of approximately 11° longitude by 34° latitude) with amplitudes reaching up to several TECU [146]. These findings raise questions about whether the effects observed in these storms or quiet time at mid-latitudes could appropriately be categorized as a NILE. Also, it indicates NILE events may originate from enhancements at low latitudes being transported to mid-latitudes due to driving forces that need to be investigated.

The objective of this chapter is to validate the physical mechanisms underlying NILE occurrence. One proposed explanation for the formation of NILE is the concept of the polarization terminator [48], that a NILE was attributed to upward and northward plasma transport around the dusk terminator, driven by eastward polarization electric fields, from EIA region to higher latitudes. The dusk terminator generates an electric field associated with plasma drifts, which might contribute to the localized enhancement. The crucial driving forces of neutral wind and electric fields during storm periods can be analyzed to represent the plasma motion regional map where the NILE is formed.

In this study, the focus is on exploring the NILE effect by examining the theories of ionospheric behavior during storm events hypothesized in the literature and establishing a systematic methodology to test these theories. I specifically analyze the geomagnetic storm that occurred on 17 March 2015, ingesting 4D electron density rate maps from the IDA4D/SAMI3 algorithm and incorporating ion drift measurements from SuperDARN radar sites, to enhance our understanding of global physical drivers at the NILE location. Another data assimilation algorithm, WACCM-X+DART is implemented for TEC map and global physical drivers. The EMPIRE estimations of ion drift over Miami, Florida, and their implications for the presence of the PRE and the PT in contributing to a potential NILE phenomenon are discussed subsequently.

5.1 Physical principle investigation underlying NILE

Three major questions were proposed initially to explore in the theoretical explanation of NILE: **1) Where and when does a NILE occur? 2) Do the properties of the NILE correlate with the severity of the storm? 3) What is the plasma source of the NILE?**

Before we answer these questions, 4 storm events categorized by solar severity are selected listed in the Table 5.1, that November 2003 storm happens in the 23rd solar cycle and the other three are in the 24th solar cycle. The minimum Dst value, peak time, and the storm categorization for each storm is listed in Table 1.1.

Table 5.1. Storm event list in chronological order with minimum Dst values and Universal Time hour of minimum Dst

Storm event date	Universal Time (UT) hour	Minimum Dst [nT]	Category
November 20th 2003	21 & 22	-422	Great
March 17th 2015	23	-234	Severe
September 28th 2017	07	-56	Moderate
August 26th 2018	10	-156	Strong

Electron density information is provided by the Madrigal database [147], and processed by MIT Automated Processing of GPS (MAPGPS) to obtain global TEC maps [148], also to provide an overview of the storm time ionospheric plasma. [149] primarily determined NILE as a storm-related phenomenon that happened in the recovery phase as an enhanced density at the Florida region during local nighttime, hence the ratio of vertically integrated electron density over the mean value of vTEC (treated as the background value of TEC) is plotted for each storm. The ratio threshold for defining NILE occurrence is selected to be 1.5.

5.1.1 Storm event on November 2003. Figure 5.1 shows the storm characteristics from November 19th to 21st 2003. The subplot 5.1(a) indicates the main phase starts from 4 UT to 22 UT on November 20th, with the minimum Dst value of -422 nT at 22 UT on 20 November 2003. From subplot 5.1(b), the maximum proton density exceeds 30 cm^{-3} is observed at near the time of minimum Dst, and the maximum proton speed of approximately 750 km/s happens at 08 UT on the 20th. From subplot 5.1(c), the IMF turns southward at 10 UT on the 20th and reaches the maximum strength of 50 nT at 14 UT. It continues to be southward until 00 UT on November 21st, and northward with a duration of 4 hours during the recovery phase.

Figure 5.2 provides a map of GNSS vertically integrated electron density ratio over North America during the storm initial phase on 20 November 2003 and recovery phase on 21 November 2003, at time epochs of 00 UT, 02 UT, 04 UT and 06 UT, which are local times in Florida of 19 LT, 21 LT, 23 LT, 1 LT, respectively. Compared to the initial phase vTEC map at 00 UT, the enhancement at Florida region is 1.5 times more than the background value and extends pole-ward and westward to higher latitudes during the recovery phase. For the initial phase, the plasma appears to move westward and pole-ward along the west side of the North American continent

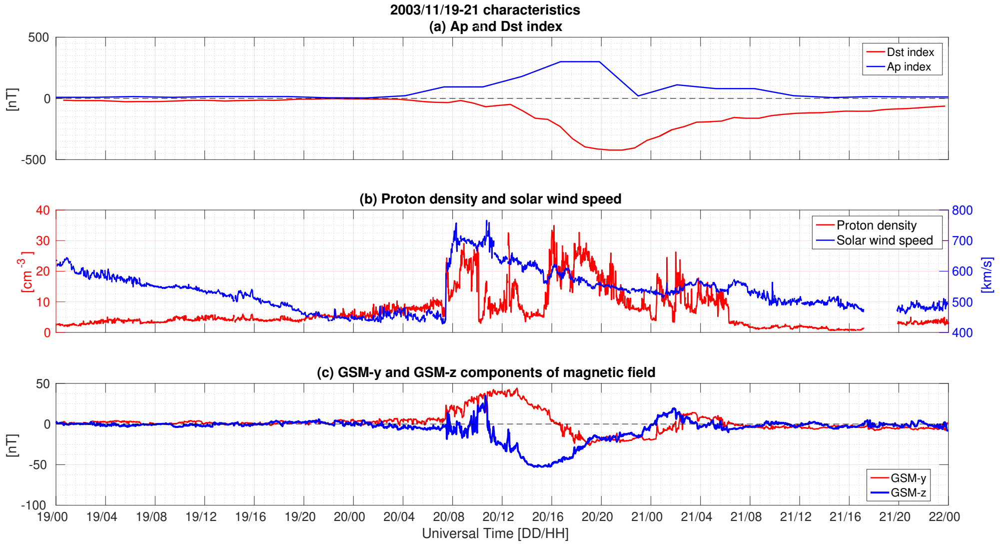

Figure 5.1. Storm characteristics of (a) Ap and Dst index $[nT]$ produced from WDCG [1], (b) Proton density $[cm^{-3}]$ and solar wind speed $[km/s]$, (c) GSM-y and GSM-z components of magnetic field $[nT]$, from November 19th to 21th 2003. The subplots (b) and (c) are plotted from ACE satellite observations [2].

at 02 UT, and the ratio is below 1 at the Florida region from 02 UT and 06 UT. During the recovery phase, the enhancement persistently co-rotates with the Earth at the Florida region during the recovery phase, with twice the background value of equivalent vertical TEC until 06 UT.

5.1.2 Storm event on March 2015. The characteristics of the storm from March 16th to 18th, are shown in Figure 5.3. In subplot 5.3 (a), the initial phase starts from 4 UT to 6 UT 17th with a Sudden Storm Commencement (SSC), and main phase is shown to span from 6 UT to 23 UT 17th, with the lowest Dst value of -234 $[nT]$. Subplot 5.3 (b) indicates that the proton density measurements are missing from 6 UT to 16 UT 17th. From the available information, proton density reaches 34 $[cm^{-3}]$ at 4UT, while the maximum proton speed of approximately 750 $[km/s]$ occurs during the recovery phase at 20 UT 18th. Subplot 5.3 (c) displays the IMF strength measurements, which is increased initially in northward direction before shifting southward at 6 UT on the 17th, and oscillating between ± 20 $[nT]$

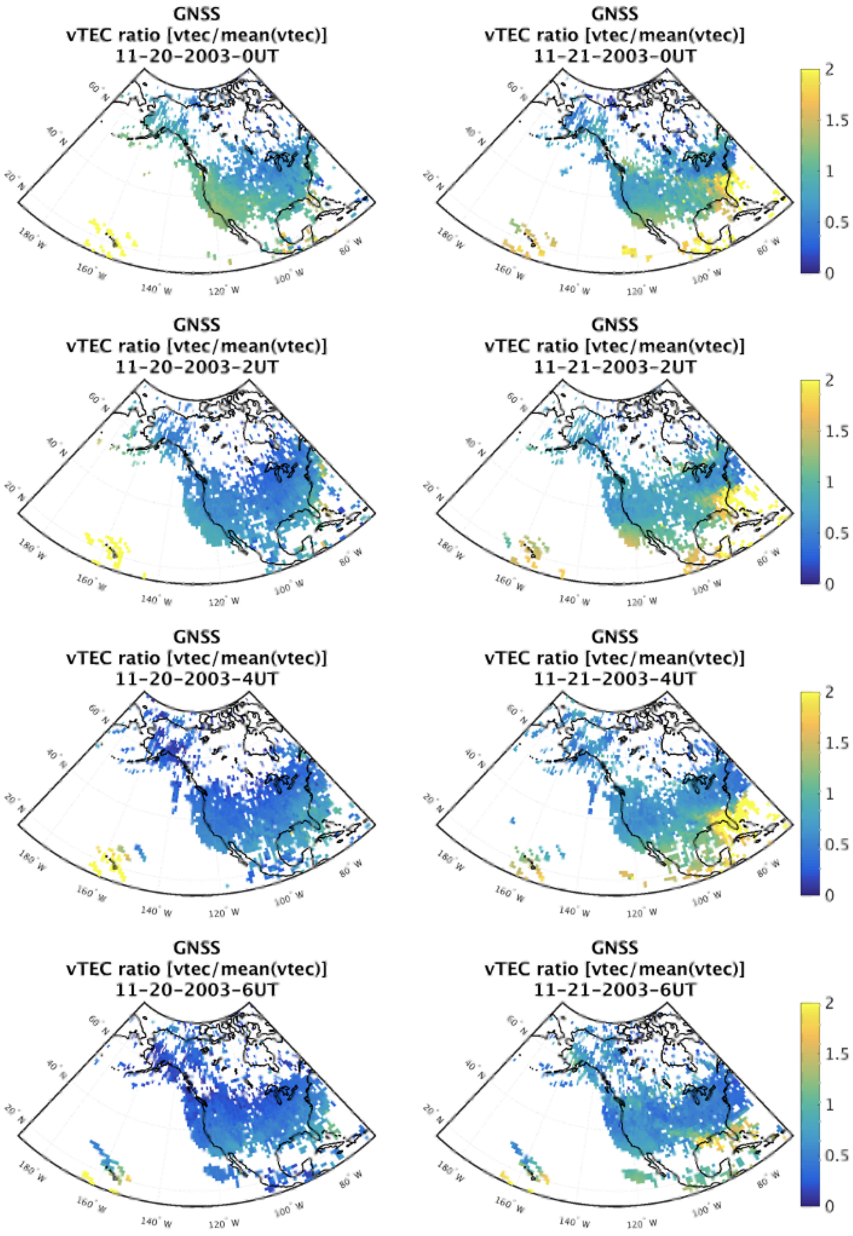

Figure 5.2. Vertically integrated GNSS electron density measurement on November 20th and 21th 2003 at 0UT, 2UT, 4UT and 6UT, in units of log10(TECU) as the color-bar.

until 12 UT, then remains to be southward in the rest of main phase.

Figure 5.4 provides a north America map of GNSS vertically integrated electron density ratio during the initial phase on March 17th and recovery phase on March

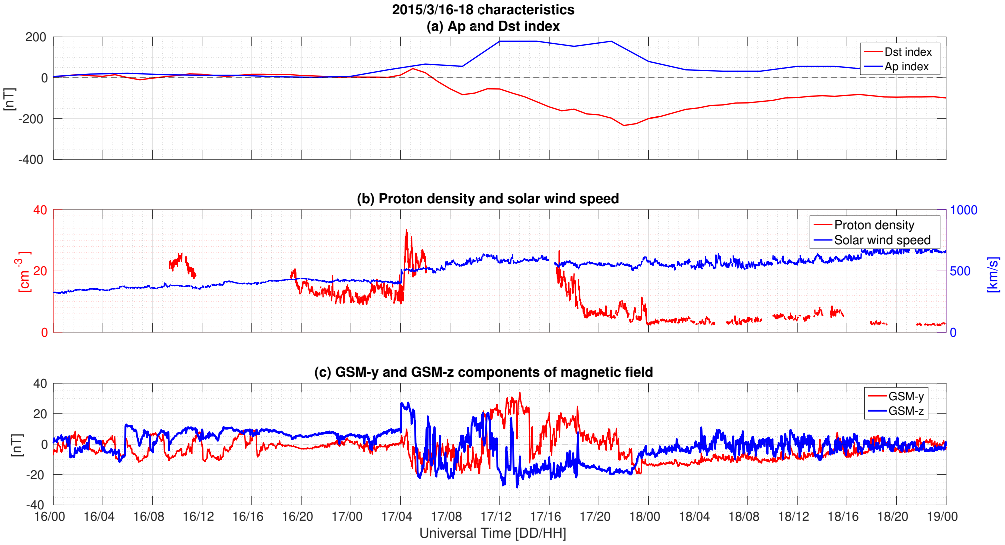

Figure 5.3. Storm characteristics of (a) Ap and Dst index $[nT]$ produced from WDCG [43], (b) Proton density $[cm^{-3}]$ and solar wind speed $[km/s]$, (c) GSM-y and GSM-z components of magnetic field $[nT]$, from March 16th to 18th 2015. The subplots (b) and (c) are plotted from ACE satellite observations [2].

18th 2015, at time epoch of 0 UT, 2 UT, 4 UT and 6 UT (Florida 19 LT, 21 LT, 23 LT, 1 LT). Compared to the initial phase vTEC map at 0 UT, the enhancement at Florida region exceeds twice more than the background value and extends pole-ward and westward to higher latitudes during the recovery phase. One thing to note is a slightly higher enhancement ridge is observed at 40^oN180^oW on March 17th. For the initial phase, the plasma appears move westward and pole-ward along the west-side of north America continent at 2UT, and the ratio is below 1 at the Florida region from 2 UT and 6 UT, but above 1 at west-side of America map. As for the recovery phase, the enhancement persistently co-rotates with the Earth near the Florida region and above carribean during the recovery phase, with 1.5 times more than the background value until 6 UT.

5.1.3 Storm event on September 2017.

The storm characteristics observed 27-29 September 2017 are presented in Figure 5.5. Subplot 5.5(a) showcases the main phase extends from 08 UT on the 27th to 09 UT on the 28th, reaching its minmum

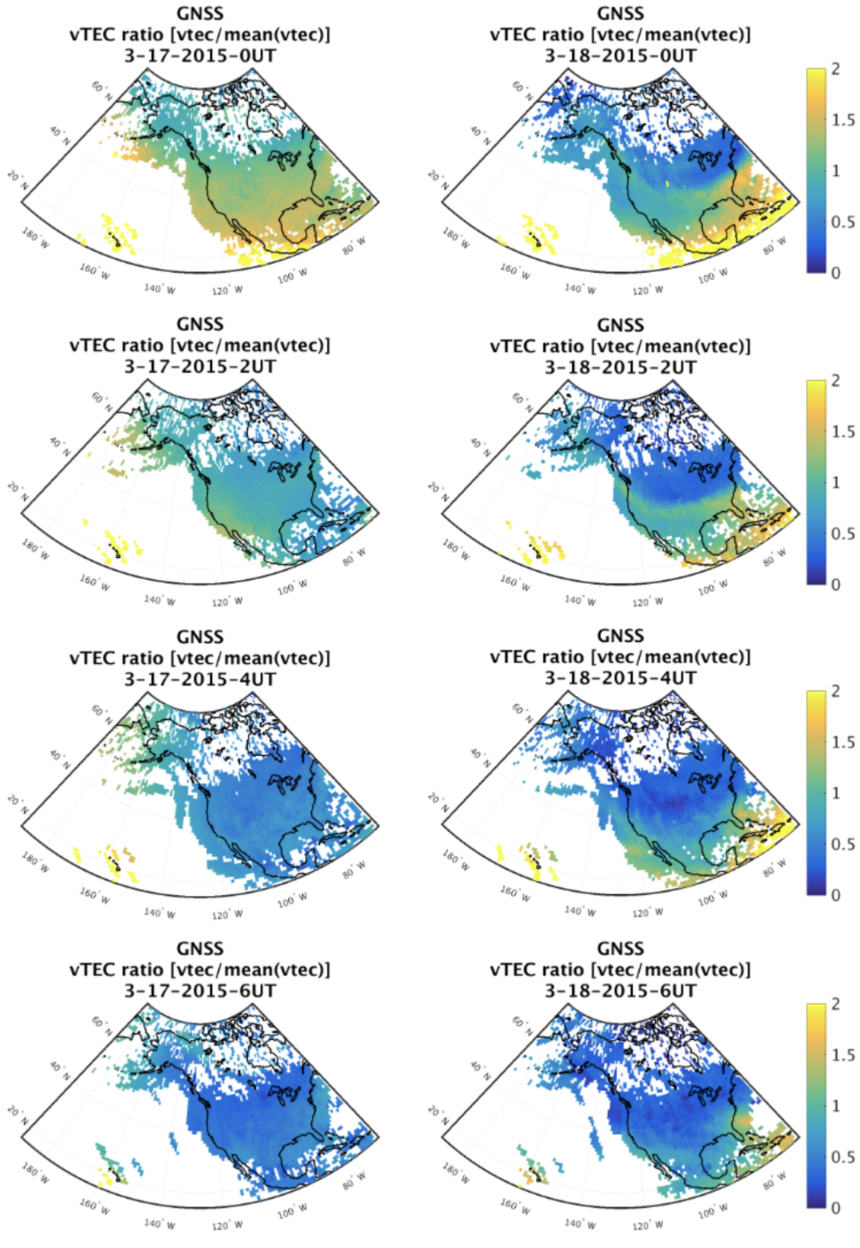

GNSS vTEC ratio [vtec/mean(vtec)] 3-17-2015-0UT

GNSS vTEC ratio [vtec/mean(vtec)] 3-18-2015-0UT

GNSS vTEC ratio [vtec/mean(vtec)] 3-17-2015-2UT

GNSS vTEC ratio [vtec/mean(vtec)] 3-18-2015-2UT

GNSS vTEC ratio [vtec/mean(vtec)] 3-17-2015-4UT

GNSS vTEC ratio [vtec/mean(vtec)] 3-18-2015-4UT

GNSS vTEC ratio [vtec/mean(vtec)] 3-17-2015-6UT

GNSS vTEC ratio [vtec/mean(vtec)] 3-18-2015-6UT

Figure 5.4. Ratio of integrated GNSS electron density measurement over the mean measurement value on March 17th and 18th 2015 at 0UT, 2UT, 4UT and 6UT. The colorbar indicate the ratio value of between 0 and 2.

Dst value of -56 nT. In subplot 5.5(b), observations indicate a spike in proton density to 50 cm^{-3} at 04 UT on the 27th, while the maximum proton speed exceeds 700 km/s is recorded during the main phase at 10 UT on the 28th. Subplot 5.5 (c)

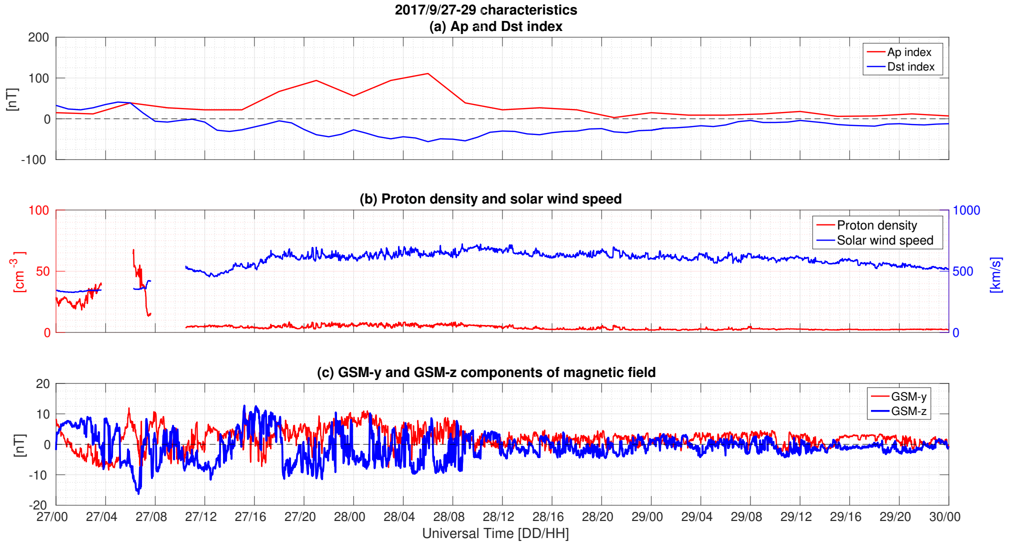

Figure 5.5. Storm characteristics of (a) Ap and Dst index $[nT]$ plotted from WDCG [1], (b) Proton density $[cm^{-3}]$ and solar wind speed $[km/s]$, (c) GSM-y and GSM-z components of magnetic field $[nT]$, from September 27th to 29th 2017. The subplots (b) and (c) are plotted from DSCOVR satellite observations [3].

indicates a sudden southward IMF measurement of -100 nT at 08 UT on the 27th, and oscillating randomly between -100 $[nT]$ to 20 $[nT]$ in the rest of the main and recovery phases. Figure 5.6 provides a North America map of GNSS vertically integrated electron density ratio during the main phase on September 28th and recovery phase on September 29th 2017, at time epochs of 00 UT, 02 UT, 04 UT and 06 UT (Florida 20 LT, 22 LT, 24 LT, 2 LT). At 00 UT on September 28th, the enhancement is more than twice the background value over the Mexico region, while the same scale of enhancement is only observed over the western part of Mexico at 00 UT on September 29th with the ratio value between 1 and 1.5. At 02 UT during the main phase, the enhancement with an approximate ratio value of 1.5 is observed at the Florida region, which forms a narrow north-west band of enhancement and extends to 60° N. As for 02 UT during the recovery phase, the ratio value above 1 shows the electron density is slightly enhanced along the west boundary of north America map, and no enhancement is observed at Florida region. The ratio values drops below 1.5 for both

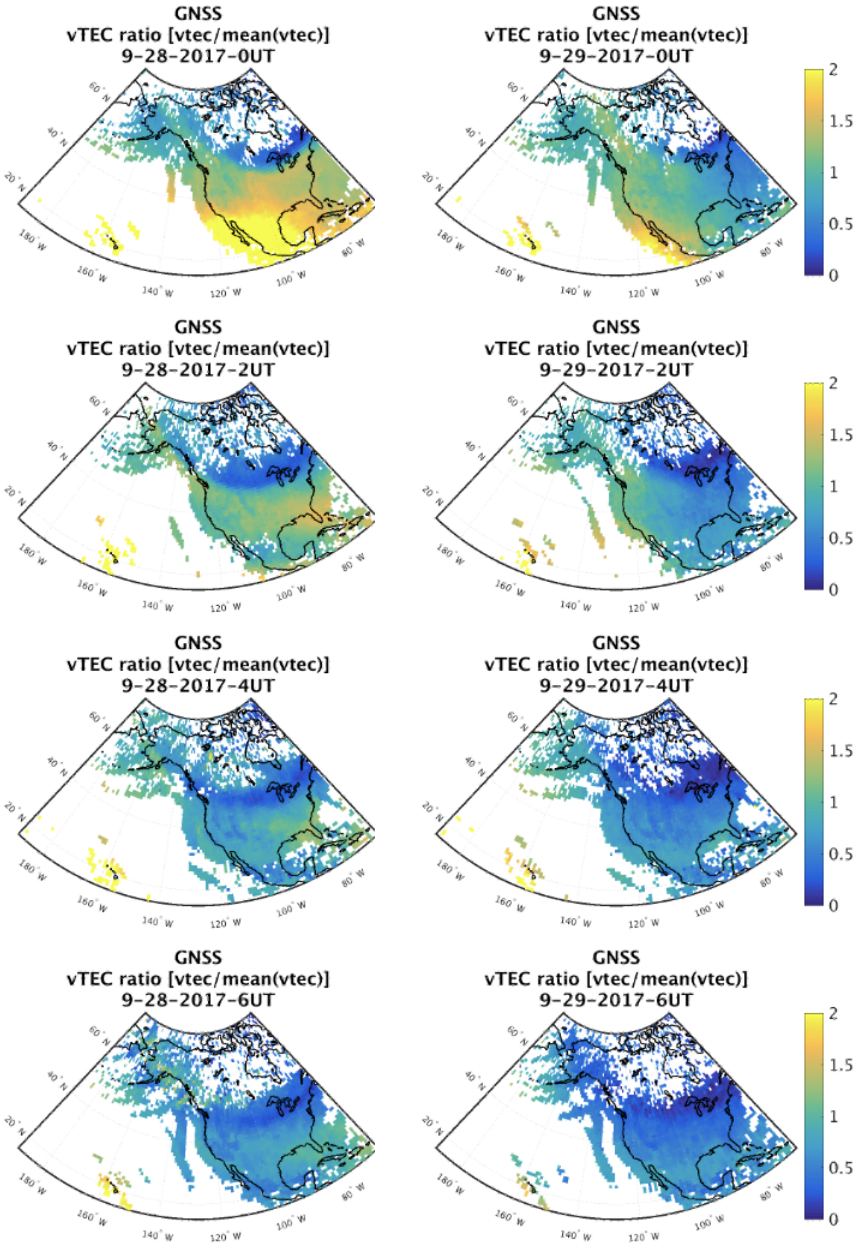

Figure 5.6. Ratio of integrated GNSS electron density measurement over the mean measurement value on September 28th and 29th 2017 at 0UT, 2UT, 4UT and 6UT. The colorbar indicate the ratio value of between 0 and 2.

04 UT and 06 UT on then 28th and 29th, implying the enhancement dissipation.

5.1.4 Storm event on August 2018. The solar wind and geomagnetic indices for the August 2018 storm are shown in Fig. 5.7. From subplot 5.7(a), the main phase lasts from 16 UT on the 25th to 06 UT on the 26th with the minimum Dst value of -156 nT. The subplot 5.7(b) shows the maximum proton density of 25 cm^{-3} at the start of the recovery phase at 14 UT on the 26th, and maximum solar wind speed of 550 km/s at 22 UT. The subplot 5.7(c) shows the southward IMF starts at 16 UT on the 25th, returning to the nominal state at 20 UT on the 26th.

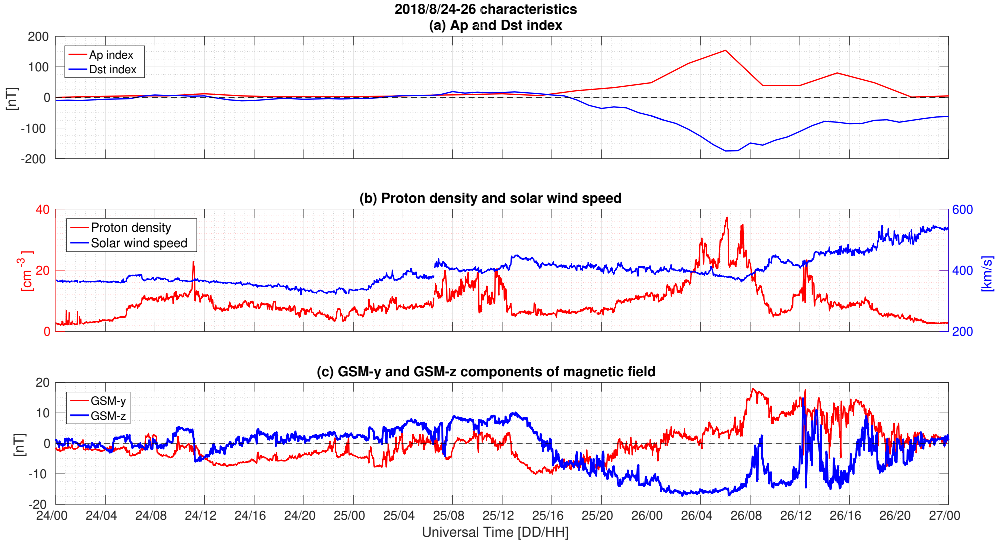

Figure 5.7. Storm characteristics of (a) Ap and Dst index $[nT]$, and is produced from WDCG [1] (b) Proton density $[cm^{-3}]$ and solar wind speed $[km/s]$, (c) GSM-y and GSM-z components of magnetic field $[nT]$, from August 25th to 27th 2018. The subplot (b) and (c) are plotted from DSCOVR satellite observations [3].

Figure 5.8 provides a map of GNSS vertically integrated electron density ratio over North America during the quiet time on August 25th and recovery phase on August 26th 2018, at 00 UT, 02 UT, 04 UT and 06 UT (Florida 20 LT, 22 LT, 24 LT, 2 LT). At 00 UT on 25 August 2018, the enhancement forms below latitude band of $40°N$, and extends along the west boundary of North America continent from 02 UT to 04 UT, then reaches $60°N180°W$. The enhancement covers the US continent at 00 UT on August 26th, and forms two ridges over the central US and Pacific Ocean which extends to mid-latitudes at 02 UT. At 04 UT on August 26th, only one ridge at the west coast of the US is observed, and reaches a high-latitude band of

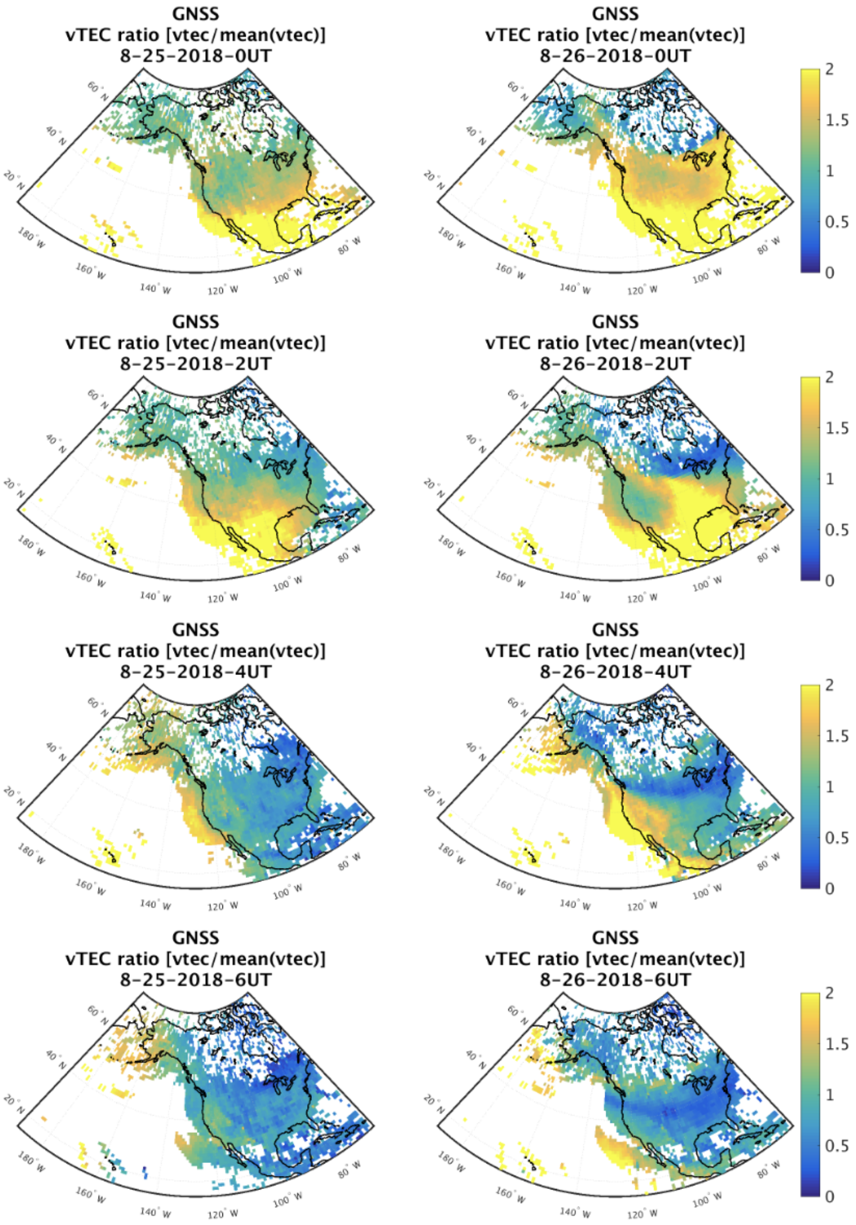

Figure 5.8. Ratio of integrated GNSS electron density measurement over the mean measurement value on August 25th and 26th at 0UT, 2UT, 4UT and 6UT. The colorbar indicate the ratio value of between 0 and 2.

$60°N$ with northwest plasma motion, then the bridge is "disconnected " between the mid-latitude and low-latitude enhancements.

A NILE occurrence is initially defined as enhancement at the Florida region and co-rotates with the Earth during local nighttime until mid-night. By comparing the vTEC to the mean value of vTEC, we define the NILE as having occurred when the ratio value exceeds 1.5 at Florida region. From the above listed storms, NILE is observed during the recovery phase of November 2003 and March 2015 storms, and the main phase of September 2017. As for August 2018 storm, it is a different case in which larger enhancements at west edge of US continent appear to be transported to mid-to-high region near Alaska.

The NILE time span is also different for each storm. For the great and severe storms (November 21, 2003 and March 18, 2015), the vTEC ratio near the Florida region is higher at 04 UT than 02 UT, and the vTEC ratio value of more than 1.5 can still be observed at 06 UT. However for the moderate storm event on September 28, 2017, the NILE is observed at 02 UT, but the density drops quickly after 04 UT. For the strong storm on August 26, 2018, the enhancement is observed near the Florida region from 00 UT to 02 UT but dissipates at 04 UT and afterwards.

Among these 4 map sequences of vTEC ratios, one common phenomena during storm time that can be observed is that the plasma appears to be transported from the lower latitudes to higher latitudes, which contributes to larger enhancement measurements over the Alaska region. Also, the enhancements along US west coast seems to be another contributor to high-latitude enhancements (most obvious on the storm event of August 26, 2018).

Some useful information can be obtained from the vTEC ratio maps: 1) a NILE happens near the Florida region during local nighttime. 2) NILE is more evident when the geomagnetic activity level is higher. 3) One hypothesis is made for plasma enhancement, that plasma is transported from the low latitudes to high latitudes with westward and poleward motion. But what causes this motion? Models do not model this behaviors. Data assimilation algorithms can be a useful tool to present a more comprehensive understanding of nighttime ionospheric behavior.

The NILE driving mechanism was initially proposed to be driven by the combined effects of PRE and PT described in Section 2.4, that plasma is transported westward and poleward, forming an enhancement over the Florida region. To test the theory, an experiment implementing WACCM-X + DART and EMPIRE algorithms as two separate independent DA methods will be used, providing insights about electron density and ionospheric drivers of ion drifts in this contribution.

5.2 Experimental setup

In this study, our primary focus lies on understanding the role of ion drifts as a significant driver for NILE phenomenon. Figure 5.9 provides an overview of the methodology which separately implements the WACCM-x + DART and EMPIRE algorithms to comprehensively analyze and visualize global patterns of electron column densities and ion drifts. By leveraging these advanced computational tools, we aim to gain insights into the complex dynamics of ionospheric processes. The selection of 17 March 2015 as the target storm event for our investigation into the NILE phenomenon is based on data availability for assimilation. This particular event offers a wealth of data due to the existence of denser GNSS measurements compared to other storms, such as the Halloween storm of 2003. This increased spatial and temporal resolution of the GNSS data provides a more robust dataset for our analysis, enabling us to capture finer-scale variations in ionospheric behavior. The analysis period for WACCM-X + DART is 10 days from March 10th to 20th 2015, and EMPIRE runs from March 16th to 18th 2015.

Figure 5.9 is a flowchart shows the outputs from WACCM-X + DART and EMPIRE data assimilation algorithms. The outputs of electron column density (*ElecColDens*) from WACCM-X + DART is an indicator of NILE occurrence during the March 2015 storm event. Ion drifts **V** from both of WACCM-X + DART and EMPIRE algorithms give two separate global views of ion drifts, and show how plasma is transported under $E \times B$ effect to investigate whether the PT and PRE contribute to the NILE formation.

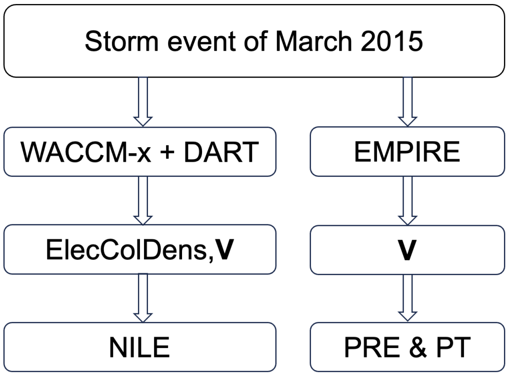

Figure 5.9. Flowchart of WACCM-x + DART and EMPIRE data assimilation algorithms with the outputs on March 17th storm. ElecCloDens is the electron column density, and **V** is the ion drift vector. NILE refers to the Nighttime Ionospheric Localized Enhancement. Pre-reversal enhancement and Polarization Terminator are denoted as PRE and PT respectively.

WACCM-X couples with physics at lower atmosphere and solar influences, self-consistently solves for global electrodynamics, and transport of O^+ in the F-region [150]. The ionospheric electrodynamics is built upon TIEGCM [151, 152], driven by the low-to-mid wind dynamo and empirical ion convection patterns at high latitudes from Heelis [153]. EMPIRE, driven by the continuity equation uses time-differenced electron density from SAMI3/IDA4D as measurements. The modeled transports are based on the Kirchengast model [93]. The neutral densities and temperatures are provided by MSIS [135], and HWM14 [137] produces the neutral wind global map. SAMI3 [94] is the source for electric potential, ion and electron temperatures for

Table 5.2. Spatial and temporal resolution for WACCM-x + DART and EMPIRE

Resolution	WACCM-x + DART	EMPIRE
Horizontal [Lat × Lon]	1.9 × 2.5 [degs]	6 × 6 [degs]
Vertical	Pressure [hpa]	50 [km]
Time	1 hr	20 mins

model transport. No augmentation with ion drifts is used.

Table 5.2 presents an overview of the spatial and temporal resolutions for the WACCM-X + DART and EMPIRE algorithms utilized in our study. The capability of WACCM-X + DART is to provide high-resolution data, yielding detailed insights into ionospheric dynamics. Specifically, it achieves a spatial resolution of 1.9 degrees and 2.5 degrees for latitude and longitude, respectively, on the horizontal map. The vertical scale is defined by pressure variance along with altitude. In contrast, EMPIRE offers a slightly coarser spatial resolution, with a horizontal resolution of 6 degrees for both latitude and longitude. However, it maintains a vertical cadence of 50 kilometers, ensuring adequate coverage of the ionospheric profile. Additionally, EMPIRE calculates its outputs at 20-minute intervals, providing a fine-grained temporal resolution that captures rapid changes in ionospheric parameters.

5.2.1 Data inputs to EMPIRE.

Figure 5.10 presents the SAMI3/IDA4D global maps of vertically integrated electron content on $\log_{10}$ scale at 00 UT, 02 UT, 04 UT and 06 UT March 18th, from which the NILE is observed until Florida local midnight. The SAMI3/IDA4D assimilated GNSS TEC measurements, and its outputs of electron density from March 16th to March 18th are time-differenced to serve in observation vector $\mathbf{z}$ ingested to EMPIRE.

5.3 Results

Figure 5.11 provides a global map of vertical TEC on $\log_{10}$ scale from WACCM-X + DART algorithm, at 00 UT, 02 UT, 04 UT, 06 UT on March 18th.

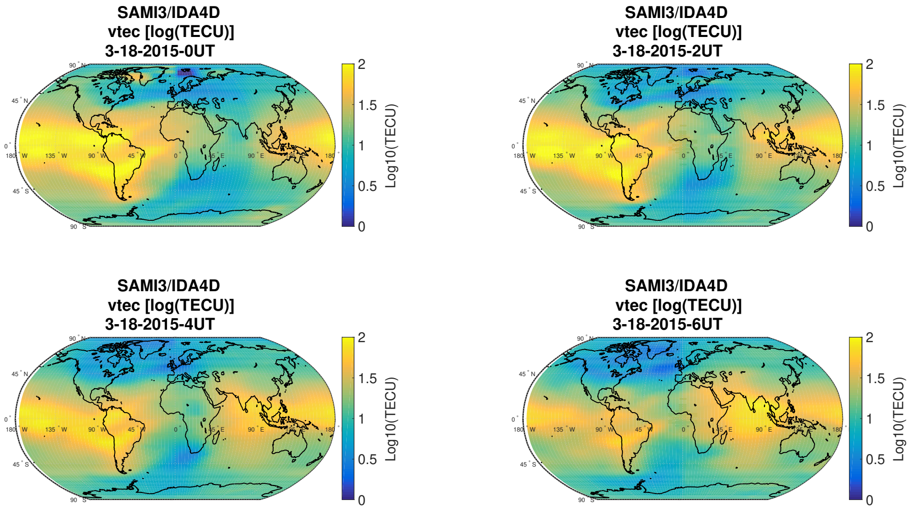
SAMI3/IDA4D
vtec [log(TECU)]
3-18-2015-0UT

SAMI3/IDA4D
vtec [log(TECU)]
3-18-2015-2UT

SAMI3/IDA4D
vtec [log(TECU)]
3-18-2015-4UT

SAMI3/IDA4D
vtec [log(TECU)]
3-18-2015-6UT

Figure 5.10. SAMI3/IDA4D global map of vertically integrated total electron content at 00 UT, 02 UT, 04 UT and 06 UT on 18 March 18 2015.

NILE is also observed on WACCM-X + DART outputs, and peak densities (i.e. EIA) can also be referred from Figure 5.11. The background TEC near the prime meridian is more closer to 0, which is different from SAMI3/IDA4D results (i.e., Figure 5.10 indicate the nighttime $\log_{10}(TECU)$ is between 0.5 to 1).

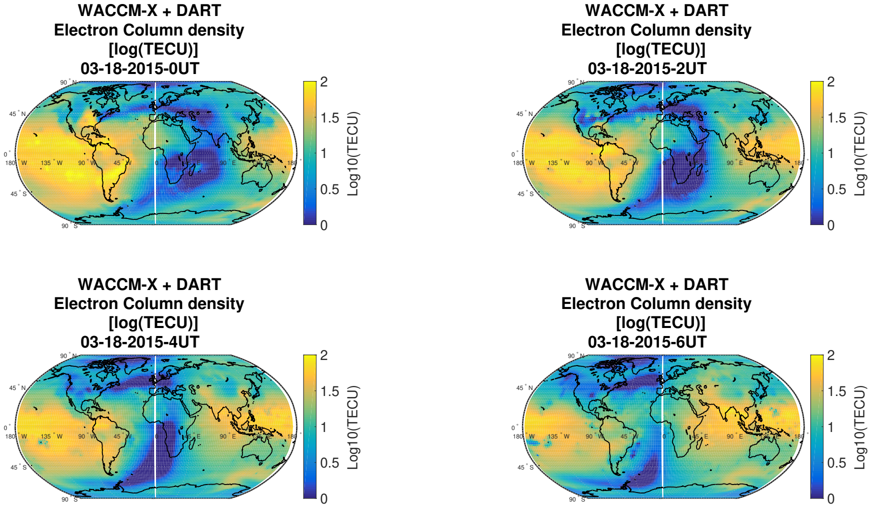
WACCM-X + DART
Electron Column density
[log(TECU)]
03-18-2015-0UT

WACCM-X + DART
Electron Column density
[log(TECU)]
03-18-2015-2UT

WACCM-X + DART
Electron Column density
[log(TECU)]
03-18-2015-4UT

WACCM-X + DART
Electron Column density
[log(TECU)]
03-18-2015-6UT

Figure 5.11. WACCM-X+DART global map of electron column density (i.e. TEC) at 00 UT, 02 UT, 04 UT and 06 UT on March 18th.

Figure 5.12 is a zoomed in view of the vertical TEC ratio over the North American continent. At 00 UT on March 18th, an enhancement of vTEC ratio exceeding 1.5 indicates NILE occurrence, and large electron density is also observed at the high latitude region of $60^{\circ}N160^{\circ}W$. After 02 UT, the high-latitude enhancement dissipates and the one over Florida decreases but does not disappear.

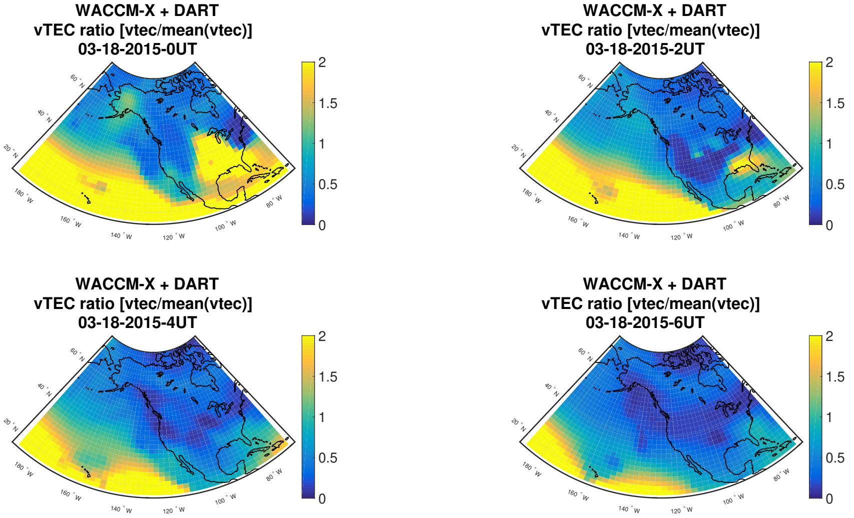
WACCM-X + DART vTEC ratio [vtec/mean(vtec)] 03-18-2015-0UT

WACCM-X + DART vTEC ratio [vtec/mean(vtec)] 03-18-2015-2UT

WACCM-X + DART vTEC ratio [vtec/mean(vtec)] 03-18-2015-4UT

WACCM-X + DART vTEC ratio [vtec/mean(vtec)] 03-18-2015-6UT

Figure 5.12. WACCM-X+DART US continent map of vTEC ratio at 00 UT, 02 UT, 04 UT, and 06 UT on 18 March 2015.

Figure 5.13 shows WACCM-X + DART ion velocity quiver plot at 20 UT on March 17th to 06 UT on March 18th with a 2-hour time step. At low latitudes, the westward ion drift turns eastward is observed at 0 UT on March 18th, which indicates a circulation pattern below Florida region. Local nighttime is shaded gray. At the Florida region, ions move westward and poleward until 04 UT on March 18th, and then turn equatorward at 06 UT.

Figure 5.14 is the ion velocity quiver plots corrected by EMPIRE, from 20 UT on March 17th to 06 UT on March 18th, with 2 hours cadence. It's observed that the dusk terminator appears slightly different compared to Figure 5.13 for each time

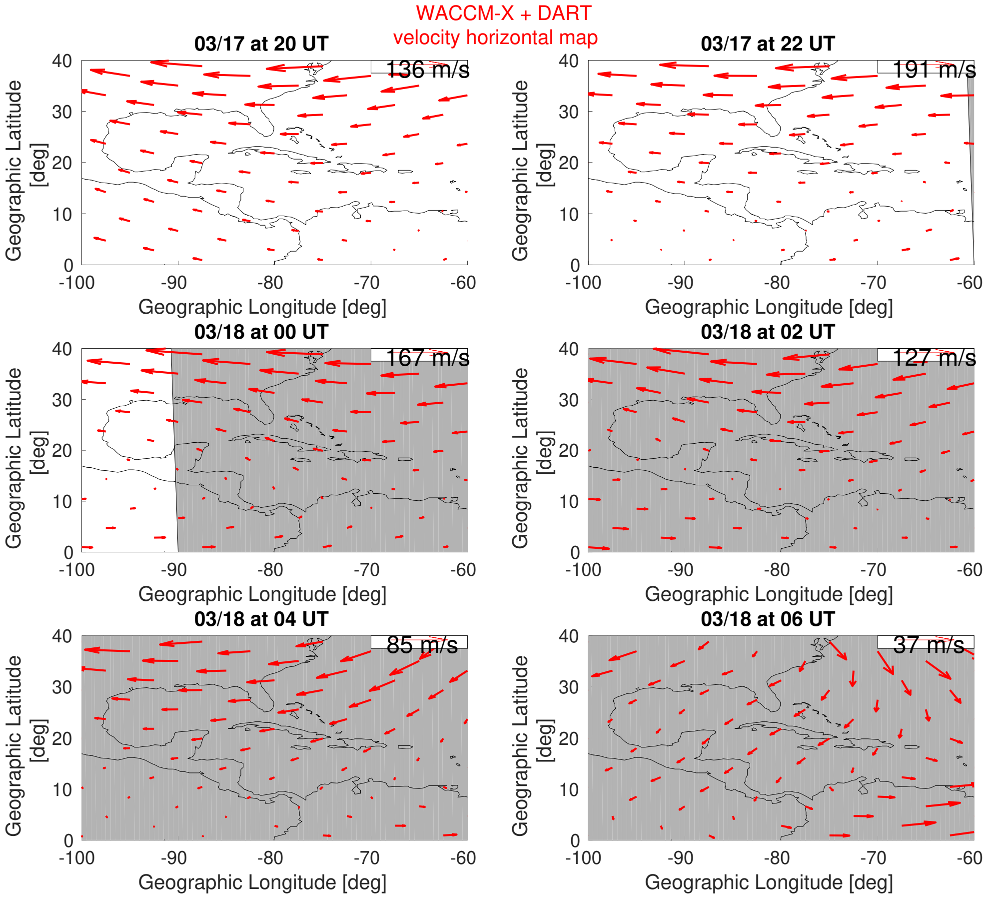

Figure 5.13. Regional maps of WACCM-X + DART ion drift vector on geographic coordinates, at 20 UT, 22 UT on March 17th, 00 UT, 02 UT, 04 UT, and 06 UT on March 18th. The speed scale is indicated in the right upper corner.

epoch. This variation arises because EMPIRE generates results 7 minutes ahead of WACCM-X + DART due to differences in time resolution. For instance, the time output from WACCM-X + DART at 2000 UT corresponds to 2007 UT in EMPIRE. Compared to Figure 5.13 produced by WACCAM-X + DART, EMPIRE agrees with the westward ion motion but yields slightly equator-ward ion motion. At 02 UT, a small circulation pattern is observed at the longitude sector of 90°W to 100°W.

The electron column density vertical profile at 20 UT, 22 UT on March 17th, 00 UT,02 UT, 04 UT and 06 UT on March 18th, are produced from WACCM-X

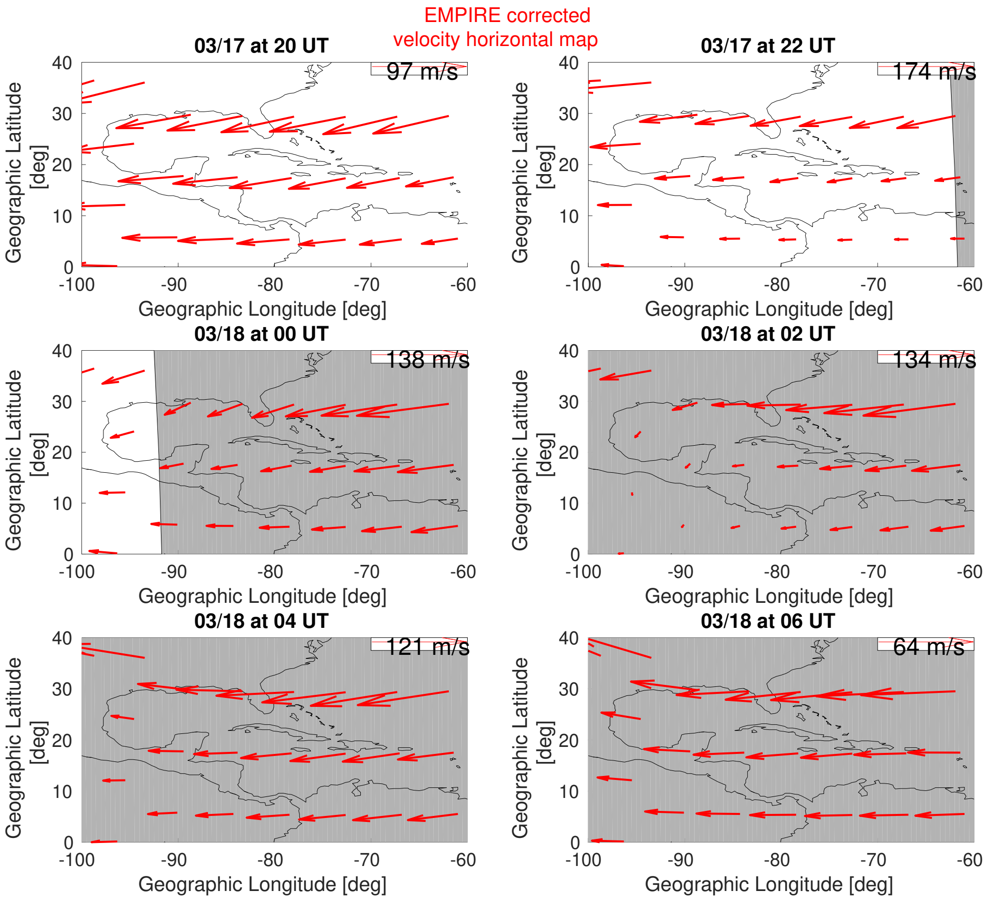

Figure 5.14. Regional maps of EMPIRE corrected ion drift vector on geographic coordinates, at 20 UT, 22 UT on March 17th, 00 UT, 02 UT, 04 UT, and 06 UT on March 18th. The speed scale is indicated in the right upper corner.

+ DART as Fig. 5.15. The vertical red solid line marks the geographic latitude of 25°N, and horizontal dashed line is labeling the geopotential height of 300 $[km]$. The color bar indicates the column density level in unit of $[m^{-3}]$. At 20 UT (16 LT), a plasma bubble is observed poleward of geographic latitude of 50°N, and the southern EIA peaks at 300 $[km]$. Also, the subplot at 20 UT implies the formation of NILE. As time progresses to 22 UT when it is before local sunset, both EIA and NILE peaks are enhanced. Equatorial anomaly is connected to NILE which indicates possible plasma transport between the NILE region and higher latitudes (or could be a plotting interpolating artifact). After local dusk (00 UT) on March 18th, the peaks

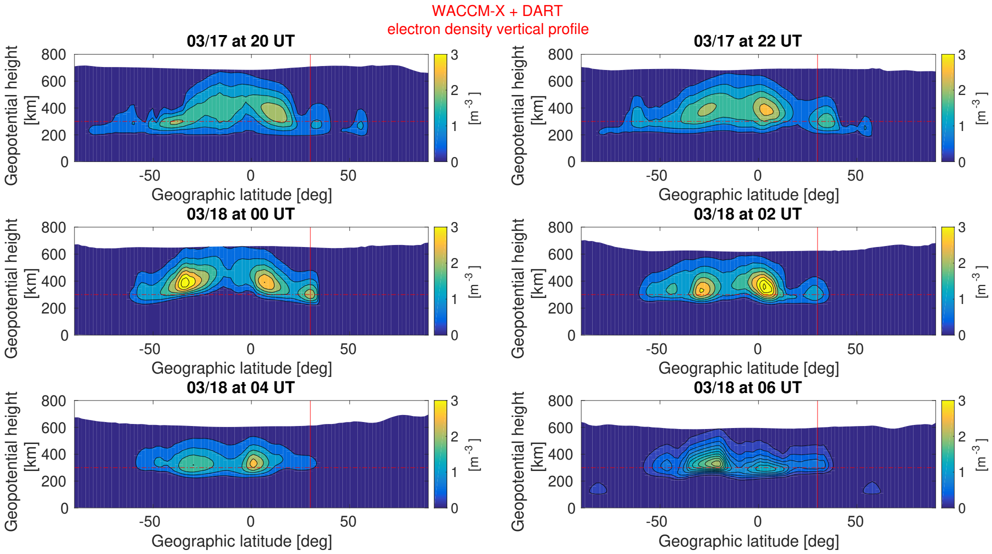

Figure 5.15. Electron density vertical profile from WACCM-X + DART plotted on potential height [km] v.s. geographic latitude [deg], at 20 UT, 22 UT on March 17th, 00 UT, 02 UT, 04 UT and 06 UT on March 18th 2015. The horizontal red dashed line represents the altitude of 300 [km], and the vertical red solid line is at geographic latitude of 25 $^\circ N$.

are further enhanced with evidence that magnetic equatorial plasma is reduced. The NILE persistently occurs until 02 UT, and dissipates afterwards.

To illustrate how the plasma near the NILE region, EMPIRE estimated ExB drifts at $80^\circ W$ geographic longitude are plotted geomagnetic coordinates in Figure 5.16 at the same time epochs as Figure 5.15. At local dusk (22 UT), the plasma uplift motion is enhanced near equatorial region, which supports the PRE theory. From 20 UT on March 17th to 00 UT on March 18th, the downward and equatorward component of drifts are observed near the NILE region (magnetic $34^\circ N$). From 00 UT to 02 UT, the plasma motion is retarded (negligible speed) near the NILE, and redistributed to higher latitudes afterwards.

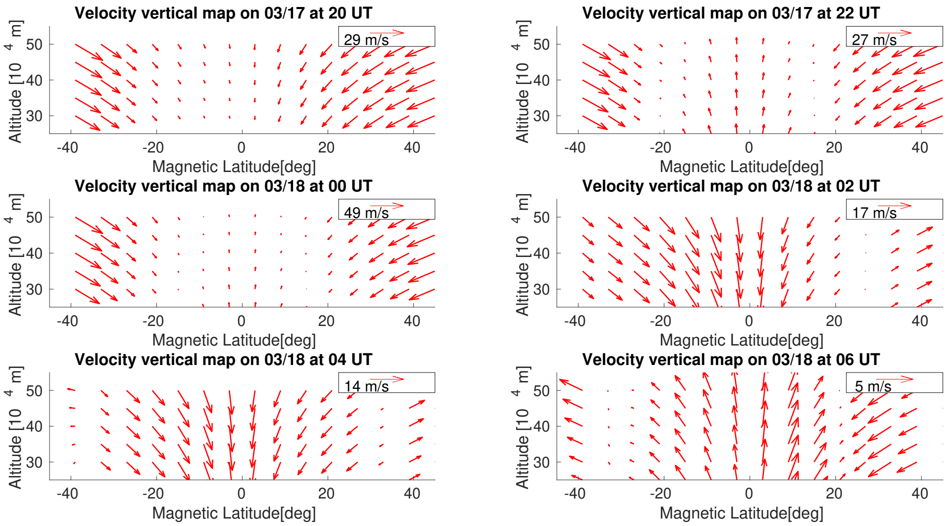

Figure 5.16. The ExB drift vertical profile plotted on geomagnetic coordinates from EMPIRE estimations at 20 UT, 22 UT on March 17th, 00 UT, 02 UT, 04 UT and 06 UT on March 18th, 2015. The speed scale is indicated in the right upper corner.

5.4 Conclusions

The vTEC global maps generated by WACCM-X + DART algorithm reveals the important characteristic of ionospheric behavior on March 2015 storm event. The maps shows variations in vTEC levels near Florida region at different Universal Time (UT) intervals, highlighting the occurrence of NILE. The zoomed-in view of vTEC ratios over the US continent shows NILE occurrence until 02 UT, and dissipates after. Additionally, a notable increase in electron density is observed at high latitudes ($60^\circ N$, $160^\circ W$) at 00 UT.

The PT theory proposes westward and pole-ward motion east of the dusk terminator. Consistent westward ion motion are shown from the ion velocity quiver plots by WACCM-X + DART and EMPIRE algorithms, but with slight differences in equator-ward motion shown by EMPIRE. A circulation pattern below the Florida region is observed, with ions initially moving westward and poleward before transitioning to an equator-ward direction.

Overall, the combination of observational data and model simulations provides valuable insights into ionospheric dynamics and the impact of algorithms like DART and EMPIRE on ion velocity predictions. They partially support PT theory for the NILE driving mechanism in that plasma moves westward. However the northward motion is not consistent with PT theory from both WACCM-X + DART and EMPIRE algorithms.

CHAPTER 6

DEVELOPMENT OF A FILTERING-SMOOTHING TECHNIQUE IN EMPIRE

Data assimilation, which can be categorized as variational, sequential or hybrid approaches, aims for optimal state estimations by integrating observational and climate model information [154]. The Kalman filter is one of the state estimation techniques primarily built in the sequential data assimilation paradigm, recursively optimizing the state calculations in a forward direction. The Kalman smoother, as an invariant of Kalman filter, originated from Rudolf E. Kálmán in 1960s to refine the state estimation incorporating “future” observations in a reverse order [155]. In the field of navigation and control systems, a Kalman smoother improves the state calculations and leverages the abilities to separate signal from noise. Also, it has been shown to be effective in various applications in Earth science, including the sub-fields of meteorology, land surface and ocean studies [156, 157, 158, 159].

In the field of data assimilation, the variational data assimilation methods are subject to high computational cost [160, 161]. Researchers have been focused on extending KS principles to develop the data assimilation algorithms. In the context of 4DVAR data assimilation algorithm, the application of a Kalman smoother improves the error statistics for estimations that does not require perfect model assumptions and minimize a 4D cost functions at the meantime [162]. A variant of the Kalman smoother (i.e. fixed-lag Kalman smoother) technique shows numerical efficiency for estimating fluxes and flux uncertainties of atmospheric trace species (i.e. carbon dioxide) [163]. [164] discussed the optimality of the Kalman filter and smoother, and its relationship with variational data assimilation. The equivalence between Kalman smoother procedures and weakly-constrained variational data assimilation algorithm in a linear system is investigated, and argued to be a solution to limit memory problem in extend Kalman filter implementations [165].

Ensemble-based data assimilation is one of the sequential techniques that is prone to sampling errors, especially in high-dimensional systems. Limited ensemble sizes can lead to sampling noise and inaccuracies in estimating the true system state, particularly in regions of low data density or high uncertainty. A study [166] of assimilating posterior stratospheric observations demonstrates the potential to improve the constraints of whole model state analysis in an Ensemble Kalman Smoother (EnKS) system. State estimation accuracy in a one-dimensional advection-diffusion model is increased by using EnKS technique [167], emphasizing the applicability of EnKS in larger-scale problems. [168] validate the EnKS techniques can be successful alternatives for solving non-linear correlation propagation in atmospheric inversion problems.

A Kalman filter is more computationally effective than an Ensemble Kalman Filter (EnKF) but highly depends on the error covariance setup for unbiased gain calculations. EMPIRE is built based on a Kalman filter, and the states of ion drifts and neutral wind are assumed to be linearly independent. Also, the background and observation error covariance are defined based on approximations, which leads to biased Kalman gain calculations in state calculations. EMPIRE applications are based on offline data sources, hence I propose to couple EMPIRE with the KS technique, and investigate the benefits through a retrospective analysis.

This chapter focuses the new concept of coupling KS to EMPIRE algorithm. Two days of August 25th and 26th are chosen and the smoothed results are compared to results from the primary setup in Sect. 3.3. The KS equations required for execution are introduced in Sect. 6.1, and experimental setup is described in Sect. 6.2.

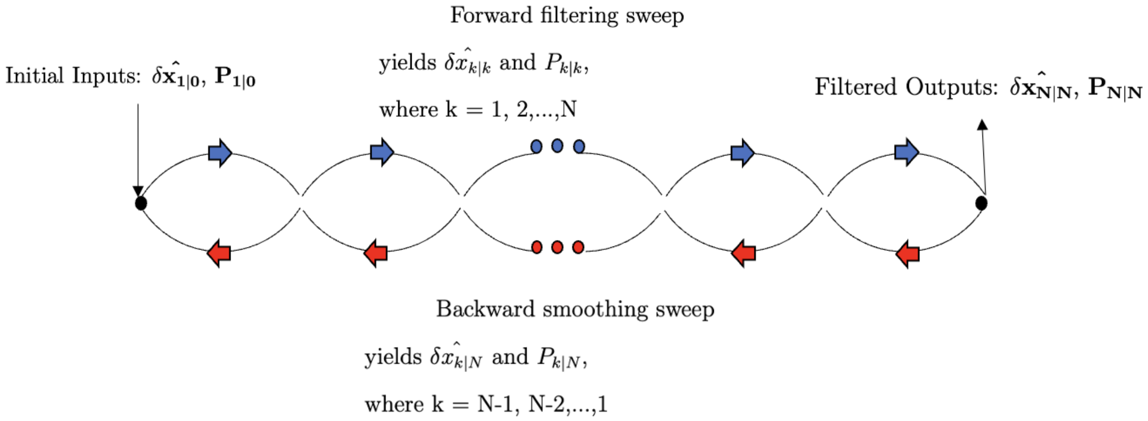

Figure 6.1. Blue and red arrows indicate the algorithm recursive orders of forward and backward respectively. $\delta\hat{\mathbf{x}}_{\mathbf{1|0}}$ and $\mathbf{P_{1|0}}$ are the state correction and covariance at initial time step. Index k indicates the time epoch number and there are N measurements available in the time frame.

6.1 Kalman smoother application in EMPIRE

Three types of KS are categorized in [33], which are (1) fixed-interval smoothing (2) fixed-point smoothing and (3) fixed-lags smoothing. A fixed-point smoother uses past, current and future data to estimate the dynamic states at a particular point in time, thus condition (1) and (3) can be treated as generalizations of the condition (2) [169].

Current EMPIRE application focuses on atmospheric driver analysis with a time range of measurements and model data available to use. The filtered state estimates are stored and can be archived for that time range. To initiate the investigations on Kalman smoother impacts to EMPIRE, the simplest fixed-interval smoothing technique is chosen for this study. Figure 6.1 describes the procedure for estimating the states for a time interval with N available measurements. The EMPIRE algorithm proceeds in forward filtering as the primary setup as summarized in Chapter 3, then sweeps backwards to refine the states and co-variances at the k-th time epoch.

Recall the Kalman filter setup defined as Eq. (2.26) in Chapter 2.1, the observation update model is:

$$\mathbf{z_k} = \mathbf{H_k}\delta\mathbf{x_k} + \epsilon_\mathbf{k}, \epsilon_\mathbf{k} \sim \mathcal{N}(\mathbf{0},\, \mathbf{R_k})$$

The dynamic process previously defined as Eq. (2.27) is:

$$\delta\mathbf{x_{k+1}} = \mathbf{\Phi_k}\delta\mathbf{x_k} + \eta_\mathbf{k}, \eta_\mathbf{k} \sim \mathcal{N}(\mathbf{0},\, \mathbf{Q_k})$$

The backward-sweeping equations are built on the states and covariance matrices from the Kalman filter. At the k-th step for the smoother, the posterior state and covariance are denoted as $\delta\mathbf{\hat{x}_{k|k}}$ $\mathbf{P_{k|k}}$, and prior state and covariance are $\delta\mathbf{\hat{x}_{k+1|k}}, \mathbf{P_{k+1|k}}$. The smoothing gain $\mathbf{A_k}$ is formulated in Eq. (6.1)

$$\mathbf{A_k} = \mathbf{P_k^+}\mathbf{\Phi_k^T}(\mathbf{P_{k+1}^-})^{-\mathbf{1}} \tag{6.1}$$

The state vector given all measurement information $\delta\mathbf{\hat{x}_{k|N}}$ is given by Eq. (6.2)

$$\delta\mathbf{\hat{x}_{k|N}} = \delta\mathbf{\hat{x}_k^+} + \mathbf{A_k}\left[\delta\mathbf{\hat{x}_{k+1|N}} - \delta\mathbf{\hat{x}_{k+1}^-}\right] \tag{6.2}$$

The error covariance matrix for the smoothed estimates can be obtained by the recursive equation:

$$\mathbf{P_{k|N}} = \mathbf{P_k^+} + \mathbf{A_k}\left[\mathbf{P_{k+1|N}} - \mathbf{P_{k+1}^-}\right]\mathbf{A_k^T}$$

where the refined state vector $\delta\mathbf{\hat{x}_{k|N}}$ and co-variance $\mathbf{P_{k|N}}$ from the backward sweeping processes are updated at each smoothing step.

Figure 6.2 shows how the Kalman filter and smoother is coupled to the EMPIRE algorithm. After the state and covariances are obtained from the Kalman filter for a selected time window, the smoother is implemented in backward order to refine the state and covariance estimations at time steps of $N-1, N-2, ...1$, denoted as $\delta\mathbf{\hat{x}_{N-1|N}}$, $\delta\mathbf{\hat{x}_{N-2|N}}$, ...$\delta\mathbf{\hat{x}_{1|N}}$ for state vectors, and $\mathbf{P_{N-1|N}}$, $\mathbf{P_{N-2|N}}$,...$\mathbf{P_{1|N}}$ for state covariance matrices.

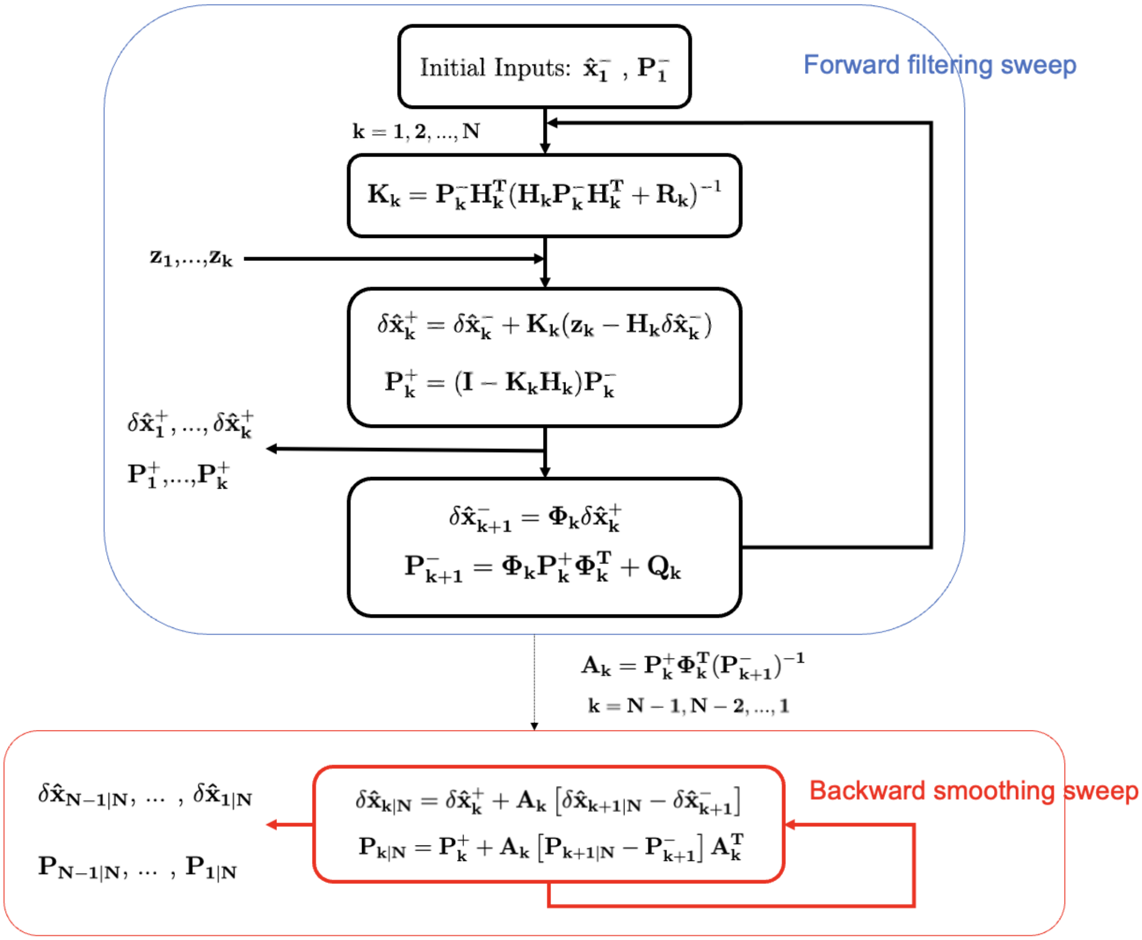

Figure 6.2. Filter-smoother coupled technique setup in EMPIRE algorithm. The forward filter sweep block is same as the Kalman filter flowchart shown in Figure 2.1, and the variable descriptions can be referred to in the caption of Figure 2.1. The smoother gain is denoted as $\mathbf{A_k}$, and $k = N-1, N-2, ...1$ indicates the recursive direction is backward. At k-th time epoch, the smoothed state variables $\delta\mathbf{\hat{x}_{k|N}}$ and covariance $\mathbf{P_{k|N}}$ are calculated based on the smoother gain, prior and posterior state vectors and covariance matrices estimated from the Kalman filter.

6.2 Experimental setup

The goal is to explore the potential of the Kalman smoother in EMPIRE. To illustrate the global impacts, a similar experimental setup using synthetic data is adopted from Chapter 3.2: the driving ionospheric variables obtained from SAMI3 and SAMI3's driven models (Weimer, MSIS and HWM14) are treated as synthetic truth, and IRI is the background model. The same two days of 25-26 August 2018 are selected for this study.

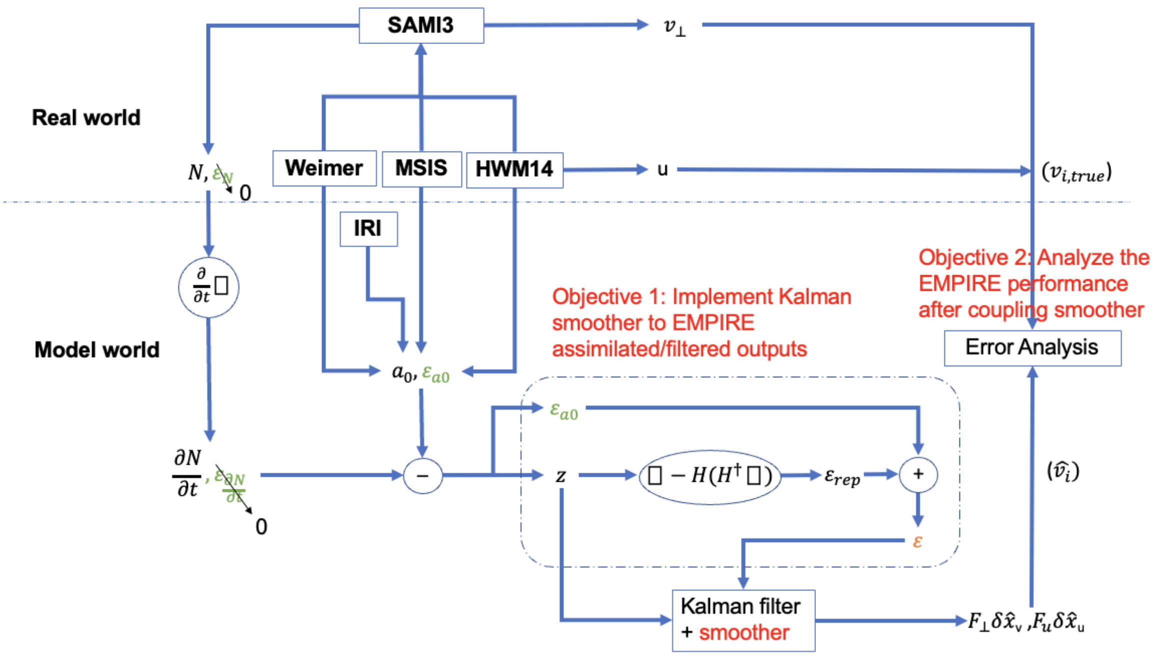

Figure 6.3. Modified from Figure 3.3. The background model inputs and measurements are same as the experiment setup in Chapter 3.2. The red text indicates EMPIRE new modification by coupling a smoother. Two study objectives is also highlighted in red.

The experiment flowchart is shown in Figure 6.3, which indicates the objectives in red are: 1) Implement a Kalman smoother to EMPIRE assimilated/filtered outputs, 2) Analyze EMPIRE performance after coupling the smoother. The driver of ion drift will be assessed by comparing to SAMI3 data as synthetic truth.

6.3 Results

After EMPIRE is coupled with Kalman smoother, Figure 6.4 shows the zonally averaged difference between SAMI3 and EMPIRE correction of ion drifts in field-perpendicular zonal and meridional directions over time. Compared to Figure 3.4, which shows EMPIRE results without a smoother implemented, the zonal mean error of ion drifts at high latitudes is reduced significantly.

During the quiet time from 14 UT to 24 UT on the August 25th, the zonal mean error in the field-perpendicular zonal direction in the northern hemisphere high latitudes exceeds +200 $[m/s]$ in Figure 3.4. The smoothed results indicates the zonal mean error is decreased by approximately 150-200 $[m/s]$. As for storm time, the large negative mean errors at northern high latitudes were observed in Figure 3.4, while smoothed products shows reduced magnitude in zonal mean errors. At SH high latitudes, the smoothed results yield zonally averaged mean errors within ± 50 $[m/s]$, which is much lower than results shown in Figure 3.4.

Figure 6.5 shows the time-averaged and latitude-dependent ion drift relative error on a log base-10 scale in the (a) field-perpendicular zonal direction and (b) field-perpendicular meridional direction. Figure 6.5(c) and (d) plot the time-averaged error $\mu_{\epsilon \mathbf{vi}}(\theta)$ and standard deviation $\sigma_{\epsilon \mathbf{vi}}(\theta)$ between SAMI3 and EMPIRE corrected ion drifts in perp-zonal and perp meridional directions, respectively. Figure 6.5(a) and (b) indicate relative error does not change by comparing to Figure 3.4 (a) and (b).

From Figure 6.5(c), calculations of $\mu_{\epsilon \mathbf{vi}}(\theta)$ and $\sigma_{\epsilon \mathbf{vi}}(\theta)$ in perp-zonal direction at high latitudes for both hemispheres are decreased, indicating that the zonal mean errors are less spread across time. Figure 6.5(d) also present reduced $\mu_{\epsilon \mathbf{vi}}(\theta)$ and $\sigma_{\epsilon \mathbf{vi}}(\theta)$ in the perp-meridional direction.

Zonally averaged difference $\bar{\epsilon}_{vi}(\theta;t)$ [SAMI3 - EMPIRE]

(a) Perp-zonal $\bar{\epsilon}_{vi}(\theta;t)$

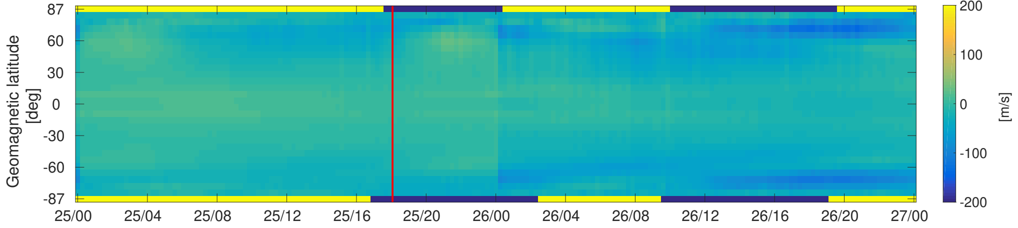

(b) Perp-meridional $\bar{\epsilon}_{vi}(\theta;t)$

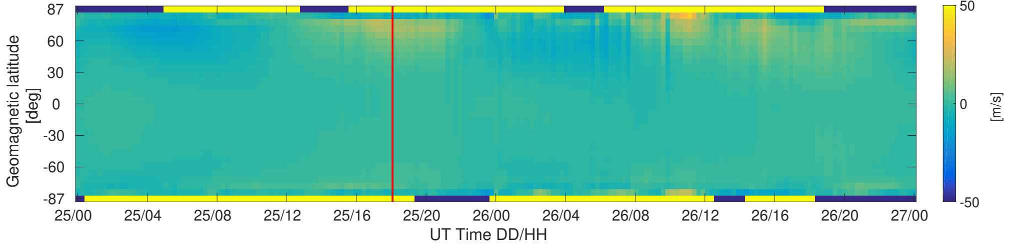

Figure 6.4. Zonally averaged differences between SAMI3 and EMPIRE correction of ion drifts processed by Kalman smoother, in the (a) field-perpendicular zonal and (b) field-perpendicular meridional directions. The red vertical lines separates the quiet and storm periods: 00 UT and 18 UT August 25th is the quiet period, and 18 UT August 25th to 00 UT August 27th is the storm period.

6.4 Conclusions

A synthetic study is conducted for exploring the impacts from coupling the Kalman smoother to the EMPIRE algorithm in correcting ion drifts, and show significant improvements on error residuals at high latitudes. To compare EMPIRE performance before and after the smoothing process, data inputs and error metrics are same as contribution (1) in Chapter 3, and same period from August 25th to 26th 2018 are selected.

The zonal mean errors in the field-perpendicular zonal direction at northern high latitudes are bounded within a range of ± 100 $[m/s]$ for storm time (00 UT to 18 UT on August 25th), and ± 50 $[m/s]$ for quiet time (18 UT on August 25th to 00 UT on August 27th). For the field-perpendicular meridional direction, the zonal mean errors at high latitudes are also decreased to below the magnitude of 50 $[m/s]$. The time-averaged error sigmas are also reduced to be within ± 50 $[m/s]$ for

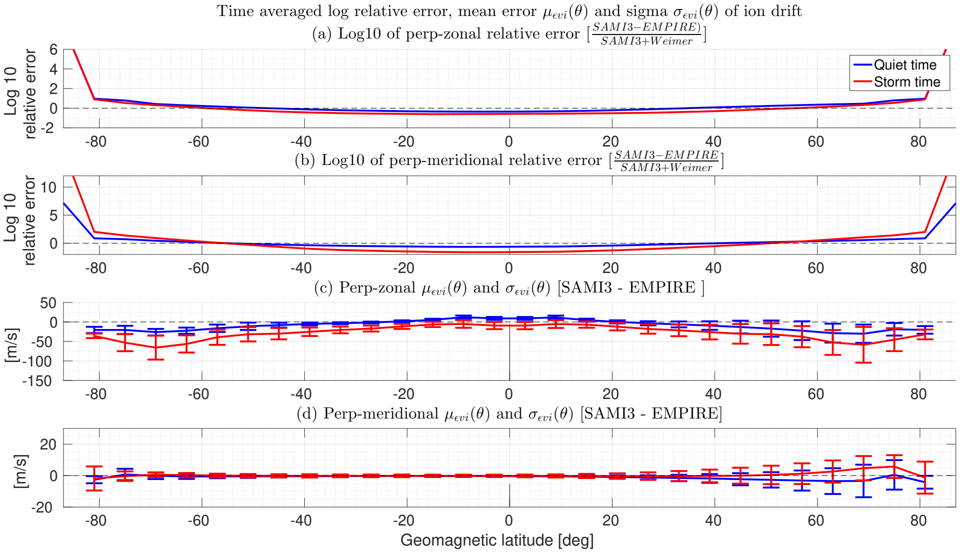

Figure 6.5. The time averaged ion drift relative errors on a log base-10 scale versus geomagnetic latitude are presented in (a) field-perpendicular zonal direction and (b) field-perpendicular meridional direction, from EMPIRE newly coupled smoother. The horizontal dashed line in (a) and (b) indicate that the relative error is 100%. The time-averaged error $\mu_{\mathbf{\epsilon vi}}(\theta)$ and standard deviation $\sigma_{\mathbf{\epsilon vi}}(\theta)$ between SAMI3 and EMPIRE corrected ion drifts versus magnetic latitude are plotted in the field-perpendicular (c) zonal and (d) meridional directions. The horizontal dashed line indicates 0 velocity components. The Figure (c) inset plot zooms in on the mean error at the low-to-mid latitudes. For all of the subplots, the vertical black line is the 0° latitude line. Quiet and storm time error statistics are plotted with blue and red lines, respectively.

the field-perpendicular zonal direction, and ± 20 $[m/s]$ for the field-perpendicular meridional direction. The time-averaged relative errors on a log-10 scale do not differ much from the results in Section 3.3, indicating that at latitudinal-dependent bias at high latitudes still persists in EMPIRE.

Categorized as a retrospective objective analysis, the Kalman smoother has been studied for the purpose of improving analysis qualities in data assimilation [169]. The implementation in this work of a Kalman smoother in EMPIRE also indicates the potential of using a Kalman smoother to refine ionospheric models and improve the accuracy of ion drift predictions, which highlights the importance of continued research and development in ionospheric modeling and prediction techniques.

CHAPTER 7

CONCLUSIONS

This dissertation described the developments in a data assimilation (DA) algorithm known as EMPIRE, and DA applications for investigating a storm-related phenomenon, the NILE. EMPIRE primarily ingests the electron densities from other DA algorithms, combines them with background model information, and yields optimized estimates of ion drifts and neutral wind in a global or regional map via Kalman filtering. The major contributions in this thesis include: (1) reconstructing the representation error as an error source input to the Kalman filter in EMPIRE; (2) augmenting observations with SuperDARN ion drift measurements to be assimilated into EMPIRE and validating with MHISR measurements; (3) exploring the NILE driving mechanism and validating the proposed mechanism with independent outputs from two DA algorithms, the WACCM-X + DART and EMPIRE.

7.1 Summary and Discussion

This dissertation is motivated by investigation of a storm-related phenomenon: NILE, which refers to persistent electron content enhancement at the U.S. Florida region during local nighttime. Neutral wind can be a driving factor of NILE and was analyzed in [31]. [21] explained the plasma motion might be due to storm-time electric fields, and proposed the Polarization Terminator (PT) and Pre-reversal Enhancement (PRE) as possible supporting theories describing the NILE. Before investigating NILE phenomenon, it is essential to comprehensively understand the limitations and advantages of the data assimilation tool used in the study, which is EMPIRE.

The first and second contributions are related with data assimilation algorithm developments. The first contribution of Chapter 3 reconstructs the representation error in EMPIRE and analyzes the performance on a global scale. SAMI3 is utilized as a synthetic truth source of electron density and ion drifts. EMPIRE runs on two days of August 25th and 26th on 2018 are investigated, and inputs to EMPIRE are self-consistent with SAMI3. The EMPIRE outputs of ion drifts in field-perpendicular zonal and meridional directions are compared with the synthetic truth of ion drift corresponding components from SAMI3. The error metrics indicate latitude-dependent error distributions. The results show the northern hemisphere yields larger zonally averaged mean errors over the analysis period, and the relative error exceeds 100 % at high latitudes. Also, the error sigma during storm time is generally greater than the quiet time, which indicates larger uncertainties are expected during storm time.

The second contribution, of Chapter 4, introduces a new method to improve EMPIRE's capabilities by integrating SuperDARN ion drift measurements. This method involves creating new observation matrices within the Kalman filter observation update procedure. The analysis period is selected from 16-18 March 2015, with peak geomagnetic activity at 22 UT on March 17th. The study compares a primary case that only ingests SAMI3/IDA4D electron densities with the augmented cases that assimilate SuperDARN data in fit and grid data forms, respectively. EMPIRE's estimations and background model calculations for ion drifts are validated using MHISR measurements at two locations for field-perpendicular zonal and meridional directions. Additionally, two independent SuperDARN gridded ion drift datasets, which are not integrated into EMPIRE, are used as other validation sources. Overall, this investigation shows EMPIRE's performance improves only slightly due to ingestion of high latitude drifts through the incorporation of richer spatial information from fit data, leading to slightly reduced residual deviations.

The scientific principle investigation of a storm-related phenomenon of NILE is conducted on the third contribution of Chapter 5. In order to quantify an enhancement level compared to the background total electron content, the TEC ratio regional maps are constructed for 4 moderate to severe storm events. The case studies show that the geomagnetic activity levels are associated with NILE strength, and plasma is transported westward and poleward at the enhancement region. We investigated the NILE driving mechanism and tested the proposed theory [21] that the NILE formation is due to PT and PRE that cause northwest ion motion. To gain more insight on ion transport, EMPIRE and WACCM-X + DART are each implemented independently for the storm case of 17 March 2015. The westward motion during Florida local nighttime from both algorithms agree with PT theory, but the poleward motion is not observed either from WACCM-X + DART or EMPIRE results. A circulation pattern below Florida's latitude after dusk terminator is detected in WACCM-X + DART, and EMPIRE shows agreement with this at one time epoch. At local post-midnight, EMPIRE continues to yield westward motion, which is different from the equator-ward motion in WACCM-X + DART.

Motivated by the inconsistency between EMPIRE and WACCM-X + DART estimations for NILE study, a causal filtering technique is proposed to refine the states with all information available (both past and future). Chapter 6 adopted the Kalman smoothing technique in EMPIRE proposed to refine the state calculations. To assess the global performance after coupling the smoother, the days that were investigated in Chapter 3 are chosen for the evaluation time periods. The same inputs and error metrics in Chapter 3 are used in this study to better understand the impacts of the new filter/smoother coupled technique in EMPIRE. From the filtered and smoothed results, EMPIRE shows improvements on high-latitude ion drift calculations, indicated by reduced zonal mean errors and time-averaged error sigmas.

7.2 Future work

Chapter 3 is the synthetic study of representation error in EMPIRE with only Kalman filter, and yields excessive errors at high-latitudes. EMPIRE utilizes spherical harmonics expansion as the fitting functions for electric potential driver, formulated by assuming the constant electric potential value along with a magnetic field-line for a dipole. However, the defined L-shell values at high-latitudes based on the assumptions yield larger variations than the actual earth model. The Active Magnetosphere and Planetary Electrodynamics Response Experiment (AMPERE) utilizes the spherical cap harmonic analysis (SCHA) to derive fitting coefficients for magnetic field perturbations due to Birkeland (field-aligned) currents from Iridium satellite magnetometer data [170]. One direction for EMPIRE work can be to develop a high-latitude mapping function, using spherical cap harmonics [171] to separate the coefficient fitting for low-to-mid and high latitudes. Additionally, Chapter 6 indicates that the smoother can reduce the high-latitude errors. In future work, runs with ingesting real data should be conducted to assess the performance of the smoother.

Chapter 4 investigated the algorithm capabilities of ingesting additional ion drift measurements and validate with other independent data sources. However, the posterior state covariance from EMPIRE implementations (indicated by the error bars plotted on Figure 4.7 and Figure 4.8) does not adequately represent for the truth measurements. Posterior state covariance is obtained based on the Kalman gain calculation, observation mapping matrix and prior state covariance. Given the linear independent relationship between observations, and between drivers of neutral wind and electric potential, the correlation information is missing in the Kalman gain calculations. Besides, the fitting function can be another error source that attributed to the Kalman gain calculations. Further investigations need to be performed to improve the error statistics input to the algorithm.

Chapter 5 only shows the WACCM-X + DART and EMPIRE implementation results on March 2015, to illustrate the NILE plasma motion. One case can be illustrative but is not enough for definitive scientific conclusions. Thus other storm cases should also be investigated for dependency on other possible factors (i.e. geomagnetic levels, seasons, geographic locations). Also, the neutral wind's impacts as a NILE were investigated in [31], but the combined effects of both winds and fields can reveal more realistic information about NILE.

APPENDIX A

CORRECTIONS TO FIRST AND SECOND DERIVATIVES OF ASSOCIATED LEGENDRE POLYNOMIAL FUNCTIONS

A.1 Derivation of Associated Legendre Function's First Derivative Recurrence Relation

The goal of the derivation is to show that, unlike Miladinovich et al. (2020)'s Eq. (A13), which says:

$$\frac{dP_l^m}{du} = \frac{muP_l^m - (l+m)(l-m+1)(1-u^2)^{1/2}P_l^{m-1}}{1-u^2} \textbf{ INCORRECT}$$

and unlike A&S 9th edition's Eq. 8.5.2,

$$(u^2-1)\frac{dP_l^m}{du} = (l+m)(l-m+1)(u^2-1)^{1/2}P_l^{m-1} - muP_l^m \textbf{ NOT APPLICABLE}$$

which applies to complex values of u, the recurrence relation derivative for real-valued u and non-negative integer l, m is:

$$(u^2-1)\frac{dP_l^m}{du} = -(l+m)(l-m+1)(1-u^2)^{1/2}P_l^{m-1} - muP_l^m \textbf{ CORRECT} \quad (A.1)$$

To show Eq. (A.1), begin with the definition of the associated Legendre functions P_l^m for $-\mathrm{l} \le m \le \mathrm{l}$ including the Condon-Shortly phase $(-1)^m$ but not the normalization factors is defined by Eq. (23) of Miladinovich et al., 2020, and reprinted here:

$$P_l^m = \frac{(-1)^m}{2^l l!}(1-u^2)^{m/2}(\frac{d}{du})^{(l+m)}(u^2-1)^l \quad (A.2)$$

Taking the derivative of Eq. (A.2) with respect to u:

$$\begin{aligned}\frac{dP_l^m}{du} &= \frac{(-1)^m}{2^l l!}(\frac{d}{du})^{l+m}(u^2-1)^l\frac{d\left((1-u^2)^{m/2}\right)}{du} + \frac{(-1)^m}{2^l l!}(1-u^2)^{m/2}(\frac{d}{du})^{(l+m+1)}(u^2-1)^l \\ &= -\frac{mu}{1-u^2}P_l^m - (1-u^2)^{1/2}P_l^{m+1} \quad (A.3)\end{aligned}$$

where

$$P_l^{m+1} = \frac{(-1)^{m+1}}{2^l l!}(1-u^2)^{\frac{m+1}{2}} \frac{d}{du}^{(l+m+1)}(u^2-1)^l \tag{A.4}$$

Separately, substituting degree of l+1 into Eq. (A.2):

$$P_{l+1}^m = \frac{(-1)^m}{2^{l+1}(l+1)!}(1-u^2)^{m/2} \underbrace{(\frac{d}{du})^{(l+m+1)}(u^2-1)^{l+1}}_{Term1} \tag{A.5}$$

To expand $Term1$ in Eq. A.5, there are two options: to write it in terms of $[P_l^m,\, P_l^{m-1}]$ or write it in terms of $[P_l^{m+1},\, P_l^m,\, P_l^{m-1}]$.

A.1.1 Mathematical equations used in the derivation.

Before we expand $Term1$, the binomial coefficient on k-th derivatives with respect to u on the product of differentiable functions f and g dependent on u are expressed by the general Leibniz rule as Eq. (5.52) in [172]:

$$\begin{aligned} \frac{d}{du}^{(k)}(fg) &= \sum_{r=0}^{k} \binom{k}{r} f^{(r)} g^{(k-r)} \\ &= \binom{k}{0} f^{(0)} g^{(k)} + \binom{k}{1} f^{(1)} g^{(k-1)} + \binom{k}{2} f^{(2)} g^{(k-2)} + ... + \binom{k}{k} f^{(k)} g^{(0)} \end{aligned} \tag{A.6}$$

where r is the summation variable, f, g are the functions of independent variable u, and where $\binom{a}{b} \triangleq \frac{a!}{b!(a-b)!}$, and the bracketed superscripts indicate the ()-th derivative with respect to u.

A.1.2 Option 1: Express $Term1$ as a combination of $[P_l^m$ & $P_l^{m-1}]$.

Using the binomial differentiation Eq. (A.6),

$$\begin{aligned}
Term1 &= \frac{d}{du}^{(l+m+1)}(u^2-1)^{l+1} \\
&= \frac{d}{du}^{(l+m)}\left[\underbrace{2u(l+1)}_{f}\underbrace{(u^2-1)^l}_{g}\right] \\
&= \sum_{r=0}^{l+m}\binom{l+m}{r}f^{(r)}g^{(l+m-r)} \\
&= \binom{l+m}{0}f^{(0)}g^{(l+m)} + \binom{l+m}{1}f^{(1)}g^{(l+m-1)} \\
&+ \underbrace{\binom{l+m}{2}f^{(2)}g^{(l+m-2)} + \ldots + \binom{l+m}{l+m}f^{(l+m)}g^{(0)}}_{0} \\
&= 2u(l+1)\frac{d}{du}^{(l+m)}(u^2-1)^l + \frac{(l+m)!}{(l+m-1)!}\underbrace{2(l+1)}_{f^{(1)}}\underbrace{\frac{d}{du}^{(l+m-1)}(u^2-1)^l}_{g^{(l+m-1)}} \qquad \text{(A.8)}
\end{aligned}$$

Multiplying both sides of Eq. (A.8) by $\frac{(-1)^m}{2^{l+1}(l+1)!}(1-u^2)^{m/2}$, so then Eq. (A.5) can be rewritten as

$$P_{l+1}^m = uP_l^m - (l+m)(1-u^2)^{1/2}P_l^{m-1} \qquad \text{(A.9)}$$

where

$$P_l^{m-1} = \frac{(-1)^{m-1}}{2^l l!}(1-x^2)^{(m-1)/2}\frac{d}{du}^{(l+m-1)}(u^2-1)^l \qquad \text{(A.10)}$$

Eq. (A.9) is the form for Option 1 for Eq. (A.5).

A.1.3 Option 2: Expand $Term1$ in terms of $[P_l^{m+1}$, P_l^m & $P_l^{m-1}]$.

Recall that P_l^{m+1} is given in Eq. (A.4), P_l^m in Eq. (A.2), and P_l^{m-1} in Eq. (A.10). Begin with $Term1$:

$$
\begin{aligned}
Term1 &= \frac{d}{du}^{(l+m+1)}(u^2-1)^{l+1} \\
&= \frac{d}{du}^{(l+m+1)}\left[\underbrace{(u^2-1)}_{f}\underbrace{(u^2-1)^l}_{g}\right] \\
&= \sum_{r=0}^{l+m+1}\binom{l+m+1}{r} f^{(r)} g^{(l+m+1-r)} \\
&= 1\binom{l+m+1}{0} f^{(0)} g^{(l+m+1)} + \binom{l+m+1}{1} f^{(1)} g^{l+m} \\
&+ \binom{l+m+1}{2} f^{(2)} g^{(l+m-1)} \\
&= \underbrace{(u^2-1)\frac{d}{du}^{(l+m+1)}(u^2-1)^l}_{term2} + \underbrace{\frac{(l+m+1)!}{(l+m)!}2u\frac{d}{du}^{(l+m)}(u^2-1)^l}_{term3} \\
&\quad + \underbrace{\frac{2(l+m+1)!}{2!(l+m-1)!}\frac{d}{du}^{(l+m-1)}(u^2-1)^l}_{term4} \\
&= \underbrace{(u^2-1)\frac{d}{du}^{(l+m+1)}(u^2-1)^l}_{term2} + \underbrace{2u(l+m+1)\frac{d}{du}^{(l+m)}(u^2-1)^l}_{term3} \\
&\quad + \underbrace{(l+m+1)(l+m)\frac{d}{du}^{(l+m-1)}(u^2-1)^l}_{term4} \qquad \text{(A.11)}
\end{aligned}
$$

Multiply both sides of Eq. (A.11) by $\frac{(-1)^m}{2^{l+1}(l+1)!}(1-u^2)^{m/2}$, which is the factor preceding $Term1$ in Eq. (A.5). This will give the $term2$ expansion as:

$$
\begin{aligned}
&\frac{(-1)^m}{2^{l+1}(l+1)!}(1-u^2)^{m/2}(term2) \\
&= \frac{(-1)^m}{2^{(l+1)}(l+1)!}(1-u^2)^{m/2}(u^2-1)\frac{d}{du}^{(l+m+1)}(u^2-1)^l \\
&= -(1-u^2)^{-1/2}\frac{u^2-1}{2(l+1)}\underbrace{\frac{(-1)^{m+1}}{2^l l!}(1-u^2)^{(m+1)/2}\frac{d}{du}^{(l+m+1)}(u^2-1)^l}_{P_l^{m+1}}
\end{aligned}
$$

$$= \frac{(1-u^2)^{1/2}}{2(l+1)} P_l^{m+1}$$

The *term*3 expansion is:

$$\begin{aligned}
&\frac{(-1)^m}{2^{l+1}(l+1)!}(1-u^2)^{m/2}(term3)\\
&= \frac{(-1)^m}{2^{(l+1)}(l+1)!}(1-u^2)^{m/2} 2u(l+m+1)\frac{d}{du}^{(l+m)}(u^2-1)^l\\
&= \frac{u(l+m+1)}{l+1}\underbrace{\frac{(-1)^m}{2^l(l)!}(1-u^2)^{m/2}\frac{d}{du}^{(l+m)}(u^2-1)^l}_{P_l^m}\\
&= \frac{u(l+m+1)}{l+1} P_l^m
\end{aligned}$$

The *term*4 expansion is:

$$\begin{aligned}
&\frac{(-1)^m}{2^{l+1}(l+1)!}(1-u^2)^{m/2}(term4)\\
&= (l+m+1)(l+m)\frac{(-1)^m}{2^{l+1}(l+1)!}(1-u^2)^{m/2}\frac{d}{du}^{(l+m-1)}(u^2-1)^l\\
&= \frac{-(1-u^2)^{1/2}(l+m)(l+m+1)}{2(l+1)}\underbrace{\frac{(-1)^{m-1}}{2^l l!}(1-u^2)^{(m-1)/2}\frac{d}{du}^{(l+m-1)}(u^2-1)^l}_{P_l^{m-1}}\\
&= \frac{-(1-u^2)^{1/2}(l+m)(l+m+1)}{2(l+1)} P_l^{m-1}
\end{aligned}$$

Combining the expansions of term2, term3 and term4, then P_{l+1}^m of Eq. (A.5) can be written via Option 2 as:

$$P_{l+1}^m = \frac{(1-u^2)^{1/2}}{2(l+1)} P_l^{m+1} + \frac{u(l+m+1)}{l+1} P_l^m - \frac{(1-u^2)^{1/2}(l+m)(l+m+1)}{2(l+1)} P_l^{m-1} \tag{A.18}$$

A.1.4 Final derivation of the recurrence relation.

Here we will use the Option 1 form, Eq. (A.9) to complete the recurrence relation for the derivative. Multiplying Eq. (A.18) through by $2(l{+}1)$, subtracting the P_l^m term from both sides, and plugging in Eq. (A.9) to eliminate P_{l+1}^m:

$$2(l+1)\underbrace{\left[uP_l^m-(l+m)(1-u^2)^{1/2}P_l^{m-1}\right]}_{P_{l+1}^m}-2u(l+m+1)P_l^m$$
$$=(1-u^2)^{1/2}\left[P_l^{m+1}-(l+m)(l+m+1)P_l^{m-1}\right] \tag{A.19}$$

Reorganizing Eq. (A.19) to gather P_l^m terms:

$$2muP_l^m=-(l-m+1)(l+m)(1-u^2)^{1/2}P_l^{m-1}-(1-u^2)^{1/2}P_l^{m+1} \tag{A.20}$$

Recall the derivative of P_l^m with respect to u in Eq. (A.3):

$$\frac{dP_l^m}{du}=-\frac{mu}{1-u^2}P_l^m-(1-u^2)^{-1/2}P_l^{m+1}$$

Rearranging Eq. (A.3) to move P_l^{m+1} to the left side of equation and other terms to the right side:

$$P_l^{m+1}=-(1-u^2)^{1/2}\frac{dP_l^m}{du}-mu(1-u^2)^{-1/2}P_l^m \tag{A.21}$$

Plugging (A.21) into (A.20), the final recurrence relation is derived as:

$$\boxed{(u^2-1)\tfrac{dP_l^m}{du}=-(l+m)(l-m+1)(1-u^2)^{1/2}P_l^{m-1}-muP_l^m} \tag{A.22}$$

A.1.5 Examples plugged in.

1. Derivative of P_1^1

   To demonstrate (A.22), we first choose an associated Legendre function with

$l = 1, m = 1$

$$\begin{aligned} P_1^1 &= -(1-u^2)^{1/2}\frac{d}{d^2u}^{2}(u^2-1) \\ &= -(1-u^2)^{1/2} \\ P_1^0 &= u \end{aligned}$$

plugging P_1^1 and P_1^0 into the right side of Eq. (A.22) and organizing the terms:

$$\frac{dP_1^1}{du} = u(1-u^2)^{-1/2}$$

Which is equivalent to the result of directly taking derivative of P_1^1 with respect to x:

$$\frac{dP_1^1}{du} = u(1-u^2)^{-1/2}$$

2. Derivative of P_2^2

   To check (A.22) again, we choose an associated Legendre function with $l = 2, m = 2$

$$P_2^2 = 3(1-u^2)P_2^1 = -3u(1-u^2)^{1/2} \tag{A.24}$$

   Plugging P_2^2 and P_2^1 into the right side of Eq. (A.22) and organizing the terms:

$$\frac{dP_2^2}{du} = -6u$$

   which is equivalent to the result of directly taking derivative of P_2^2 with respect to u:

$$\frac{dP_2^2}{du} = -6u$$

3. Derivative of P_2^1 Start by noting that P_2^1 was given in Eq. (A.24), and P_2^0 is:

$$\begin{aligned} P_2^0 &= \frac{(-1)^0}{2^2(2!)}(1)\frac{d^2}{du^2}(u^2-1)^2 \\ &= \frac{1}{2}(3u^2-1) \end{aligned}$$

To test whether $(u^2-1)\frac{dP_l^m}{du} = -(l+m)(l-m+1)(1-u^2)^{1/2}P_l^{m-1} - muP_l^m$, compute the lefthand side (LHS) by direct differentiation:

$$\begin{aligned} (u^2-1)\frac{dP_l^m}{du} &= (u^2-1)\frac{d}{du}[-3u(1-u^2)^{1/2}] \\ &= (u^2-1)[-3(1-u^2)^{1/2}+3u^2(1-u^2)^{-1/2}] \\ &= 3(1-u^2)^{3/2}-3u^2(1-u^2)^{1/2} \\ &= 3(1-u^2)^{1/2}[(1-u^2)-u^2] \\ &= 3(1-u^2)^{1/2}(1-2u^2) \end{aligned}$$

For the righthand side (RHS) we plug in:

$$\begin{aligned} & -(l+m)(l-m+1)(1-u^2)^{1/2}P_l^{m-1} - muP_l^m \\ = \; & -(2+1)(2-1+1)(1-u^2)^{1/2}[\frac{1}{2}(3u^2-1)] - 1u(-3u)(1-u^2)^{1/2} \\ = \; & -3(1-u^2)^{1/2}(3u^2-1)+3u^2(1-u^2)^{1/2} \\ = \; & 3(1-u^2)^{1/2}[-3u^2+1+u^2] \\ = \; & 3(1-u^2)^{1/2}(1-2u^2) \end{aligned}$$

So the LHS = RHS for the derivative of P_2^1 as well.

A.1.6 Alternative derivation based on NIST Handbook of Mathematical Functions [page 362].

In the textbook, the degree is denoted as μ,equivalently to m in the above context, and order ν is equivalent to l. For this derivation, we maintain the notation in the textbook for consistency, Eq. (14.10.1) in the book refers to the occurrence relation between degrees, by reducing 1 degree the relation can be written as:

$$P_{\nu}^{\mu+1} + 2\mu x(1-x^2)^{-1/2}P_{\nu}^{\mu} + (\nu-\mu+1)(\nu+\mu)P_{\nu}^{\mu-1} = 0$$

Then in order to simplify the equation representation, $K = (1-x^2)$ treated as a constant:

$$P_{\nu}^{\mu+1} = -2\mu x K^{-1/2}P_{\nu}^{\mu} - (\nu-\mu+1)(\nu+\mu)P_{\nu}^{\mu-1} \tag{A.36}$$

For the Eq. (14.10.2) in the textbook:

$$K^{1/2}P_{\nu}^{\mu+1} = (\nu-\mu+1)P_{\nu+1}^{\mu} - (\nu+\mu+1)xP_{\nu}^{\mu} \tag{A.37}$$

Plugging (A.36) in (A.37):

$$K^{1/2}[-2\mu x K^{-1/2}P_{\nu}^{\mu} - (\nu-\mu+1)(\nu+\mu)P_{\nu}^{\mu-1}] = (\nu-\mu+1)P_{\nu+1}^{\mu} - (\nu+\mu+1)xP_{\nu}^{\mu}$$

Move P_{ν}^{μ} and its coefficient at the right side to the left side of the equation, and canceling K out:

$$-2\mu xP_{\nu}^{\mu} + (\nu+\mu+1)xP_{\nu}^{\mu} - K^{1/2}(\nu-\mu+1)(\nu+\mu)P_{\nu}^{\mu-1} = (\nu-\mu+1)P_{\nu+1}^{\mu}$$

Canceling the common term $(\nu + \mu + 1)$ out, the equation can be written as:

$$xP_\nu^\mu - K^{1/2}(\nu+\mu)P_\nu^{\mu-1} = P_{\nu+1}^\mu \tag{A.38}$$

Recall the derivative Eq. (14.10.4) at textbook:

$$K\frac{dP_\nu^\mu}{dx} = (\mu-\nu-1)P_{\nu+1}^\mu + (\nu+1)xP_\nu^\mu$$

Insert the term $P_{\nu+1}^\mu$ in Eq. (A.38) to the derivative equation:

$$\begin{aligned} K\frac{dP_\nu^\mu}{dx} &= (\mu-\nu-1)[xP_\nu^\mu - K^{1/2}(\nu+\mu)P_\nu^{\mu-1}] + (\nu+1)xP_\nu^\mu \\ &= \mu xP_\nu^\mu - K^{1/2}(\mu-\nu-1)(\nu+\mu)P_\nu^{\mu-1} \\ &= \mu xP_\nu^\mu + K^{1/2}(\nu-\mu+1)(\nu+\mu)P_\nu^{\mu-1} \end{aligned}$$

Recall the earlier simplification $K = (1-x^2)$, and $\nu \triangleq \mathrm{l}$, $\mu \triangleq m$, $x \triangleq u$ the final derivation can be written as:

$$(1-u^2)\frac{dP_l^m}{du} = muP_l^m + (1-u^2)^{1/2}(l-m+1)(l+m)P_l^{m-1}$$

A.2 Derivation of second order derivative of the Legendre polynomials P_l^m

From previous context, the first order derivative of Legendre polynomial $P_{l(u)}^m$ is defined in Eq. (A.42), and substitute $S = (l-m+1)(l+m)$ for simplification:

$$\frac{dP_l^m}{du} = \frac{muP_l^m + \overbrace{(l-m+1)(l+m)}^{S}(1-u^2)^{\frac{1}{2}}P_l^{m-1}}{1-u^2} \tag{A.42}$$

The derivative of $P_{l(u)}^m$ can be :

$$P_{l(uu)}^m = \frac{g(u)f'(u) - f(u)g'(u)}{[g(u)]^2}\text{,where}\begin{cases} f(u) = muP_l^m + S(1-u^2)^{\frac{1}{2}}P_l^{m-1} \\ g(u) = 1-u^2 \end{cases} \tag{A.43}$$

We first derive the first order derivative of $f(u)$ and $g(u)$:

$$\begin{aligned} f'(u) &= \frac{df(u)}{du} = mP_l^m + muP_{l(u)}^m - Su(1-u^2)^{-\frac{1}{2}}P_l^{m-1} + S(1-u^2)^{\frac{1}{2}}P_{l(u)}^{m-1} \\ g'(u) &= \frac{dg(u)}{du} = -2u \end{aligned} \tag{A.44}$$

Then plug Eq. (A.44) into Eq. (A.43) to obtain $P_{l(uu)}^m$:

$$\begin{aligned} &\frac{g(u)f'(u) - f(u)g'(u)}{[g(u)]} \\ &= \frac{Su(1-u^2)^{\frac{1}{2}}P_l^{m-1} + S(1-u^2)^{\frac{3}{2}}P_{l(u)}^{m-1} + (m+mu^2)P_l^m + mu(1-u^2)P_{l(u)}^m}{(1-u^2)^2} \\ &= \frac{Su}{(1-u^2)^{\frac{3}{2}}}P_l^{m-1} + \frac{S}{\sqrt{1-u^2}}P_{l(u)}^{m-1} + \frac{m(u^2+1)}{(1-u^2)^2}P_l^m + \frac{mu}{1-u^2}\underbrace{P_{l(u)}^m}_{Eq.\text{(A.42)}} \end{aligned} \tag{A.45}$$

The fourth term in Eq. (A.45) can be expanded by plugging in Eq. (A.42) :

$$\frac{mu}{1-u^2}P_{l(u)}^m = \frac{muS}{(1-u^2)^{\frac{3}{2}}}P_l^{m-1} + \left(\frac{mu}{1-u^2}\right)^2 P_l^m \tag{A.46}$$

plugging Eq. (A.46) into (A.45), and rearrage the terms, the final form of $P_{l(uu)}^m$ can be derived:

$$P_{l(uu)}^m = \frac{S}{\sqrt{1-u^2}}P_{l(u)}^{m-1} + \frac{uS(m+1)}{(1-u^2)^{\frac{3}{2}}}P_l^{m-1} + \frac{m^2u^2+mu^2+m}{(1-u^2)^2}P_l^m$$

The normalized $P_{l(uu)}^m$ is (denoted as $\hat{P}_{l(uu)}^m$):

$$\hat{P}_{l(uu)}^m = N_l^m P_{l(uu)}^m = \underbrace{\frac{N_l^m}{N_l^{m-1}}}_{\frac{1}{\sqrt{(l+m)(l-m+1)}}} \left[\frac{S}{\sqrt{1-u^2}}\hat{P}_{l(u)}^{m-1} + \frac{uS(m+1)}{(1-u^2)^{\frac{3}{2}}}\hat{P}_l^{m-1}\right] + \frac{m^2u^2+mu^2+m}{(1-u^2)^2}\hat{P}_l^m$$

$$\text{where}\begin{cases} N_l^m = \sqrt{\left(\frac{2l+1}{2}\right)\frac{(l-m)!}{(l+m)!}} \\ N_l^{m-1} = \sqrt{\left(\frac{2l+1}{2}\right)\frac{(l-m+1)!}{(l+m-1)!}} \end{cases}$$

Recall the definition of $S = (l+m)(l-m+1)$, $\hat{P}_{l(uu)}^m$ is derived as:

$$\hat{P}_{l(uu)}^m = \sqrt{\frac{(l+m)(l-m+1)}{1-u^2}}\left(\hat{P}_{l(u)}^{m-1} + \frac{u(m+1)}{1-u^2}\hat{P}_l^{m-1}\right) + \frac{m^2u^2+mu^2+m}{(1-u^2)^2}\hat{P}_l^m$$

When $m=0$:

$$\hat{P}_{l(uu)}^0 = \frac{-\sqrt{l(l+1)}\left[uP_l^1 + (1-u^2)P_{l(u)}^1\right]}{(1-u^2)^{\frac{3}{2}}}$$

APPENDIX B

SUPPORTING INFORMATION TO CHAPTER 3

B.1 EMPIRE mapping matrix H and state x definition

The mapping matrix $\mathbf{H}$ and state $\delta\mathbf{x}$ that appear in Eq. (2.25) are obtained by concatenating the transport terms of each of the estimated drivers that are estimated with EMPIRE $\mathbf{a}_\perp$ and $\mathbf{a}_\mathbf{u}$:

$$\delta\mathbf{a}_\perp = \mathbf{H}_\mathbf{V}\delta\mathbf{x}_\mathbf{V}$$

$$\delta\mathbf{a}_\mathbf{u} = \mathbf{H}_\mathbf{u}\delta\mathbf{x}_\mathbf{u}$$

The definition of the mapping matrix $\mathbf{H}_\mathbf{V}$ and the state $\delta\mathbf{x}_\mathbf{V}$ can be found in [90]. The mapping matrix $\mathbf{H}_\mathbf{u}$ and the state $\delta\mathbf{x}_\mathbf{u}$ are defined in [38]. They are obtained by substituting the expansions of the driver, Equations (B.3) and (B.4), into the corresponding density rate terms in Eq. (2.21) and stacking all the grid points. The potential field δV uses a scalar spherical harmonic expansion, derived in [90], using geomagnetic coordinates altitude, colatitude and longitude (r, θ, ϕ).

$$\delta V = \sum_{l=1}^{l_{\max}} \sum_{m=1}^{l} Y_l^m(L, \phi) \tag{B.3}$$

$$Y_l^m(L, \phi) = N_l^m P_l^m(L) \Phi_l^m(\phi)$$

$N_l^m P_l^m$ is the fully normalized associated Legendre polynomial as described by [173]. The potential field δV expansion depends on variable $L(r, \theta)$, that describes the normalized L-shell between domain $[-1, 1]$. This allows for the spatial potential field δV to be a function of only two independent variables (r, θ). This is done by assuming constant electric field along the dipole field lines. The term Φ_l^m contains the harmonic term and the unknown coefficients stacked in the state $\delta\mathbf{x}_\mathbf{V}$. To obtain the ion drift $\delta\vec{v}_\perp$, the electric field $\delta\vec{E}$ associated with ion motion is cross-multiplied with the Earth's magnetic field $\vec{B}_0$. The electric field $\delta\vec{E}$ is calculated as the gradient of the expanded electric potential δV and the IGRF-11 model [99] is used to obtain the magnetic field $\vec{B}_0$.

$$\delta\vec{v}_\perp = \frac{-\nabla\delta V \times \vec{B}_0}{B_0^2}$$

The neutral winds $\delta\vec{u}$ are expanded using a vector spherical harmonic expansion, derived in [38]. They are estimated by projecting the geographic meridional and zonal components, δu_N and δu_E respectively, onto the field-aligned direction $\hat{b}$ as shown in [90]. The assumption of negligible vertical winds in the vertical direction is made.

$$\delta\vec{u} = \sum_{l=1}^{l_{\max}}\sum_{m=1}^{l} Y_l^m(\cos\theta,\phi)\hat{r} + r\vec{\nabla}Y_l^m(\cos\theta,\phi) + \vec{r}\times\vec{\nabla}Y_l^m(\cos\theta,\phi) \tag{B.4}$$

Where $\delta\vec{u}$ is expanded in $(\hat{r},\hat{\theta},\hat{\phi})$, that are the unit vectors of a magnetic spherical coordinate system. Function Y_l^m has been defined in Eq. (B.1) which includes the harmonic term Φ_l^m that contains the unknown coefficients $\delta\mathbf{x_u}$.

B.2 ExB drift mapping matrices derivation The ExB drift $\delta\vec{v}_\perp$ at the i^{th} gridpoint defined in Eq. (2.29) can be decomposed into radial, magnetic co-latitudinal, and magnetic longitudinal components $\delta v_{\perp r}, \delta v_{\perp\theta}, \delta v_{\perp\phi}$, respectively, along the magnetic spherical coordinate directions $\hat{r},\hat{\theta},\hat{\phi}$. The detailed derivative expansion of these components was presented in Appendix A from [37], which we array here as:

$$\begin{aligned}\delta\vec{v}_\perp &= \begin{bmatrix}\delta v_{\perp_r} & \delta v_{\perp_\theta} & \delta v_{\perp_\phi}\end{bmatrix}^T \\ &= \begin{bmatrix}\underbrace{\frac{\delta V_{(\phi)}B_{0,\theta}}{{B_0}^2 r\sin(\theta)}}_{\delta v_{\perp r}} & \underbrace{-\frac{\delta V_{(\phi)}B_{0,r}}{{B_0}^2 r\sin(\theta)}}_{\delta v_{\perp\theta}} & \underbrace{\frac{B_{0,r}}{{B_0}^2 r}\delta V_{(\theta)} - \frac{B_{0,\theta}}{{B_0}^2}\delta V_{(r)}}_{\delta v_{\perp\phi}}\end{bmatrix}^T\end{aligned} \tag{B.5}$$

where the superscript T denotes matrix transpose. The magnetic field terms $B_{0,r}, B_{0,\theta}, B_{0,\phi}$ are the components of magnetic field in the spherical coordinate system, B_0 is the magnitude of the modeled magnetic field. We model them by IGRF-11, but simplify Eq. (B.5) by assuming that the magnetic field is close enough to dipolar that $B_\phi \approx 0$. The terms $\delta V_{(r)}, \delta V_{(\theta)}, \delta V_{(\phi)}$ are the derivatives of the spherical harmonic expansion of correction electric potential V in Eq. (2.31), with respect to r, θ, ϕ, respectively. (The subscript in parentheses denotes the variable with respect to which the derivative is taken.) The full forms of these derivatives are given in Appendix A of [37], and make use of recurrence relations for derivatives $P^m_{l(u)}$ of Legendre polynomials. An important update to the first order derivative of Legendre polynomial $P^m_{l(u)}$ is corrected in Appendix A.1 Eq. (A.22). For the i^{th} grid point:

$$\delta V_{(r)} = \sum_{l=1}^{l_{max}} \sum_{m=1}^{l} \underbrace{\frac{2\cos(m\phi)}{R_e \sin^2\theta (L_{max} - L_{min})} P^m_{l(u)}}_{\equiv c_r^{lm}} x_c^{lm} + \underbrace{\frac{2\sin(m\phi)}{R_e \sin^2\theta (L_{max} - L_{min})} P^m_{l(u)}}_{\equiv s_r^{lm}} x_s^{lm} \tag{B.6}$$

$$\delta V_{(\theta)} = \frac{-2r}{\tan\theta} \delta V_{(r)} \tag{B.7}$$

$$\delta V_{(\phi)} = \sum_{l=1}^{l_{max}} \sum_{m=1}^{l} \underbrace{\left(-mP_l^m \sin(m\phi)\right)}_{\equiv c_\phi^{lm}} x_c^{lm} + \underbrace{\left(mP_l^m \cos(m\phi)\right)}_{\equiv s_\phi^{lm}} x_s^{lm} \tag{B.8}$$

Expanding the summation terms $\delta V_{(r)}$,$\delta V_{(\theta)}$,$\delta V_{(\phi)}$ in Eq. (B.6),(B.7),(B.8) and rewriting in matrix form, the coefficients matrices $\mathbf{C_r}$,$\mathbf{C}_\theta$,$\mathbf{C}_\phi$ can be formulated:

$$\delta V_{(r)} = \underbrace{\begin{bmatrix} c_r^{11} & c_r^{21} & ... & c_r^{lm} & | & s_r^{11} & s_r^{21} & ... & s_r^{lm} \end{bmatrix}}_{\mathbf{C_r}} \underbrace{\begin{bmatrix} x_c^{11} & x_c^{21} & ... & x_c^{lm} & | & x_s^{11} & x_s^{21} & ... & x_s^{lm} \end{bmatrix}^T}_{\delta \mathbf{x_V}} \tag{B.9}$$

$$\delta V_{(\theta)} = \underbrace{\frac{-2r}{\tan\theta} \begin{bmatrix} c_r^{11} & c_r^{21} & ... & c_r^{lm} & | & s_r^{11} & s_r^{21} & ... & s_r^{lm} \end{bmatrix}}_{\mathbf{C}_\theta} \underbrace{\begin{bmatrix} x_c^{11} & x_c^{21} & ... & x_c^{lm} & | & x_s^{11} & x_s^{21} & ... & x_s^{lm} \end{bmatrix}^T}_{\delta \mathbf{x_V}} \tag{B.10}$$

$$\delta V_{(\phi)} = \underbrace{\begin{bmatrix} c_{\phi}^{11} & c_{\phi}^{21} & ... & c_{\phi}^{lm} & | & s_{\phi}^{11} & s_{\phi}^{21} & ... & s_{\phi}^{lm} \end{bmatrix}}_{\mathbf{C}_{\phi}} \underbrace{\begin{bmatrix} x_c^{11} & x_c^{21} & ... & x_c^{lm} & | & x_s^{11} & x_s^{21} & ... & x_s^{lm} \end{bmatrix}^T}_{\delta \mathbf{x_V}} \tag{B.11}$$

By plugging Eq. (B.9),(B.10),(B.11) into Eq. (B.5) and reorganizing the terms, row matrices $\mathbf{H}_{\perp \mathbf{r}}$,$\mathbf{H}_{\perp\theta}$, $\mathbf{H}_{\perp\phi}$ in Eq. (2.34) map the basis function coefficients for electric potential $\delta\mathbf{x_V}$ to three components of $\delta\vec{v}_{\perp}$ along centered dipole spherical coordinate directions $\hat{r}, \hat{\theta}, \hat{\phi}$:

$$\delta\vec{v}_{\perp} = \begin{bmatrix} \delta v_{\perp r} \\ \delta v_{\perp\theta} \\ \delta v_{\perp\phi} \end{bmatrix} = \begin{bmatrix} \mathbf{H}_{\perp \mathbf{r}} \\ \mathbf{H}_{\perp\theta} \\ \mathbf{H}_{\perp\phi} \end{bmatrix} \begin{bmatrix} \delta\mathbf{x_V} \end{bmatrix}$$

The relation between $\mathbf{H}_{\perp \mathbf{r}}$,$\mathbf{H}_{\perp\theta}$, $\mathbf{H}_{\perp\phi}$ and $\mathbf{C_r}$,$\mathbf{C}_{\theta}$, $\mathbf{C}_{\phi}$ are shown as in Eq. (B.12), (B.13), (B.14)

$$\mathbf{H}_{\perp \mathbf{r}} = \frac{B_{0,\theta}}{{B_0}^2 r \sin(\theta)} \mathbf{C}_{\phi} \tag{B.12}$$

$$\mathbf{H}_{\perp\theta} = -\frac{B_{0,r}}{{B_0}^2 r \sin(\theta)} \mathbf{C}_{\phi} \tag{B.13}$$

$$\mathbf{H}_{\perp\phi} = -\frac{B_{0,\theta}}{{B_0}^2} \mathbf{C_r} + \frac{B_{0,r}}{{B_0}^2 r} \mathbf{C}_{\theta} \tag{B.14}$$

B.3 Background model covariance setup in the Kalman filter In EMPIRE, we estimate the ionospheric drivers of electric potential and neutral wind, and the formation of counterpart background model covariance appearing in Eq. (2.28) describes the uncertainty of background state vector for these two drivers. Here we derive the background model covariance $\mathbf{P_{0,k|k}}$ for electric potential; the formation for neutral wind is analogous.

The background electric potential state vector $\mathbf{\hat{x}_{V,0}}$ for l-order equal to 6 is estimated in Eq. (B.15), which is Weimer modeled ExB velocity $\mathbf{v_{\perp 0}}$ linearly transformed by the Moore–Penrose inverse operator of ExB velocity mapping matrix $\mathbf{F}_{\perp}^{\dagger}$. The Weimer model yields ExB drifts in magnetic radial, latitudinal, and longitudianl directions as $\mathbf{v_{\perp 0,r}}$, $\mathbf{v}_{\perp\mathbf{0},\theta}$ and $\mathbf{v}_{\perp\mathbf{0},\phi}$ respectively. The corresponding mapping matrices are $\mathbf{F_{\perp r}}$, $\mathbf{F}_{\perp\theta}$ and $\mathbf{F}_{\perp\phi}$.

$$\underbrace{\mathbf{\hat{x}_{V,0}}}_{[42\times 1]} = \mathbf{F}_{\perp}^{\dagger}\mathbf{v_{\perp 0}} = \underbrace{\begin{bmatrix} \mathbf{F_{\perp r}} \\ \\ \mathbf{F}_{\perp\theta} \\ \\ \mathbf{F}_{\perp\phi} \end{bmatrix}^{\dagger}}_{[42\times 3n]} \underbrace{\begin{bmatrix} \mathbf{v_{\perp 0,r}} \\ \\ \mathbf{v}_{\perp\mathbf{0},\theta} \\ \\ \mathbf{v}_{\perp\mathbf{0},\phi} \end{bmatrix}}_{[3n\times 1]} \tag{B.15}$$

The background state covariance $\mathbf{P_{xV}}$ is defined by the linear transformation from Eq. (B.15), where $\mathbf{P_{v_{\perp 0}}}$ is the background velocity error covariance matrix:

$$\underbrace{\mathbf{P_{xV}}}_{[42\times 42]} = \underbrace{\mathbf{F}_{\perp}^{\dagger}}_{[42\times 3n]} \underbrace{\mathbf{P_{v_{\perp 0}}}}_{[3n\times 3n]} \underbrace{(\mathbf{F}_{\perp}^{\dagger})^{\mathbf{T}}}_{[3n\times 42]} \tag{B.16}$$

Assuming the background model values for each n-th grid is linearly independent, $\mathbf{P_{v_{\perp 0}}}$ is a diagonal variance matrix, and $\mathbf{0}$ is a square matrix of zeros of dimension $[n \times n]$. The background ExB velocity error variances in r, θ, ϕ direction are $\sigma^{\mathbf{2}}_{\mathbf{v_{\perp 0,r}}}, \sigma^{\mathbf{2}}_{\mathbf{v}_{\perp\mathbf{0},\theta}}, \sigma^{\mathbf{2}}_{\mathbf{v}_{\perp\mathbf{0},\phi}}$ correspondingly, and each diagonal matrix has dimension of [n × n]:

$$\mathbf{P_{v_{\perp}0}} = \begin{bmatrix} \mathbf{diag}(\sigma^{\mathbf{2}}_{\mathbf{v_{\perp}0,r}}) & \mathbf{0} & \mathbf{0} \\ \mathbf{0} & \mathbf{diag}(\sigma^{\mathbf{2}}_{\mathbf{v_{\perp}0,\theta}}) & \mathbf{0} \\ \mathbf{0} & \mathbf{0} & \mathbf{diag}(\sigma^{\mathbf{2}}_{\mathbf{v_{\perp}0,\phi}}) \end{bmatrix} \tag{B.17}$$

For each i^{th} direction $i = \{“r”, “\theta”, “\phi”\}$, the background velocity error variance matrix $\mathbf{diag}(\sigma^{\mathbf{2}}_{\mathbf{v_{\perp}0,i}})$ is composed of fitting error and the background model error:

$$\mathbf{diag}(\sigma^{\mathbf{2}}_{\mathbf{v_{\perp}0,i}}) = \mathbf{diag}(\sigma^{\mathbf{2}}_{\mathbf{\perp fitting,i}} + \sigma^{\mathbf{2}}_{\mathbf{\perp climate,i}}) \tag{B.18}$$

The fitting error of the mapping matrix is defined as the standard deviation of the difference between the estimated mapping value $\mathbf{F_{\perp i}\hat{x}_{V,0}}$ and the background values $\mathbf{v_{\perp 0,i}}$ over the global map:

$$\sigma_{\mathbf{\perp fitting,i}} = std(\mathbf{F_{\perp i}\hat{x}_{V,0}} - \mathbf{v_{\perp 0,i}}) \tag{B.19}$$

Since the correction of ExB velocity is estimated, the background model errors must be regarded in the process update during storm time, and they are assumed to be 70% of modeled values:

$$\sigma_{\mathbf{\perp climate,i}} = \mathbf{70\% v_{\perp 0,i}} \tag{B.20}$$

Plugging in Equations (B.19) and (B.20) into Eq. (B.18), then Eq. (B.17) is formed with the diagonal values from Eq. (B.18). By the linear transformation in Eq. (B.16), the electric potential background state covariance $\mathbf{P_{xV}}$ is obtained as a rectangular matrix in $\mathbf{P_{0,k|k}}$ at the k-th time epoch, and $\mathbf{0}$ are the rectangular matrices that fill the gaps:

$$\mathbf{P_{0,k|k}} = \underbrace{\begin{bmatrix} \underbrace{\mathbf{P_{xV}}}_{[42\times42]} & \mathbf{0} \\ \mathbf{0} & \underbrace{\mathbf{P_{xu}}}_{[48\times48]} \end{bmatrix}}_{[90\times90]}$$

The derivation of P_{xu} for the neutral wind driver δx_u is defined similarly by replacing the mapping matrix $F_\perp$ with the mapping matrix F_u [38] that maps the neutral wins corrections onto the geographic east and north directions, for which $\mathbf{v_i} = \{\text{“}u_E\text{”}, \text{“}u_N\text{”}\}$. Note that the background model covariance $\mathbf{P_{0,k|k}}$ is assumed to be a diagonal matrix at each time epoch, and the correlation between neutral wind and ion drifts are neglected in the simplified setup. However in a more realistic setting, the off-diagonal terms in $\mathbf{P_{0,k|k}}$ should be non-zero to improve the driver estimations.

B.4 EMPIRE sensitivity to the change of ion and electron temperature in the ion contiuity equation

A sensitivity analysis was conducted by examining the dependency of ion and electron temperatures for collision frequency related to ion temperature, and for diffusion coefficient related to both of ion and electron temperatures.

Assuming the only ion specie is O^+, the field-parallel speed $v_\parallel$ is simplified as in Eq. (B.21) [89], based on Kirchengast model [93], with drivers of neutral wind $u_\parallel$, gravitational effect $\frac{g_\parallel}{\nu_{o^+}}$ and the diffusion term along the field-line.

$$v_\parallel = u_\parallel + \frac{g_\parallel}{\nu_{o^+}} - \underbrace{\frac{k_B(T_i + T_e)}{m_{o^+}\nu_{o^+}(1 - \triangle_{in})}}_{D} \frac{\nabla_\parallel N}{N} \tag{B.21}$$

where $g_{\|}$ is gravity, and ν_{o^+} is the $O^+ - O$ collision frequency. The diffusion coefficient D is formulated by the combination of Boltzmann's constant k_B, ion and electron temperatures $(T_i + T_e)$, O^+ mass m_{ν^+}, ion-neutral collision adjustment term $\triangle_{in}$ (assumed 0 in EMPIRE). The gradient of electron density N along the magnetic field line is denoted as $\nabla_{\|}N$.

The collision frequency ν_{o^+} is dependent on ion temperatures, and can be formulated as:

$$\nu_{o^+} = C_1 N_o \left(\frac{T_i + T_n}{2}\right)^{1/2} (C_2 - C_3 \log_{10}\left(\frac{T_i + T_n}{2}\right))^2 + C_4 N_{o^2} + C_5 N_{N^2}$$

where C_1,C_2,C_3,C_4,C_5 are provided constant coefficients for the ion-neutral frequency, and the neutral density of atmoic oxygen, oxygen and nitrogen molecules are denoted by N_o, N_{o^2} and N_{N^2} correspondingly. T_n is the neutral temperature.

The partial derivatives of collision frequency with respect to ion temperature $\frac{\partial \nu_{o^+}}{\partial T_i}$. The diffusion coefficient partial derivatives respect to ion and electron temperatures denoted by $\frac{\partial D}{\partial T_i}$ and $\frac{\partial D}{\partial T_e}$ respectively, are formulated in the following context.

The partial derivative of collision frequency with respect to ion temperature is:

$$\frac{\partial \nu_{o^+}}{\partial T_i} = C_1 N_o T^{-\frac{1}{2}} \left[\frac{1}{4}(C_2 - C_3 \log_{10} T)^2 - \frac{C_3}{\ln 10}(C_2 - C_3 \log_{10} T)\right], \text{where } T = \frac{T_i + T_n}{2}$$

The partial derivative of diffusion coefficient with respect to ion temperature is:

$$\frac{\partial D}{\partial T_i} = \frac{k_B\left(\nu_{o^+} - (T_i + T_e)\frac{\partial \nu_{o^+}}{\partial T_i}\right)}{m_{o^+}(\nu_{o^+})^2}$$

The partial derivative of diffusion coefficient with respect to electron temperature is presented at Eq. (B.22).

$$\frac{\partial D}{\partial T_e} = \frac{k_B}{m_{o^+}\nu_{o^+}} \tag{B.22}$$

To show the changes subject to temperature variations (pick $\triangle T_i = \triangle T_e = 100\ K$), the variation percent of dependent variables are approximated by first order Taylor expansion as:

$$\frac{\triangle \nu_{o^+}}{\nu_{o^+}} = \frac{\partial \nu_{o^+}}{\partial T_i}\triangle T_i, \frac{\triangle D}{D} = \frac{\partial D}{\partial T_i}\triangle T_i + \frac{\partial D}{\partial T_e}\triangle T_e$$

The fractional changes $\triangle \nu_{O^+}/\nu_{O^+}$ and $\triangle D/D$ for each temperature input to the EMPIRE horizontal grid at 300 kilometers is plotted in Fig. B.1 (a) and (b), respectively. The bounded 5 percent of the variations in response to temperature changes of 100 K suggest that the ion continuity formulation is not significantly affected by varying ion and electron temperature inputs. Furthermore, with regard to the loss term, the loss disturbance is negligible at F region [100]. Hence, the ingestion of IRI temperature data, instead of SAMI3 which would be self-consistent with the truth reference but were not saved, is not expected to have a substantial effect on EMPIRE estimations.

B.5 EMPIRE experimental setup without incorporating representation error

Appendix B.5 illustrates the impacts of eliminating representation errors in the

Change of collision frequency ν_{o^+} and diffusion coefficient D with respect to ion and electron temperature T_i and T_e

(a) $\Delta\nu_{o^+}/\nu_{o^+}$ v.s. T_i

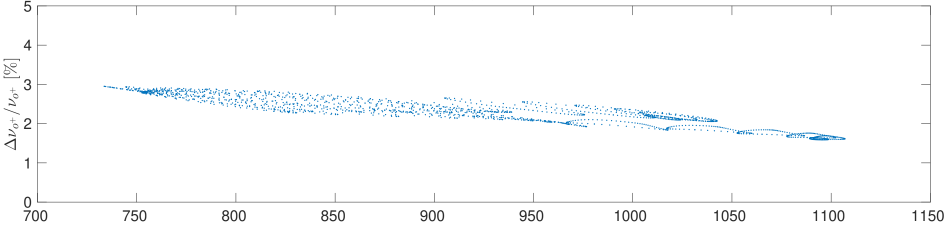

(b) $\Delta D/D$ v.s. $(T_i + T_e)$

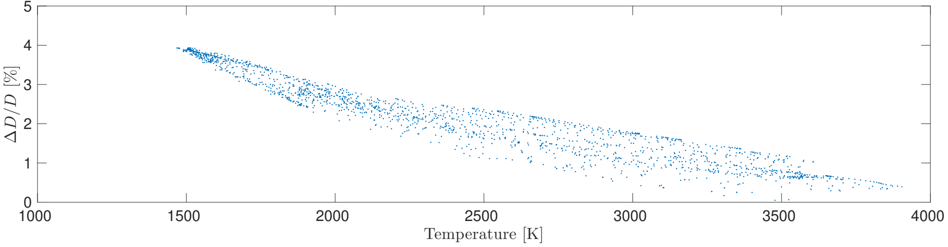

Figure B.1. Change of collision frequency ν_{o^+} and diffusion coefficient D with respect to ion temperature T_i and electron temperature T_e. (a) The variation of collision frequency $\triangle\nu_{o^+}$ over ν_{o^+} [%] with respect to T_i. (b) The variation of diffusion coefficient $\triangle D$ over D [%] with respect to $T_i + T_e$. Each dot in the subplots represents a data pair for the EMPIRE horizontal map at altitude of 300 km. The x-axes is the temperature in the unit of Kelvin, and y-axes is the variation percentage.

original EMPIRE setup. The experimental flowchart is represented in Fig. B.2, and the observation error is only due to the climate model with the simulated truth as inputs. This result serves as the control for the experiment with the EMPIRE setup of incorporating representation error in Chapter 4. The same analysis period from 25-26 August 2018 is selected, and the same data sources are ingested in this study (i.e. SAMI3 outputs are treated as simulated truth).

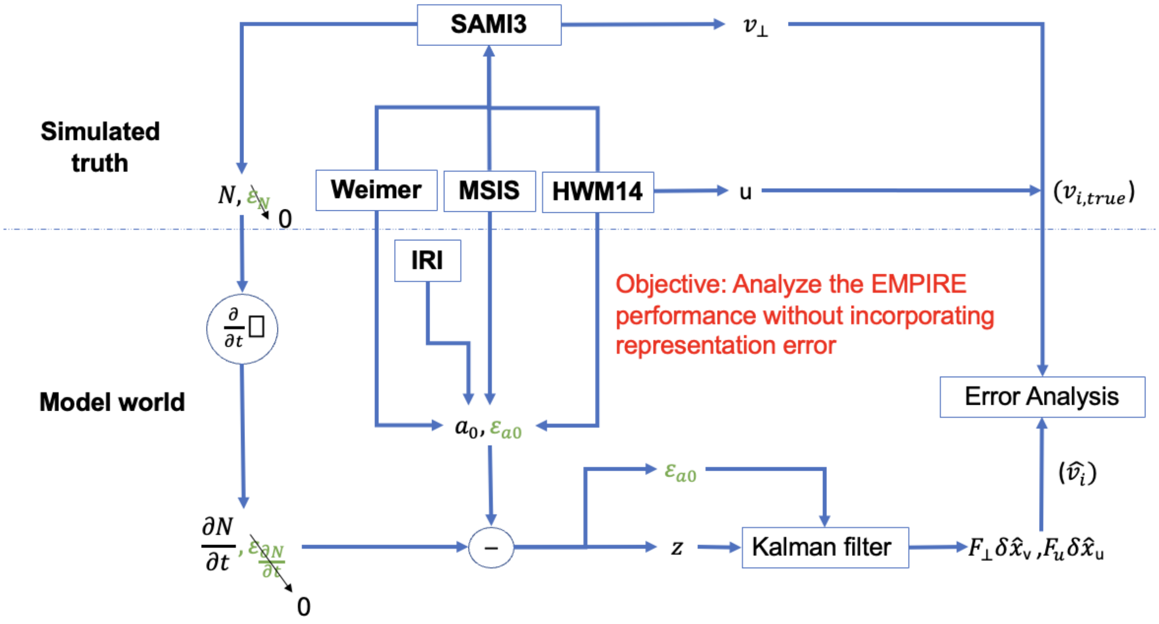

Figure B.2. Block diagram of EMPIRE performance analysis with SAMI3 as the self-consistent truth source, in which EMPIRE does not take representation error into account. The electron density rate $\partial N/\partial t$ is obtained from the electron density N from the SAMI3 model, and the time-differencing error is $\epsilon_{\partial N/\partial t}$, counted as one component of measurement error. The observation error ϵ_{a_0} (equivalent to ϵ in Figure 3.3) is due to the background modeled term a_0, which is modeled by Weimer, HWM14, IRI and MSIS. The gap between $\partial N/\partial t$ and a_0 is treated as the measurement vector.

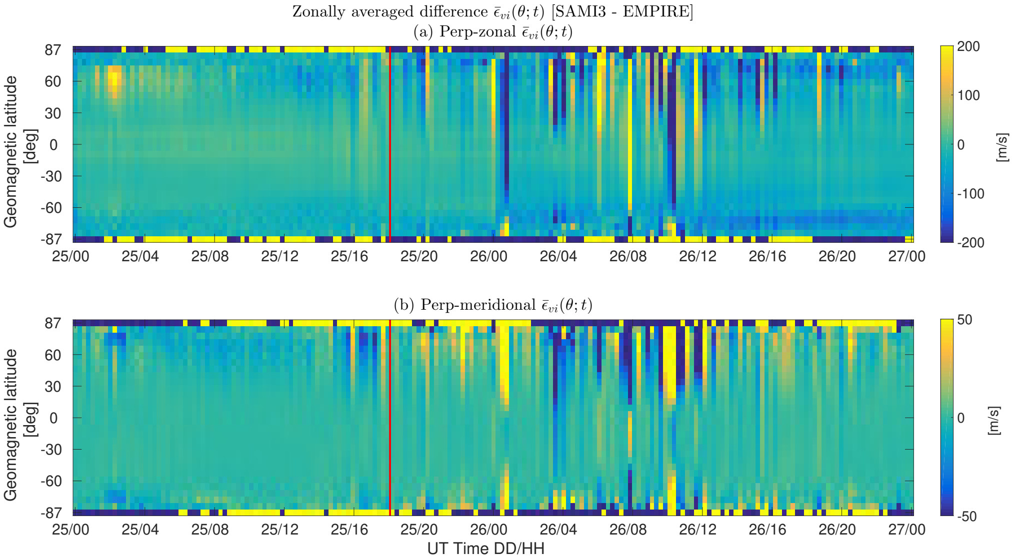

Figure B.3. Zonally averaged differences between SAMI3 and EMPIRE correction of ion drifts in the (a) field-perpendicular zonal and (b) field-perpendicular meridional directions, without the representation error formulation of Chapter 4. The red vertical line separates the quiet and storm periods: 00 UT to 18 UT August 25th is the quiet period, and 18 UT August 25th to 00 UT August 27th is the storm period.

B.6 EMPIRE performance analysis

To analyze the difference due to experimental setups between Section 3.2 and Appendix B.5 quantitatively, Figure 3.4, 3.5, 3.7 in Chapter 3 are reproduced for the current experimental setup, as Figure B.3, Figure B.4, Figure B.5 respectively.

Figure B.3 shows the zonally averaged differences between SAMI3 and EMPIRE correction of ion drifts in (a) field-perpendicular zonal and (b) field-perpendicular meridional directions. Comparing to Figure 3.4, vertical blue and yellow stripes are visible for EMPIRE case without formulation of representation error, which indicates larger random noise exists in the state estimations. Also, the state estimation is more disturbed during storm time than quiet time.

Figure B.4 plots the time-averaged ion drift relative errors on a log base-10 scale in (a) field-perpendicular zonal and (b) field-perpendicular meridional direc-

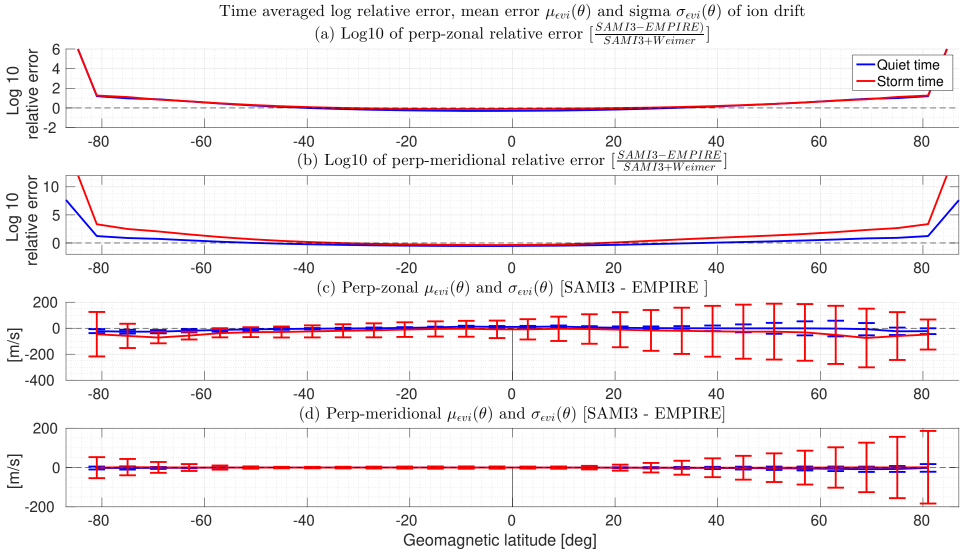

Figure B.4. The time averaged ion drift relative errors on a log base-10 scale versus geomagnetic latitude are presented in (a) field-perpendicular zonal direction and (b) field-perpendicular meridional direction, for EMPIRE case without representation error formulation. The horizontal dashed line in (a) and (b) indicate that the relative error is 100%. The time-averaged error $\mu_{\epsilon \mathbf{vi}}(\theta)$ and standard deviation $\sigma_{\epsilon \mathbf{vi}}(\theta)$ between SAMI3 and EMPIRE corrected ion drifts versus magnetic latitude are plotted in the field-perpendicular (c) zonal and (d) meridional directions. The horizontal dashed line indicates 0 velocity components. The vertical black line is the 0° latitude line. Quiet and storm time error statistics are plotted with blue and red lines, respectively.

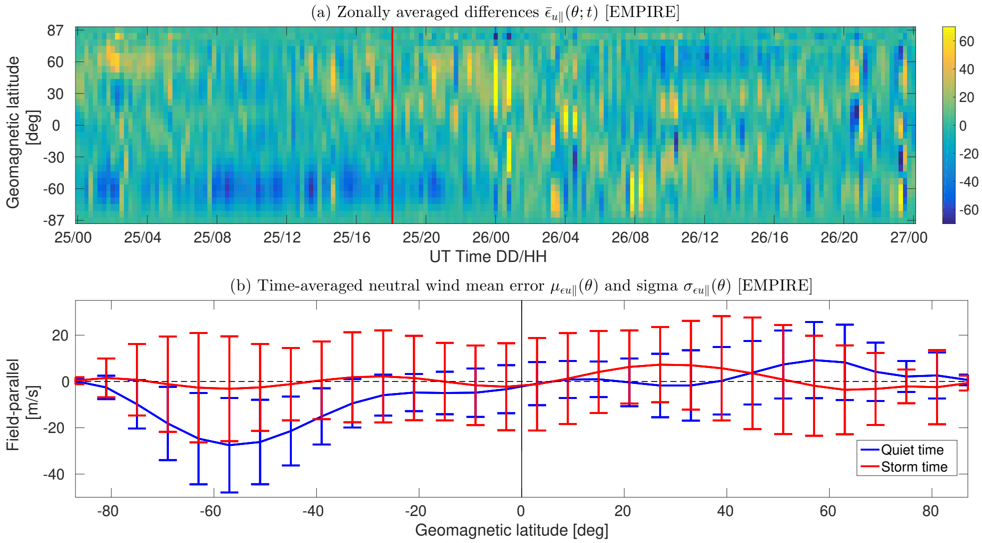

Figure B.5. (a) Zonally averaged difference of neutral wind in the field-parallel direction from EMPIRE corrections $\bar{\epsilon}_{\mathbf{u}\|}(\theta, \mathbf{t})$ across analysis time, without representation error formulation. The red vertical line separates the quiet and storm periods. (b) Time-averaged EMPIRE field-parallel neutral wind mean errors $\mu_{\epsilon \mathbf{u}\|}$ and standard deviations $\sigma_{\epsilon \mathbf{u}\|}$ as a function of magnetic latitude.

tions. The dashed line indicates the relative error exceeds 100%. It can be observed that the low-to-mid latitude (within ±40°) relative error is nearly 100%, and increases more quickly for higher latitudes, compared to Figure 3.5. The time-averaged error and its standard deviation between SAMI3 and EMPIRE corrections are shown in subplot (c) and (d) for field-perpendicular zonal and meridional directions. For the field-perpendicular zonal direction, the error sigmas at all latitudes are bounded within 50 $[m/s]$ during quiet-time, but storm-time error sigmas reach to 200 $[m/s]$ at NH mid-latitudes. The quiet-time error sigma is bounded within 20 $[m/s]$ for field-perpendicular meridional direction, but exceeds 200 $[m/s]$ at NH high latitudes.

Figure B.5 (a) shows the EMPIRE neutral wind estimation on the field-parallel direction, from which figure the color stripes indicating significant error are randomly distributed across time and latitudes. The time-averaged neutral wind are plotted in Figure B.5 (b). For quiet time, the mean estimations peak at latitudes of ± 60°, and the sigmas is about 4 times larger than 3.7 (b). The mean error during storm time is closer to 0, but the sigmas are approximately 20 $[m/s]$ across low-to-mid latitudes, compared to lower sigma values bounded within 15 $[m/s]$ from Figure 3.7 (b).

The noise in state estimation is due to biased Kalman gain calculated based on the ratio of observation error covariance $\mathbf{R}$ and prior state covariance $\mathbf{P_k^-}$. Recall the Eq. (2.11), if $\mathbf{R}$ is formulated much smaller than the actual value (i.e. eliminating the representation error source), so it leads to larger values of Kalman gain and more weights are added to the observation vector $\mathbf{z}$. Less information from prior state is inherited to the posterior state estimations, which might lead to the posterior state being uncorrelated to the prior states, so random noise appeared as color stripes on the Figure B.3 and Figure B.5. Although observation vector $\mathbf{z}$ is assumed error-free, the actual finite time differencing step (from $\mathbf{N}$ to $\frac{\partial \mathbf{N}}{\partial \mathbf{t}}$) carries algorithmic errors into the Kalman gain calculation. The algorithmic errors are intensified due to more gains on the observation vector, which introduces larger errors into the state estimations.

Appendix B.5 is set up as a supplementary study related to the Chapter 4, and shows that it is essential to include the representation error to the Kalman gain calculation for capturing the missing error sources.

APPENDIX C

SUPPORTING INFORMATION TO CHAPTER 4

C.1 Bearing angle derivation and coordinate transformations

The rotation matrix ${}^{\mathbf{gm}}\mathrm{R}^{\mathbf{sph}}$ transforms components from geomagnetic spherical coordinates $\hat{r}, \hat{\theta}, \hat{\phi}$ to geomagnetic east-north-up (ENU) coordinates $\hat{m}_E, \hat{m}_N, \hat{m}_U$.

$$ {}^{\mathbf{gm}}\mathrm{R}^{\mathbf{sph}} = \begin{bmatrix} 0 & 0 & 1 \\ 0 & -1 & 0 \\ 1 & 0 & 0 \end{bmatrix} $$

The rotation matrix ${}^{\mathbf{field}}\mathrm{R}^{\mathbf{gm}}$ transforms components from geomagnetic ENU to magnetic field coordinates, $\hat{\perp}_{zonal}, \hat{b}, \hat{\perp}_{merid}$:

$$ {}^{\mathbf{field}}\mathrm{R}^{\mathbf{gm}} = \begin{bmatrix} 1 & 0 & 0 \\ 0 & \cos I & -\sin I \\ 0 & \sin I & \cos I \end{bmatrix} \tag{C.1} $$

where I is the inclination angle of the local magnetic field with respect to the horizontal, defined positive downward. Recall the velocity decomposition in Figure 4.1 for each measurement, the bearing angle γ between $\hat{\mathbf{m}}_{\mathbf{N}}$ and v_{lp} is calculated by the components projected onto the $\hat{\mathbf{m}}_{\mathbf{E}}$ and $\hat{\mathbf{m}}_{\mathbf{N}}$ directions, denoted as v_{mE} and v_{mN} respectively:

$$ \tan(\beta - D) = \frac{v_{mE}}{v_{mN}} \tag{C.2} $$

The measured velocity geomagnetic east and north components (v_{mE} and v_{mN})

can be calculated through the relation:

$$\begin{bmatrix} v_{mE} \\ v_{mN} \\ v_{mU} \end{bmatrix} = (^{\mathbf{field}}\mathrm{R}^{\mathbf{gm}})^{\mathbf{T}} \begin{bmatrix} v_l \sin\alpha \\ 0 \\ v_l \cos\alpha \end{bmatrix} \tag{C.3}$$

Expand Eq. (C.3) and plug the components into Eq. (C.2):

$$\gamma = \beta - D \tan(\beta - D) = \frac{\tan\alpha}{\sin I} \tag{C.4}$$

Reorganize Eq. (C.4), the bearing angle α is derived:

$$\alpha = \arctan(\tan(\beta - D)\sin I)$$

Another required rotation matrix that transform geomagnetic coordinates to geographic coordinates $^{\mathbf{g}}\mathrm{R}^{\mathbf{gm}}$ in Eq. (4.3) is:

$$^{\mathbf{g}}\mathrm{R}^{\mathbf{gm}} = \begin{bmatrix} \cos D & \sin D & 0 \\ -\sin D & \cos D & 0 \\ 0 & 0 & 1 \end{bmatrix} \tag{C.5}$$

Recall Fig. 4.1, the line-of-sight measurement vector $\vec{v_l}$ can be expressed in the field-perpendicular zonal-meridional plane in Eq. (C.6), with the velocity magnitude denoted as vl.

$$\vec{v_l} = v_l \sin\alpha \hat{\perp}_z + v_l \cos\alpha \hat{\perp}_m \tag{C.6}$$

Recall the rotation matrix in Eq. (C.1), $\vec{v_l}$ can be rewritten in geomagnetic coordinates as:

$$\vec{v_l} = {}^{\mathbf{gm}}\mathrm{R}^{\mathbf{field}}\vec{v_l}$$

The projection of $\vec{v_l}$ on to the geomagnetic East-North plane is:

$$\vec{v_{lp}} = v_l \sin\alpha \hat{m}_E + v_l \cos\alpha \sin I \hat{m}_N$$

C.2 Ingesting Millstone Hill Incoherent Scatter Radar ion drift measurements

Chapter 4 describes the experimental setup for augmenting SuperDARN measurements, and it can be extended to ingest Millstone Hill Incoheren Scatter Radar (ISR) measurements by same analogy. In this new augmentation, an array of direct ISR measurements of ion velocity with measurements of $\mathbf{z_{dN/dt}}$ from IDA4D are also ingested as $\mathbf{z_{ISR}}$. The augmented linear system is:

$$\begin{bmatrix} \mathbf{z_{dN/dt}} \\ \\ \mathbf{z_{ISR}} \end{bmatrix} = \begin{bmatrix} \mathbf{H_V} & \mathbf{H_u} \\ \\ \mathbf{H_{ISR}} & \mathbf{0} \end{bmatrix} \begin{bmatrix} \delta\mathbf{x_V} \\ \\ \delta\mathbf{x_u} \end{bmatrix} + \begin{bmatrix} \varepsilon \\ \\ \varepsilon_{\mathbf{ISR}} \end{bmatrix} \tag{C.7}$$

where $\mathbf{0}$ is a block matrix of zeros in coefficient matrix. The augmented linear system is then used to estimate $\mathbf{x}$ via Kalman filter.

In Eq. (C.7), the observation $\mathbf{z_{ISR}}$ is an array of length i direct measurements of LOS ion velocity v_{LOS} made within the estimation time interval dt stacked with the array $\mathbf{z_{dN/dt}}$. Each i^{th} point is a specific measurement location specified by the data providers at a given geographic longitude, latitude and altitude, and at a given look direction specified by geographic azimuth az and elevation el angles. The measurement locations do not have to coincide with the grid-points used in the

EMPIRE continuity equation. The matrix $\mathbf{H_{ISR}}$ maps the coefficients $\delta \mathbf{x_V}$ for the potential V in Eq. (2.31) that yields the ExB ion drift onto the LOS direction. The measurement noise is $\varepsilon_{\mathbf{ISR}}$ from the instrument data providers of the ion drift. In the next steps, we define how the vector ExB drift $\vec{v}_\perp$ is projected onto the LOS direction.

Performing the rotation from geomagnetic to geographic coordinate yields the geographic components of ion velocity along the $\hat{g_E}$, $\hat{g_N}$, $\hat{g_u}$ directions.

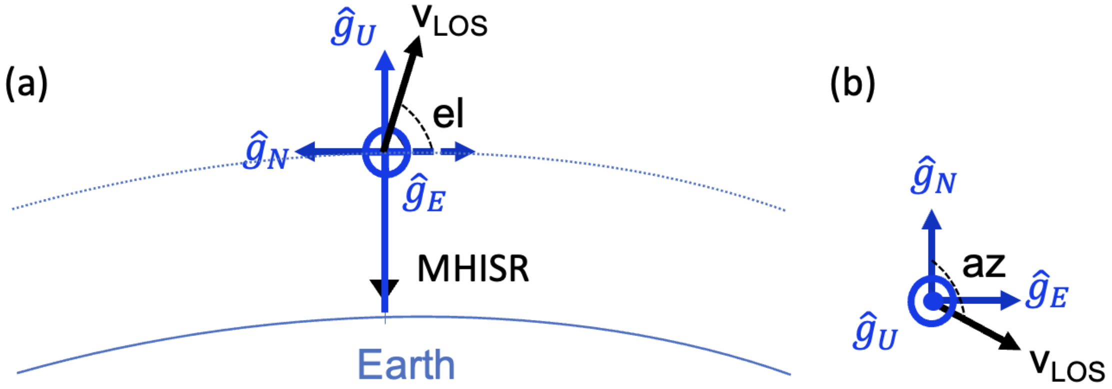

Figure C.1. LOS ion velocity with geographic azimuth angle az and elevation angle el. $\hat{g_E}$, $\hat{g_N}$, $\hat{g_U}$ are the geographic ENU axes.

.

The radar viewing direction is defined by two angles: azimuth az and elevation el (Figure C.1), measured with respect to geographic ENU coordinates. Eq. (C.8) uses these angles to project the ion velocity at each i^{th} measurement location from geographic ENU coordinates onto the line-of-sight direction.

$$v_{LOS,i} = \begin{bmatrix} \cos(el)\sin(az) & \cos(el)\cos(az) & \sin(el) \end{bmatrix}_i {}^{\mathbf{g}}\mathrm{R}^{\mathbf{gm}}\,{}^{\mathbf{gm}}\mathrm{R}^{\mathbf{sph}} \begin{bmatrix} v_{\perp_r} \\ v_{\perp_\theta} \\ v_{\perp_\phi} \end{bmatrix}_i \qquad \text{(C.8)}$$

Plugging Eq. (2.34) for $v_{\perp_r}$,$v_{\perp_\theta}$,$v_{\perp_\phi}$ derived into Eq. (C.8), the row matrix

$\mathbf{H_{ISR,i}}$ at the i^{th} measurement location is obtained as the matrix product in Eq. (C.9):

$$\mathbf{H_{ISR,i}} = \begin{bmatrix} \cos(el)\sin(az) & \cos(el)\cos(az) & \sin(el) \end{bmatrix}_i {}^{\mathbf{g}}\mathrm{R}^{\mathbf{gm}}{}^{\mathbf{gm}}\mathrm{R}^{\mathbf{sph}} \begin{bmatrix} \mathbf{H}_{\perp\mathbf{r}} \\ \mathbf{H}_{\perp\theta} \\ \mathbf{H}_{\perp\phi} \end{bmatrix}_i \tag{C.9}$$

This row matrix, when stacked for all i measurements, maps the electric potential coefficients $\mathbf{x_V}$ to the line-of-sight observations $\mathbf{z_{ISR}}$ for the Kalman filter setup in Eq. (C.7).

BIBLIOGRAPHY

[1] World Data Center for Geomagnetism, Kyoto, M. Nose, T. Iyemori, M. Sugiura, T. Kamei, “Geomagnetic ap index [dataset],” 2018.

[2] ACE Science Center, “Ace swepam level 2 magnetic field data [dataset],” 2018. [Online; accessed Oct. 10, 2023].

[3] “NOAA Space Weather Prediction Center : Deep Space Climate Observatory (DSCOVR),” *NOAA National Centers for Environmental Information*, 2016. Dataset. http://doi.org/10.7289/V51Z42F7.

[4] J. Hu, A. L. Rubio, A. Chartier, S. McDonald, and S. Datta-Barua, “Quantification of representation error in the neutral winds and ion drifts using data assimilation,” *Americna Geophysical Union, Space Weather*, 2024.

[5] W. Ward, A. Seppälä, E. Yiğit, T. Nakamura, C. Stolle, J. Laštovička, T. N. Woods, Y. Tomikawa, F.-J. Lübken, S. C. Solomon, *et al.*, “Role of the sun and the middle atmosphere/thermosphere/ionosphere in climate (rosmic): a retrospective and prospective view,” *Progress in Earth and Planetary Science*, vol. 8, pp. 1–38, 2021.

[6] D. S. Miladinovich, *Data assimilation for ionosphere-thermosphere storm-time state estimation*. PhD thesis, Illinois Institute of Technology, 2018.

[7] A. Lupo, W. Kininmonth, J. Armstrong, and K. Green, “Global climate models and their limitations,” *Climate change reconsidered II: Physical science*, vol. 9, p. 148, 2013.

[8] W. Lahoz, B. Khattatov, and R. Ménard, “Data assimilation and information,” in *Data assimilation*, pp. 3–12, Springer, 2010.

[9] S. K. Park and L. Xu, *Data Assimilation for Atmospheric, Oceanic and Hydrologic Applications (Vol. II)*. Springer, 2013.

[10] M. C. Kelley, *The Earth’s ionosphere: Plasma physics and electrodynamics*. Academic press, 2009.

[11] W. Schröder, “Some aspects of the earlier history of solar-terrestrial physics,” *Planetary and space science*, vol. 45, no. 3, pp. 395–400, 1997.

[12] G. S. Lakhina and B. T. Tsurutani, “Geomagnetic storms: historical perspective to modern view,” *Geoscience Letters*, vol. 3, no. 1, pp. 1–11, 2016.

[13] S. Kahler, “Solar flares and coronal mass ejections,” *Annual review of astronomy and astrophysics*, vol. 30, pp. 113–141, 1992.

[14] B. T. Tsurutani, W. D. Gonzalez, F. Tang, and Y. T. Lee, “Great magnetic storms,” *Geophysical Research Letters*, vol. 19, no. 1, pp. 73–76, 1992.

[15] G. Rostoker, “Geomagnetic indices,” *Reviews of Geophysics*, vol. 10, no. 4, pp. 935–950, 1972.

[16] H. Lundstedt, H. Gleisner, and P. Wintoft, “Operational forecasts of the geomagnetic dst index,” *Geophysical Research Letters*, vol. 29, no. 24, pp. 34–1, 2002.

[17] J. E. Borovsky and Y. Y. Shprits, “Is the Dst index sufficient to define all geospace storms?,” *Journal of Geophysical Research: Space Physics*, vol. 122, no. 11, pp. 11–543, 2017.

[18] C. Loewe and G. Prölss, “Classification and mean behavior of magnetic storms,” *Journal of Geophysical Research: Space Physics*, vol. 102, no. A7, pp. 14209–14213, 1997.

[19] A. Smith, M. Freeman, I. Rae, and C. Forsyth, “The influence of sudden commencements on the rate of change of the surface horizontal magnetic field in the united kingdom,” *Space Weather*, vol. 17, no. 11, pp. 1605–1617, 2019.

[20] S. Datta-Barua, A. Mannucci, T. Walter, and P. Enge, “Altitudinal variation of midlatitude localized tec enhancement from ground-and space-based measurements,” *Space Weather*, vol. 6, no. 10, 2008.

[21] A. T. Chartier, S. Datta-Barua, S. McDonald, G. Bust, J. Tate, L. Goncharenko, G. Romeo, and R. Schaefer, “Night-time ionospheric localized enhancements (nile) observed in north america following geomagnetic disturbances,” *Journal of Geophysical Research: Space Physics*, vol. 126, no. 9, p. e2021JA029324, 2021.

[22] L. Qian, A. G. Burns, B. A. Emery, B. Foster, G. Lu, A. Maute, A. D. Richmond, R. G. Roble, S. C. Solomon, and W. Wang, “The ncar tie-gcm: A community model of the coupled thermosphere/ionosphere system,” *Modeling the ionosphere–thermosphere system*, pp. 73–83, 2014.

[23] L. Liu, W. Wan, M.-L. Zhang, B. Ning, S.-R. Zhang, and J. Holt, “Variations of topside ionospheric scale heights over millstone hill during the 30-day incoherent scatter radar experiment,” in *Annales Geophysicae*, vol. 25, pp. 2019–2027, Copernicus Publications Göttingen, Germany, 2007.

[24] G. Chisham, M. Lester, S. Milan, M. Freeman, W. Bristow, A. Grocott, K. McWilliams, J. Ruohoniemi, T. Yeoman, P. L. Dyson, *et al.*, “A decade of the super dual auroral radar network (superdarn): Scientific achievements, new techniques and future directions,” *Surveys in geophysics*, vol. 28, pp. 33–109, 2007.

[25] R. Bannister, “A review of operational methods of variational and ensemble-variational data assimilation,” *Quarterly Journal of the Royal Meteorological Society*, vol. 143, no. 703, pp. 607–633, 2017.

[26] G. Bust, T. Garner, and T. Gaussiran, “Ionospheric data assimilation three-dimensional (ida3d): A global, multisensor, electron density specification algorithm,” *Journal of Geophysical Research: Space Physics*, vol. 109, no. A11, 2004.

[27] G. Bust, G. Crowley, N. Curtis, A. Reynolds, L. Paxton, C. Coker, and P. Bernhardt, “Ida4d-a new ionospheric imaging algorithm using non-linear ground-based and spaced-based data sources,” in *AGU Fall Meeting Abstracts*, vol. 2007, pp. SA11B–06, 2007.

[28] G. Bust and S. Datta-Barua, “Scientific investigations using ida4d and empire,” *modeling the ionosphere–thermosphere system*, pp. 283–297, 2014.

[29] G. Bust and T. Immel, “Ida4d: Ionospheric data assimilation for the icon mission,” *Space Science Reviews*, vol. 216, pp. 1–17, 2020.

[30] J. Anderson, T. Hoar, K. Raeder, H. Liu, N. Collins, R. Torn, and A. Avellano, "The data assimilation research testbed: A community facility," *Bulletin of the American Meteorological Society*, vol. 90, no. 9, pp. 1283–1296, 2009.

[31] A. López Rubio, *Global Estimation and Analysis of Ionospheric Drivers with a Data Assimilation Algorithm.* PhD thesis, Illinois Institute of Technology, 2022.

[32] J. Huba, G. Joyce, and J. Fedder, "Sami2 is another model of the ionosphere (sami2): A new low-latitude ionosphere model," *Journal of Geophysical Research: Space Physics*, vol. 105, no. A10, pp. 23035–23053, 2000.

[33] R. G. Brown and P. Y. Hwang, "Introduction to random signals and applied kalman filtering: with matlab exercises and solutions," *Introduction to random signals and applied Kalman filtering: with MATLAB exercises and solutions*, 1997.

[34] "An intro to plasma." https://superdarn.ca/tutorials-13. Accessed: 2024-04-04.

[35] M. A. MacLeod, "Sporadic E Theory. I. Collision-Geomagnetic Equilibrium.," *Journal of Atmospheric Sciences*, vol. 23, pp. 96–109, Jan. 1966.

[36] S. Datta-Barua, G. Bust, G. Crowley, and N. Curtis, "Neutral wind estimation from 4-d ionospheric electron density images," *Journal of Geophysical Research: Space Physics*, vol. 114, no. A6, 2009.

[37] D. S. Miladinovich, S. Datta-Barua, A. López Rubio, S.-R. Zhang, and G. S. Bust, "Assimilation of gnss measurements for estimation of high-latitude convection processes," *Space Weather*, vol. 18, no. 8, p. e2019SW002409, 2020.

[38] A. López Rubio and S. Datta-Barua, "Vector spherical harmonics for data-assimilative neutral wind estimation," *Space Weather*, vol. 20, no. 8, p. e2022SW003052, 2022. e2022SW003052 2022SW003052.

[39] A. López Rubio and S. Datta-Barua, "Vector spherical harmonics for data-assimilative neutral wind estimation," *Space Weather*, p. e2022SW003052, 2022.

[40] C. C. Finlay, S. Maus, C. Beggan, T. Bondar, A. Chambodut, T. Chernova, A. Chulliat, V. Golovkov, B. Hamilton, M. Hamoudi, *et al.*, "International geomagnetic reference field: the eleventh generation," *Geophysical Journal International*, vol. 183, no. 3, pp. 1216–1230, 2010.

[41] M. Abramowitz and I. A. Stegun, *Handbook of mathematical functions with formulas, graphs, and mathematical tables*, vol. 55. US Government printing office, 1948.

[42] D. S. Miladinovich, S. Datta-Barua, G. S. Bust, and J. J. Makela, "Assimilation of thermospheric measurements for ionosphere-thermosphere state estimation," *Radio Science*, vol. 51, no. 12, pp. 1818–1837, 2016.

[43] "Geomagnetic dst index," *World Data Center for Geomagnetism*, 2015.

[44] E. C. Stone, A. Frandsen, R. Mewaldt, E. Christian, D. Margolies, J. Ormes, and F. Snow, "The advanced composition explorer," *Space Science Reviews*, vol. 86, pp. 1–22, 1998.

[45] P. T. Loto'aniu, K. Romich, W. Rowland, S. Codrescu, D. Biesecker, J. Johnson, H. J. Singer, A. Szabo, and M. Stevens, "Validation of the dscovr spacecraft mission space weather solar wind products," *Space Weather*, vol. 20, no. 10, p. e2022SW003085, 2022.

[46] "Solar wind Merged 1-min and hourly Magnetic Field and Plasma Data from DSCOVR." `https://omniweb.gsfc.nasa.gov/ftpbrowser/dscovr_merged.html`. Accessed: 2024-04-13.

[47] L. Sparks and E. Altshuler, "The spatial distribution of ionospheric threats to waas integrity, 2000–2019: a systematic analysis," in *Proceedings of the 34th International Technical Meeting of the Satellite Division of The Institute of Navigation (ION GNSS+ 2021)*, pp. 3932–3944, 2021.

[48] J. Foster and P. Erickson, "Ionospheric superstorms: Polarization terminator effects in the atlantic sector," *Journal of Atmospheric and Solar-Terrestrial Physics*, vol. 103, pp. 147–156, 2013.

[49] J. Eccles, J. St. Maurice, and R. Schunk, "Mechanisms underlying the prereversal enhancement of the vertical plasma drift in the low-latitude ionosphere," *Journal of Geophysical Research: Space Physics*, vol. 120, no. 6, pp. 4950–4970, 2015.

[50] D. Anderson, "A theoretical study of the ionospheric f region equatorial anomaly—i. theory," *Planetary and Space Science*, vol. 21, no. 3, pp. 409–419, 1973.

[51] N. Balan, J. Souza, and G. Bailey, "Recent developments in the understanding of equatorial ionization anomaly: A review," *Journal of Atmospheric and Solar-Terrestrial Physics*, vol. 171, pp. 3–11, 2018.

[52] H. Lühr, M. Rother, S. Maus, W. Mai, and D. Cooke, "The diamagnetic effect of the equatorial appleton anomaly: Its characteristics and impact on geomagnetic field modeling," *Geophysical Research Letters*, vol. 30, no. 17, 2003.

[53] A. Mannucci, B. Tsurutani, B. Iijima, A. Komjathy, A. Saito, W. Gonzalez, F. Guarnieri, J. Kozyra, and R. Skoug, "Dayside global ionospheric response to the major interplanetary events of october 29–30, 2003 "halloween storms"," *Geophysical Research Letters*, vol. 32, no. 12, 2005.

[54] J. C. Foster, "Ionospheric-magnetospheric-heliospheric coupling: Storm-time thermal plasma redistribution," *Mid-Latitude Dynamics and Disturbances, Geophys. Monogr. Ser*, vol. 181, pp. 121–134, 2008.

[55] T. Matsuo and E. Araujo-Pradere, "Role of thermosphere-ionosphere coupling in a global ionospheric specification," *Radio Science*, vol. 46, 12 2011.

[56] N. Ssessanga, M. Yamamoto, and S. Saito, "Assessing the performance of a northeast asia japan-centered 3-d ionosphere specification technique during the 2015 st. patrick's day geomagnetic storm," *Earth, Planets and Space*, vol. 73, no. 1, 2021.

[57] J. Qiao, Y. Liu, Z. Fan, Q. Tang, X. Li, F. Zhang, Y. Song, F. He, C. Zhou, H. Qing, and Z. Li, "Ionospheric tec data assimilation based on gauss–markov kalman filter," *Advances in Space Research*, vol. 68, no. 10, pp. 4189–4204, 2021.

[58] G. S. Bust, G. Crowley, T. W. Garner, T. L. G. II, R. W. Meggs, C. N. Mitchell, P. S. J. Spencer, P. Yin, and B. Zapfe, "Four-dimensional gps imaging of space weather storms," *Space Weather*, vol. 5, p. S02003, 2007. doi:10.1029/2006SW000237.

[59] L. Scherliess, R. W. Schunk, J. J. Sojka, D. C. Thompson, and L. Zhu, "Utah state university global assimilation of ionospheric measurements gauss-markov kalman filter model of the ionosphere: Model description and validation," *Journal of Geophysical Research: Space Physics*, vol. 111, no. A11, 2006.

[60] M. J. Wu, P. Guo, T. L. Xu, N. F. Fu, X. S. Xu, H. L. Jin, and X. G. Hu, "Data assimilation of plasmasphere and upper ionosphere using cosmic/gps slant tec measurements," *Radio Science*, vol. 50, no. 11, pp. 1131–1140, 2015.

[61] Elvidge, S. and Angling, M. J., "Using the local ensemble transform kalman filter for upper atmospheric modelling," *J. Space Weather Space Clim.*, vol. 9, p. A30, 2019.

[62] L. Mandrake, B. Wilson, C. Wang, G. Hajj, A. Mannucci, and X. Pi, "A performance evaluation of the operational jet propulsion laboratory/university of southern california global assimilation ionospheric model (jpl/usc gaim)," *Journal of Geophysical Research: Space Physics*, vol. 110, no. A12, 2005.

[63] B. Reid, D. R. Themens, A. McCaffrey, P. Jayachandran, M. G. Johnsen, and T. Ulich, "A-chaim: Near-real-time data assimilation of the high latitude ionosphere with a particle filter," *Space weather*, vol. 21, no. 3, p. e2022SW003185, 2023.

[64] A. Pignalberi, J. Habarulema, M. Pezzopane, and R. Rizzi, "On the development of a method for updating an empirical climatological ionospheric model by means of assimilated vtec measurements from a gnss receiver network," *Space Weather*, vol. 17, no. 7, pp. 1131–1164, 2019.

[65] I. Galkin, B. Reinisch, X. Huang, and D. Bilitza, "Assimilation of giro data into a real-time iri," *Radio Science*, vol. 47, no. 4, 2012.

[66] J. He, X. Yue, and Z. Ren, "The impact of assimilating ionosphere and thermosphere observations on neutral temperature improvement: Observing system simulation experiments using enkf," *Space Weather*, vol. 19, no. 10, p. e2021SW002844, 2021. e2021SW002844 2021SW002844.

[67] A. Richmond, "Assimilative mapping of ionospheric electrodynamics," *Advances in Space Research*, vol. 12, no. 6, pp. 59–68, 1992.

[68] AMGeO, *A Collaborative Data Science Platform for the Geospace Community: Assimilative Mapping of Geospace Observations (AMGeO) v1.0.0*, Dec. 2019. Supported by NSF ICER 1928403.

[69] D. Knipp, T. Matsuo, L. Kilcommons, A. Richmond, B. Anderson, H. Korth, R. Redmon, B. Mero, and N. Parrish, "Comparison of magnetic perturbation data from leo satellite constellations: Statistics of dmsp and ampere," *Space Weather*, vol. 12, no. 1, pp. 2–23, 2014.

[70] C.-T. Hsu and N. M. Pedatella, "Assessing the impact of icon/mighti zonal and meridional winds on upper atmosphere weather specification in a whole

atmosphere data assimilation system: An observing system simulation experiment," *Journal of Geophysical Research: Space Physics*, vol. 126, no. 9, p. e2021JA029275, 2021. e2021JA029275 2021JA029275.

[71] F. I. Laskar, N. M. Pedatella, M. V. Codrescu, R. W. Eastes, J. S. Evans, A. G. Burns, and W. McClintock, "Impact of gold retrieved thermospheric temperatures on a whole atmosphere data assimilation model," *Journal of Geophysical Research: Space Physics*, vol. 126, no. 1, p. e2020JA028646, 2021. e2020JA028646 2020JA028646.

[72] L. Scherliess, D. C. Thompson, and R. W. Schunk, "Ionospheric dynamics and drivers obtained from a physics-based data assimilation model," *Radio Science*, vol. 44, no. 1, 2009.

[73] L. Lomidze and L. Scherliess, "Estimation of thermospheric zonal and meridional winds using a kalman filter technique," *Space Weather*, vol. 13, no. 11, pp. 747–760, 2015.

[74] J. X. Yang, Y. You, W. Blackwell, C. Da, E. Kalnay, C. Grassotti, Q. Liu, R. Ferraro, H. Meng, C.-Z. Zou, *et al.*, "Saterr: A community error inventory for satellite microwave observation error representation and uncertainty quantification," *Bulletin of the American Meteorological Society*, 2023.

[75] J. A. Waller, S. L. Dance, and N. K. Nichols, "Theoretical insight into diagnosing observation error correlations using observation-minus-background and observation-minus-analysis statistics," *Quarterly Journal of the Royal Meteorological Society*, vol. 142, no. 694, pp. 418–431, 2016.

[76] J. Durazo, E. J. Kostelich, and A. Mahalov, "Data assimilation for ionospheric space-weather forecasting in the presence of model bias," *Frontiers in Applied Mathematics and Statistics*, vol. 7, 2021.

[77] D. Koshin, K. Sato, K. Miyazaki, and S. Watanabe, "An ensemble kalman filter data assimilation system for the whole neutral atmosphere," 11 2019.

[78] P. M. Mehta and R. Linares, "A new transformative framework for data assimilation and calibration of physical ionosphere-thermosphere models," *Space Weather*, vol. 16, no. 8, pp. 1086–1100, 2018.

[79] H. L. Mitchell and P. L. Houtekamer, "An adaptive ensemble kalman filter," *Monthly Weather Review*, vol. 128, no. 2, pp. 416–433, 2000.

[80] A. Vlasenko, P. Korn, J. Riehme, and U. Naumann, "Estimation of data assimilation error: A shallow-water model study," *Monthly Weather Review*, vol. 142, no. 7, pp. 2502–2520, 2014.

[81] E. Parmuzin, F.-X. L. Dimet, and V. Shutyaev, "On error analysis in variational data assimilation problem for a nonlinear convection–diffusion model," vol. 21, no. 2, pp. 169–183, 2006.

[82] S. Gillijns and B. De Moor, "Model error estimation in ensemble data assimilation," *Nonlinear Processes in Geophysics*, vol. 14, 01 2007.

[83] P. Laloyaux and M. Bonavita, "Improving the handling of model bias in data assimilation," 2020.

[84] A. C. Lorenc, "A global three-dimensional multivariate statistical interpolation scheme," *Monthly Weather Review*, vol. 109, no. 4, pp. 701–721, 1981.

[85] T. Janjić, N. Bormann, M. Bocquet, J. A. Carton, S. E. Cohn, S. L. Dance, S. N. Losa, N. K. Nichols, R. Potthast, J. A. Waller, and P. Weston, "On the representation error in data assimilation," *Quarterly Journal of the Royal Meteorological Society*, vol. 144, no. 713, pp. 1257–1278, 2018.

[86] S. Datta-Barua, G. S. Bust, G. Crowley, and N. Curtis, "Neutral wind estimation from 4-d ionospheric electron density images," *Journal of Geophysical Research*, vol. 114, 2009.

[87] S. Datta-Barua, G. S. Bust, G. Crowley, and N. Curtis, "First storm-time plasma velocity estimates from high-resolution ionospheric data assimilation," *Journal of Geophysical Research: Space Physics*, vol. 118, no. 11, 2013.

[88] S. Datta-Barua, T. Walter, G. S. Bust, and W. Wanner, "Effects of solar cycle 24 activity on waas navigation," *Space Weather*, vol. 12, pp. 46–63, 2014. doi:10.1002/2013SW000982.

[89] D. S. Miladinovich, S. Datta-Barua, G. S. Bust, and J. J. Makela, "Assimilation of thermospheric measurements for ionosphere-thermosphere state estimation,," *Radio Science*, vol. 51, no. 12, pp. 1818–1837, 2016.

[90] D. S. Miladinovich, S. Datta-Barua, A. L. Rubio, S. Zhang, and G. S. Bust, "Assimilation of gnss measurements for estimation of high-latitude convection processes," *Space Weather*, vol. 18, aug 2020.

[91] J. D. Huba, G. Joyce, and J. Krall, "Three-dimensional equatorial spread f modeling," *Geophysical Research Letters*, vol. 35, no. 10, 2008.

[92] OSXDaily, "Pixel version of andromeda galaxy wallpaper from os x lion," 2011. [Online; accessed May 14, 2023].

[93] G. Kirchengast, "The graz ionospheric flux tube simulation model," *Solar-Terrestrial Energy Program: Handbook of Ionospheric Models (edited by R. W. Schunk)*, vol. 23, pp. 96–109, 1996.

[94] Huba, G. Joyce, J. Krall, C. L. Siefring, and P. A. Bernhardt, "Self-consistent modeling of equatorial dawn density depletions with sami3," *Geophysical Research Letters*, vol. 37, no. 3, 2010.

[95] D. Weimer, "Improved ionospheric electrodynamic models and application to calculating joule heating rates," *Journal of Geophysical Research: Space Physics*, vol. 110, no. A5, 2005.

[96] D. P. Drob, J. T. Emmert, J. W. Meriwether, J. J. Makela, E. Doornbos, M. Conde, G. Hernández, J. Noto, K. A. Zawdie, S. E. McDonald, J. D. Huba, and J. H. Klenzing, "An update to the horizontal wind model (hwm): The quiet time thermosphere," *Earth and Space Science*, vol. 2, jul 2015.

[97] J. M. Picone, A. E. Hedin, D. P. Drob, and A. C. Aikin, "Nrlmsise-00 empirical model of the atmosphere: Statistical comparisons and scientific issues," *Journal of Geophysical Research: Space Physics*, vol. 107, pp. SIA 15–1–SIA 15–16, dec 2002. doi: https://doi.org/10.1029/2002JA009430.

[98] J. Palacios, A. Guerrero, C. Cid, E. Saiz, and Y. Cerrato, “Defining scale thresholds for geomagnetic storms through statistics,” *Natural Hazards and Earth System Sciences Discussions*, vol. 2018, pp. 1–17, 2018.

[99] C. C. Finlay, S. Maus, C. D. Beggan, T. N. Bondar, A. Chambodut, T. A. Chernova, A. Chulliat, V. P. Golovkov, B. Hamilton, M. Hamoudi, R. Holme, G. Hulot, W. Kuang, B. Langlais, V. Lesur, F. J. Lowes, H. Luhr, S. Macmillan, M. Mandea, S. McLean, C. Manoj, M. Menvielle, I. Michaelis, N. Olsen, J. Rauberg, M. Rother, T. J. Sabaka, A. Tangborn, L. Toffner-Clausen, E. Thébault, A. W. P. Thomson, I. Wardinski, Z. Wei, and T. I. Zvereva, “International Geomagnetic Reference Field: the eleventh generation,” *Geophysical Journal International*, vol. 183, pp. 1216–1230, 12 2010.

[100] G. Kirchengast, “Elucidation of the physics of the gravity wave-tid relationship with the aid of theoretical simulations,” *Journal of Geophysical Research: Space Physics*, vol. 101, no. A6, pp. 13353–13368, 1996.

[101] D. Hodyss, D. R. Allen, D. Tyndall, P. Caffrey, and S. E. McDonald, “The effects of estimating a photoionization parameter within a physics-based model using data assimilation,” *Journal of Space Weather and Space Climate*, vol. 13, p. 21, 2023.

[102] G. Chisham, M. Freeman, G. Abel, W. Bristow, A. Marchaudon, J. Ruohoniemi, and G. Sofko, “Spatial distribution of average vorticity in the high-latitude ionosphere and its variation with interplanetary magnetic field direction and season,” *Journal of Geophysical Research: Space Physics*, vol. 114, no. A9, 2009.

[103] F. Su, W. Wang, A. G. Burns, X. Yue, and F. Zhu, “The correlation between electron temperature and density in the topside ionosphere during 2006–2009,” *Journal of Geophysical Research: Space Physics*, vol. 120, no. 12, pp. 10–724, 2015.

[104] A. D. Richmond, “Ionospheric electrodynamics using magnetic apex coordinates,” *Journal of geomagnetism and geoelectricity*, vol. 47, no. 2, pp. 191–212, 1995.

[105] K. M. Laundal and A. D. Richmond, “Magnetic coordinate systems,” *Space Science Reviews*, vol. 206, no. 1-4, pp. 27–59, 2017.

[106] D. R. Weimer, “An improved model of ionospheric electric potentials including substorm perturbations and application to the geospace environment modeling november 24, 1996, event,,” *Journal of Geophysical Research*, vol. 106, no. A1, p. 407, 2001.

[107] J. C. Foster, “Storm time plasma transport at middle and high latitudes,” *Journal of Geophysical Research: Space Physics*, vol. 98, no. A2, pp. 1675–1689, 1993.

[108] X. Pi, A. J. Mannucci, and O. Verkhoglyadova, “Polar topside tec enhancement revealed by jason-2 measurements,” *Earth and Space Science*, vol. 8, no. 3, p. e2020EA001429, 2021.

[109] J. Foster, A. Coster, P. Erickson, J. Holt, F. Lind, W. Rideout, M. McCready, A. Van Eyken, R. Barnes, R. Greenwald, *et al.*, “Multiradar observations of the polar tongue of ionization,” *Journal of Geophysical Research: Space Physics*, vol. 110, no. A9, 2005.

[110] J. Foster, W. Rideout, B. Sandel, W. Forrester, and F. Rich, "On the relationship of saps to storm-enhanced density," *Journal of Atmospheric and Solar-Terrestrial Physics*, vol. 69, no. 3, pp. 303–313, 2007.

[111] U. Ramirez, N. Wang, A. T. Chartier, and S. Datta-Barua, "Superdarn evidence for convection-driven lagrangian coherent structures in the polar ionosphere," *Journal of Geophysical Research: Space Physics*, vol. 124, no. 5, pp. 3573–3588, 2019.

[112] J. Ruohoniemi and R. Greenwald, "Dependencies of high-latitude plasma convection: Consideration of interplanetary magnetic field, seasonal, and universal time factors in statistical patterns," *Journal of Geophysical Research: Space Physics*, vol. 110, no. A9, 2005.

[113] A. T. Chartier, T. Matsuo, J. L. Anderson, N. Collins, T. J. Hoar, G. Lu, C. N. Mitchell, A. J. Coster, L. J. Paxton, and G. S. Bust, "Ionospheric data assimilation and forecasting during storms," *Journal of Geophysical Research: Space Physics*, vol. 121, no. 1, pp. 764–778, 2016.

[114] J. Shim, L. Rastätter, M. Kuznetsova, D. Bilitza, M. Codrescu, A. Coster, B. Emery, M. Fedrizzi, M. Förster, T. Fuller-Rowell, *et al.*, "Cedar-gem challenge for systematic assessment of ionosphere/thermosphere models in predicting tec during the 2006 december storm event," *Space Weather*, vol. 15, no. 10, pp. 1238–1256, 2017.

[115] M. W. Liemohn, A. D. Shane, A. R. Azari, A. K. Petersen, B. M. Swiger, and A. Mukhopadhyay, "Rmse is not enough: Guidelines to robust data-model comparisons for magnetospheric physics," *Journal of Atmospheric and Solar-Terrestrial Physics*, vol. 218, p. 105624, 2021.

[116] G. Evensen, F. C. Vossepoel, and P. J. Van Leeuwen, *Data assimilation fundamentals: A unified formulation of the state and parameter estimation problem.* Springer Nature, 2022.

[117] G. Bust, G. Crowley, N. Curtis, A. Reynolds, L. Paxton, C. Coker, and P. Bernhardt, "IDA4D - a new ionospheric imaging algorithm using non-linear ground-based and spaced- based data sources," in *AGU Fall Meeting Abstracts*, vol. 2007, pp. SA11B–06, Dec. 2007.

[118] G. Hajj, B. Wilson, C. Wang, X. Pi, and I. Rosen, "Data assimilation of ground gps total electron content into a physics-based ionospheric model by use of the kalman filter," *Radio Science*, vol. 39, no. 1, pp. 1–17, 2004.

[119] C. Wang, G. Hajj, X. Pi, I. G. Rosen, and B. Wilson, "Development of the global assimilative ionospheric model," *Radio Science*, vol. 39, no. 1, pp. 1–11, 2004.

[120] A. Komjathy, B. Wilson, X. Pi, V. Akopian, M. Dumett, B. Iijima, O. Verkhoglyadova, and A. J. Mannucci, "Jpl/usc gaim: On the impact of using cosmic and ground-based gps measurements to estimate ionospheric parameters," *Journal of geophysical research: space physics*, vol. 115, no. A2, 2010.

[121] G. Bailey, N. Balan, and Y. Su, "The sheffield university plasmasphere ionosphere model—a review," *Journal of Atmospheric and Solar-Terrestrial Physics*, vol. 59, no. 13, pp. 1541–1552, 1997.

[122] X. Pi, C. Wang, G. A. Hajj, G. Rosen, B. D. Wilson, and G. J. Bailey, "Estimation of e$\times$ b drift using a global assimilative ionospheric model: An observation system simulation experiment," *Journal of Geophysical Research: Space Physics*, vol. 108, no. A2, 2003.

[123] X. Pi, A. J. Mannucci, B. A. Iijima, B. D. Wilson, A. Komjathy, T. F. Runge, and V. Akopian, "Assimilative modeling of ionospheric disturbances with formosat-3/cosmic and ground-based gps measurements," *TAO: Terrestrial, Atmospheric and Oceanic Sciences*, vol. 20, no. 1, p. 2, 2009.

[124] L. Scherliess, R. W. Schunk, J. J. Sojka, and D. C. Thompson, "Development of a physics-based reduced state kalman filter for the ionosphere," *Radio Science*, vol. 39, no. 1, pp. 1–12, 2004.

[125] L. Scherliess, R. W. Schunk, J. J. Sojka, D. C. Thompson, and L. Zhu, "Utah state university global assimilation of ionospheric measurements gauss-markov kalman filter model of the ionosphere: Model description and validation," *Journal of Geophysical Research: Space Physics*, vol. 111, no. A11, 2006.

[126] L. Scherliess, D. C. Thompson, and R. W. Schunk, "Ionospheric dynamics and drivers obtained from a physics-based data assimilation model," *Radio Science*, vol. 44, p. RS0A32, Feb. 2009.

[127] R. W. Schunk, L. Scherliess, V. Eccles, L. Gardner, J. J. Sojka, L. Zhu, X. Pi, A. Mannucci, B. Wilson, A. Komjathy, *et al.*, "Ensemble modeling with data assimilation models: A new strategy for space weather specifications, forecasts, and science," *Space Weather*, vol. 12, no. 3, p. 123, 2014.

[128] R. W. Schunk, L. Scherliess, V. Eccles, L. C. Gardner, J. J. Sojka, L. Zhu, X. Pi, A. J. Mannucci, A. Komjathy, C. Wang, *et al.*, "Challenges in specifying and predicting space weather," *Space weather*, vol. 19, no. 2, p. e2019SW002404, 2021.

[129] G. Lu, "Large scale high-latitude ionospheric electrodynamic fields and currents," *Space Science Reviews*, vol. 206, no. 1-4, pp. 431–450, 2017.

[130] G. Lu, A. Richmond, J. Ruohoniemi, R. Greenwald, M. Hairston, F. Rich, and D. Evans, "An investigation of the influence of data and model inputs on assimilative mapping of ionospheric electrodynamics," *Journal of Geophysical Research: Space Physics*, vol. 106, no. A1, pp. 417–433, 2001.

[131] D. P. Munoz and P. J. Istvan, "Lateral inhibitory interactions in the intermediate layers of the monkey superior colliculus," *J. Neurophysiol.*, vol. 79, no. 3, pp. 1193–1209, 1998.

[132] T. Matsuo, L. M. Kilcommons, W. Mirkovich, J. M. Ruohoniemi, S. Chakraborty, B. J. Anderson, and S. K. Vines, "Assimilative mapping of geospace observations (amgeo): Unified global and local perspectives on high-latitude ionospheric electrodynamics," in *AGU Fall Meeting Abstracts*, vol. 2020, pp. SA026–03, 2020.

[133] S.-R. Zhang, P. J. Erickson, J. C. Foster, J. M. Holt, A. J. Coster, J. J. Makela, J. Noto, J. W. Meriwether, B. J. Harding, J. Riccobono, *et al.*, "Thermospheric poleward wind surge at midlatitudes during great storm intervals," *Geophysical Research Letters*, vol. 42, no. 13, pp. 5132–5140, 2015.

[134] G. Kirchengast, "The graz ionospheric flux tube simulation model," *STEP Handbook of Ionospheric Models*, pp. 73–94, 1996.

[135] J. Picone, A. Hedin, D. P. Drob, and A. Aikin, "Nrlmsise-00 empirical model of the atmosphere: Statistical comparisons and scientific issues," *Journal of Geophysical Research: Space Physics*, vol. 107, no. A12, pp. SIA–15, 2002.

[136] D. Weimer, "Predicting surface geomagnetic variations using ionospheric electrodynamic models," *Journal of Geophysical Research: Space Physics*, vol. 110, no. A12, 2005.

[137] D. P. Drob, J. T. Emmert, J. W. Meriwether, J. J. Makela, E. Doornbos, M. Conde, G. Hernandez, J. Noto, K. A. Zawdie, S. E. McDonald, *et al.*, "An update to the horizontal wind model (hwm): The quiet time thermosphere," *Earth and Space Science*, vol. 2, no. 7, pp. 301–319, 2015.

[138] T. Janjić, N. Bormann, M. Bocquet, J. Carton, S. Cohn, S. L. Dance, S. Losa, N. K. Nichols, R. Potthast, J. A. Waller, *et al.*, "On the representation error in data assimilation," *Quarterly Journal of the Royal Meteorological Society*, vol. 144, no. 713, pp. 1257–1278, 2018.

[139] S. Yadav, R. Choudhary, J. Kumari, S. Sunda, P. Shreedevi, and T. K. Pant, "Reverse fountain and the nighttime enhancement in the ionospheric electron density over the equatorial region: A case study," *Journal of Geophysical Research: Space Physics*, vol. 125, no. 5, p. e2019JA027286, 2020.

[140] W. Li, Y. Chen, L. Liu, H. Le, R. Zhang, J. Li, and C. Huang, "A statistical study on the winter ionospheric nighttime enhancement at middle latitudes in the northern hemisphere," *Journal of Geophysical Research: Space Physics*, vol. 125, no. 7, p. e2020JA027950, 2020.

[141] L. Zhao, Q.-H. Zhang, Y. WANG, and Z.-Y. Xing, "Characteristics of ionospheric nighttime enhancement at mid-high latitude region in the northern hemisphere," in *AGU Fall Meeting Abstracts*, vol. 2021, pp. SA45D–2247, 2021.

[142] X. Luan, W. Wang, A. Burns, S. C. Solomon, and J. Lei, "Midlatitude nighttime enhancement in f region electron density from global cosmic measurements under solar minimum winter condition," *Journal of Geophysical Research: Space Physics*, vol. 113, no. A9, 2008.

[143] E. M. El-Desoky, M. M. Hoque, M. Youssef, and A. Mahrous, "Seasonal morphology and solar activity dependence analysis of mid-latitude post-midnight enhancement using global ionospheric map," *Advances in Space Research*, vol. 73, no. 7, pp. 3624–3641, 2024.

[144] P. Rajesh, J. Liu, N. Balan, C. Lin, Y. Sun, and S. Pulinets, "Morphology of midlatitude electron density enhancement using total electron content measurements," *Journal of Geophysical Research: Space Physics*, vol. 121, no. 2, pp. 1503–1517, 2016.

[145] L. Sparks, A. Komjathy, and A. Mannucci, "Extreme ionospheric storms and their impact on WAAS," 2005.

[146] Y. Yang, L. Liu, X. Zhao, H. Xie, Y. Chen, H. Le, R. Zhang, M. A. Tariq, and W. Li, "Ionospheric nighttime enhancements at low latitudes challenge performance of the global ionospheric maps," *Remote Sensing*, vol. 14, no. 5, p. 1088, 2022.

[147] A. Coster, "Data from the CEDAR madrigal database.," 2003. `https://w3id.org/cedar?experiment_list=experiments3/2003/gps20nov03&file_list=gps031120g.004.hdf5`.

[148] W. Rideout and A. Coster, "Automated gps processing for global total electron content data," *GPS solutions*, vol. 10, pp. 219–228, 2006.

[149] S. Datta-Barua, T. W. A. J. Mannucci, and P. Enge, "Altitudinal variation of midlatitude localized tec enhancement from ground- and space-based measurements," *Space Weather*, vol. S10D06, 2008. doi:10.1029/2008SW000396.

[150] H.-L. Liu, C. G. Bardeen, B. T. Foster, P. Lauritzen, J. Liu, G. Lu, D. R. Marsh, A. Maute, J. M. McInerney, N. M. Pedatella, *et al.*, "Development and validation of the whole atmosphere community climate model with thermosphere and ionosphere extension (waccm-x 2.0)," *Journal of Advances in Modeling Earth Systems*, vol. 10, no. 2, pp. 381–402, 2018.

[151] A. Maute, "Thermosphere-ionosphere-electrodynamics general circulation model for the ionospheric connection explorer: Tiegcm-icon," *Space Science Reviews*, vol. 212, no. 1-2, pp. 523–551, 2017.

[152] A. Richmond and A. Maute, "Ionospheric electrodynamics modeling," *Modeling the ionosphere–thermosphere system*, pp. 57–71, 2014.

[153] R. A. Heelis, J. K. Lowell, and R. W. Spiro, "A model of the high-latitude ionospheric convection pattern," *Journal of Geophysical Research*, vol. 87, nov 1982.

[154] M. Asch, M. Bocquet, and M. Nodet, *Data assimilation: methods, algorithms, and applications*. SIAM, 2016.

[155] R. E. Kalman, "A new approach to linear filtering and prediction problems," 1960.

[156] B. Dong, R. Bannister, Y. Chen, A. Fowler, and K. Haines, "Simplified kalman smoother and ensemble kalman smoother for improving reanalyses," *Geoscientific Model Development*, vol. 16, no. 14, pp. 4233–4247, 2023.

[157] Y. Zhu, R. Todling, J. Guo, S. E. Cohn, I. M. Navon, and Y. Yang, "The geos-3 retrospective data assimilation system: The 6-hour lag case," *Monthly weather review*, vol. 131, no. 9, pp. 2129–2150, 2003.

[158] E. Cosme, J.-M. Brankart, J. Verron, P. Brasseur, and M. Krysta, "Implementation of a reduced rank square-root smoother for high resolution ocean data assimilation," *Ocean Modelling*, vol. 33, no. 1-2, pp. 87–100, 2010.

[159] E. Pinnington, T. Quaife, A. Lawless, K. Williams, T. Arkebauer, and D. Scoby, "The land variational ensemble data assimilation framework: Lavendar v1. 0.0," *Geoscientific Model Development*, vol. 13, no. 1, pp. 55–69, 2020.

[160] F. Rabier, P. Courtier, and M. Ehrendorfer, "Four-dimensional data assimilation: Comparison of variational and sequential algorithms," *Quarterly Journal of the Royal Meteorological Society*, vol. 118, no. 506, pp. 673–713, 1992.

[161] F. Rabier and Z. Liu, "Variational data assimilation: theory and overview," in *Proc. ECMWF Seminar on Recent Developments in Data Assimilation for Atmosphere and Ocean, Reading, UK, September 8–12*, pp. 29–43, 2003.

[162] R. Ménard and R. Daley, "The application of kalman smoother theory to the estimation of 4dvar error statistics," *Tellus A*, vol. 48, no. 2, pp. 221–237, 1996.

[163] L. Bruhwiler, A. Michalak, W. Peters, D. Baker, and P. Tans, "An improved kalman smoother for atmospheric inversions," *Atmospheric Chemistry and Physics*, vol. 5, no. 10, pp. 2691–2702, 2005.

[164] Z. Li and I. Navon, "Optimality of variational data assimilation and its relationship with the kalman filter and smoother," *Quarterly Journal of the Royal Meteorological Society*, vol. 127, no. 572, pp. 661–683, 2001.

[165] M. Fisher, M. Leutbecher, and G. Kelly, "On the equivalence between kalman smoothing and weak-constraint four-dimensional variational data assimilation," *Quarterly Journal of the Royal Meteorological Society: A journal of the atmospheric sciences, applied meteorology and physical oceanography*, vol. 131, no. 613, pp. 3235–3246, 2005.

[166] T. Milewski and M. Bourqui, "Potential of an ensemble kalman smoother for stratospheric chemical-dynamical data assimilation," *Tellus A: Dynamic Meteorology and Oceanography*, vol. 65, no. 1, p. 18541, 2013.

[167] E. Klimova, "Application of the ensemble kalman filter to environmental data assimilation," in *Iop conference series: Earth and environmental science*, vol. 211, p. 012049, IOP Publishing, 2018.

[168] J. Tang and Q. Zhuang, "Propagating correlations in atmospheric inversions using different kalman update smoothers," *Atmospheric Chemistry & Physics Discussions*, vol. 10, no. 8, pp. 19219–19245, 2010.

[169] S. E. Cohn, N. Sivakumaran, and R. Todling, "A fixed-lag kalman smoother for retrospective data assimilation," *Monthly Weather Review*, vol. 122, no. 12, pp. 2838–2867, 1994.

[170] C. L. Waters, B. Anderson, D. Green, H. Korth, R. Barnes, and H. Vanhamäki, "Science data products for ampere," *Ionospheric multi-spacecraft analysis tools: Approaches for deriving ionospheric parameters*, pp. 141–165, 2020.

[171] G. Haines, "Spherical cap harmonic analysis," *Journal of Geophysical Research: Solid Earth*, vol. 90, no. B3, pp. 2583–2591, 1985.

[172] P. J. Olver, *Applications of Lie groups to differential equations*, vol. 107. Springer Science & Business Media, 1993.

[173] M. Abramowitz and I. Stegun, "Handbook of mathematical functions," *New York: Dover Publications*, 1965. Accessed http://people.math.sfu.ca/cbm/aands/.